Crevice Volume Effect on Spark Ignition Engine Efficiency

by

Patrick M. Smith

B.S., Mechanical Engineering
Georgia Institute of Technology (2011)

Submitted to the Department of Mechanical Engineering
in Partial Fulfillment of the Requirements for the Degree of

Master of Science in Mechanical Engineering

at the

MASSACHUSETTS INSTITUTE OF TECHNOLOGY

September 2013

Signature of Author.....
Department of Mechanical Engineering
July 8th, 2013

Certified by.....
Wai K. Cheng
Professor of Mechanical Engineering
Thesis Supervisor

Certified by.....
John B. Heywood
Sun Jae Professor of Mechanical Engineering
Thesis Supervisor

Accepted by .....
David Hardt
Professor of Mechanical Engineering
Chairman, Department Committee on Graduate Theses

This page intentionally left blank

Crevice Volume Effect on Spark Ignition Engine Efficiency

by

Patrick M. Smith

Submitted to the Department of Mechanical Engineering
on August 7th, 2013 in Partial Fulfillment of the
Requirements for the Degree of Master of Science in
Mechanical Engineering

Abstract

A set of experiments and a simulation study are completed to quantify the effect of the piston crevice on engine efficiency. The simulation study breaks down the loss mechanisms on brake efficiency at different displacement volumes (300 – 500 cc) and compression ratios (8-20). Experiments focus on indicated efficiencies for a narrow range of compression ratios (9.24-12.57) with different piston crevice volumes. Piston crevice volume is increased in two steps by machining a groove into the piston top land, and is decreased by raising the top ring. Indicated efficiency is measured at various loads (0.4 – 1.0 bar MAP), speeds (1500, 2000, 2500 rpm), and coolant temperatures (50°C and 80°C). All data points compared in this study are recorded at MBT timing with a relative air-fuel ratio (λ) of 1.

For the baseline case (CR = 9.24, speed = 2000 rpm, coolant = 80°C), increased crevice volume results in an indicated efficiency degradation of 0.3-0.5%-points per 1000 mm^3. This absolute decrease corresponds to a 1.2-1.5% relative decrease for a 100% increase in crevice volume; referenced to the control piston crevice modification. Decreasing crevice volume leads to a gain in indicated efficiency of 2.3-3.5%-points per 1000 mm^3, which corresponds to a 6.9-11.8% relative increase for a 100% decrease in crevice volume; referenced to the control piston crevice modification.

Results of the experimental investigation, when compared across compression ratio, engine speed, and coolant temperature, show that the crevice effect on efficiency is largely independent of these three parameters. Large gains from decreased piston crevice volume prompt renewed discussions on piston top land, top ring, and crown design.

Thesis Supervisor: Wai K. Cheng
Title: Professor of Mechanical Engineering

Thesis Supervisor: John B. Heywood
Title: Professor of Mechanical Engineering

This page intentionally left blank

Acknowledgments

I have to start with the two most important people to my research and experience here at MIT, my advisors, Professors Wai Cheng and John Heywood. They constantly challenged me to dive deeper into results, while providing necessary guidance, so that I learned more than I could have previously imagined about automotive engines. They made possible numerous opportunities, significantly broadening my analytical, interpersonal, and teaching abilities. I've notched down so many firsts: became a teaching assistant, presented a paper at a major conference, and discuss experimental results with industry leaders. One of the highlights of my two years at MIT was attending the SAE World Congress with Professor Cheng; delivering a presentation, learning about modern research topics, and general chilling with Professor Cheng. This time at MIT has taught me plenty about engineering, but significantly more about what I am personally capable of, and I owe a huge portion of this to Professors Cheng and Heywood.

The Sloan Automotive Lab has been a great place to work. I would like to thank all of the MIT employees who make sure the lab runs smoothly. Specifically, I would like to thank Janet Maslow and Karla Stryker for helping me set up meetings, putting together consortium presentations, and being patient helping me with the many little things I wasn't familiar with. On the technical side I would like to thank Raymond Phan for helping me build and fix things on my engine, and Thane DeWitt for coordinating purchases and repairs.

Without my fellow students in the Sloan Automotive Lab there were many days when I would have just been hopelessly lost. I want to thank Kevin Cedrone, Justin Ketterer, Jacob McKenzie, and Tomas Vianna Martins for all of their help around the lab. Each of you has helped me immensely in fixing engine problems, perfecting data analysis techniques, and providing valuable insight into experimental techniques.

I would also like to thank Dr. Tian Tian for helping out on blowby simulations. Even with very little notice and many other things going on you helped me get some valuable results. I really appreciate that.

My research is made possible by members of the MIT Engine and Fuels Consortium: Borg Warner, Chrysler, Ford, and General Motors. I would especially like to thank Tom Leone and Rick Davis, who both took an active interest in my project and whose cooperation contributed to many aspects of this project and thesis. These consortium meetings were incredibly valuable in advancing my research and always provided great feedback. The regular meetings provided necessary structure to this study and kept me on my toes trying to obtain and explain data. They also provided a great excuse to celebrate over a couple of drinks.

I would like to thank all of my friends for making certain I had fun outside of research. Y'all made sure my two years at MIT were anything but dull and for that I am incredibly grateful.

Finally, I would like to thank my family for always being supportive, pushing me to succeed, and giving me great advice along the way. I may not even have applied to MIT without your encouragement and definitely wouldn't have gotten in without your guidance. You guys have always been there for me and I love you all so much. I couldn't have asked for a better family.

This page intentionally left blank

Table of Contents

List of Figures

This page intentionally left blank

List of Tables

This page intentionally left blank

Nomenclature

Acronyms

ABDC	After Bottom Dead Center
ATDC	After Top Dead Center
BBDC	Before Bottom Dead Center
BDC	Bottom Dead Center
BMEP	Brake Mean Effective Pressure
BTDC	Before Top Dead Center
CA90	Crank angle at 90% mass fraction burned
CAD	Crank Angle Degree
CAFÉ	Corporate Average Fuel Economy
COV	Coefficient of Variation
CR	Compression Ratio
DAQ	Data Acquisition
ECU	Engine Control Unit
EI	Emission Index
EVC	Exhaust Valve Closing
EVO	Exhaust Valve Opening
FFID	Fast Flame Ionization Detector
GIMEP	Gross indicated Mean Effective Pressure
IMEP	Indicated Mean Effective Pressure
IVC	Intake Valve Closing
IVO	Intake Valve Opening
LA4	Urban Dynamometer Driving Schedule
MAP	Manifold Air Pressure
MBT	Maximum Brake Torque
MCU	Main Control Unit
MFB	Mass Fraction Burned
NEDC	New European Driving Cycle
NIMEP	Net Indicated Mean Effective Pressure
NVH	Noise-Vibration-Harshness
PFI	Port Fuel Injection
RPM	Revolutions Per Minute
TDC	Top Dead Center
UEGO	Universal Exhaust Gas Oxygen

Symbols

$\bar{S}_p$	Mean piston speed
h_c	Convective heat transfer coefficient
E_{crev}	Fuel energy of the trapped fuel in the crevice volume at peak pressure
Pe_2	Peclet number
Q_{LHV}	Lower heating value
R_{swirl}	Swirl Ratio
R_{tumble}	Tumble ratio
S_L	Laminar flame speed
T_{crev}	Crevice gas temperature
U_{swirl}	Swirl velocity
U_{tumble}	Tumble velocity
V_{crev}	Crevice volume
V_d	Displacement volume
W_f	Friction Work
$W_{g,s}$	Indicated gross work output
W_p	Pumping Work
c_p	Specific heat at constant pressure
$d_{q,2}$	Two-plate quench distance
m_{crev}	Mass trapped in the crevice
$m_{f,crev}$	Mass of fuel in the crevice
m_f	Fuel mass
m_r	Residual mass
p_{peak}	Peak pressure
r_c	Compression ratio
$x_{r,IVO}$	Residual mass fraction due to trapped mass at IVO
$x_{r,backflow}$	Residual mass due to exhaust backflow
x_r	Residual mass fraction
$\eta_{f,ig}$	Indicated gross fuel conversion efficiency
$\eta'_{i,g}$	Gross indicated efficiency of burning crevice gas
p	Pressure
T	Temperature
A	Area
N	Engine speed in rev/s
R	Gas constant
k	Thermal conductivity
m	Total charge mass
x	Mass fraction burned
α	Coefficient of thermal expansion
γ	Ratio of specific heats
θ	Crank angle
ρ	Density
φ	Fuel/air equivalence ratio

1 Introduction

Since the introduction of the CAFE standards in 1975 the US has been moving toward a more fuel efficient passenger vehicle fleet. Recently, CO_2 emissions have become a key issue in global energy use, with automotive applications as an important focus. In 2012 an aggressive new standard [1] was introduced requiring vast improvements in vehicle fuel economy extending to 2025. To satisfy these strict requirements more efficient engine technology is required. It has been shown that there are large gains to be had by improving current gasoline engine technology [2–4]. One very promising solution successfully being realized by automotive manufacturers is shifting towards turbocharged downsized engines [5–11].

1.1 Turbocharged Downsized Engines

Current production engines tend to be naturally aspirated engines matched to vehicles based on maximum expected loads. To improve fuel economy these naturally aspirated engines are being replaced by smaller turbocharged engines. Figure 1-1 shows a typical drive cycle across the performance map of a naturally aspirated engine. It can be seen that a significant portion of the drive cycle is spent at part load. Downsized engines have reduced displacement volumes, thus requiring the engine to work at a higher mean effective pressure under part load conditions to meet the same torque. This lowers pumping, friction, and heat transfer losses. The turbocharger then acts to match, and in many cases exceed, the maximum torque of the replaced naturally aspirated engine. Significant fuel consumption gains (upwards of 15% over the NEDC cycle) have been reported [8].

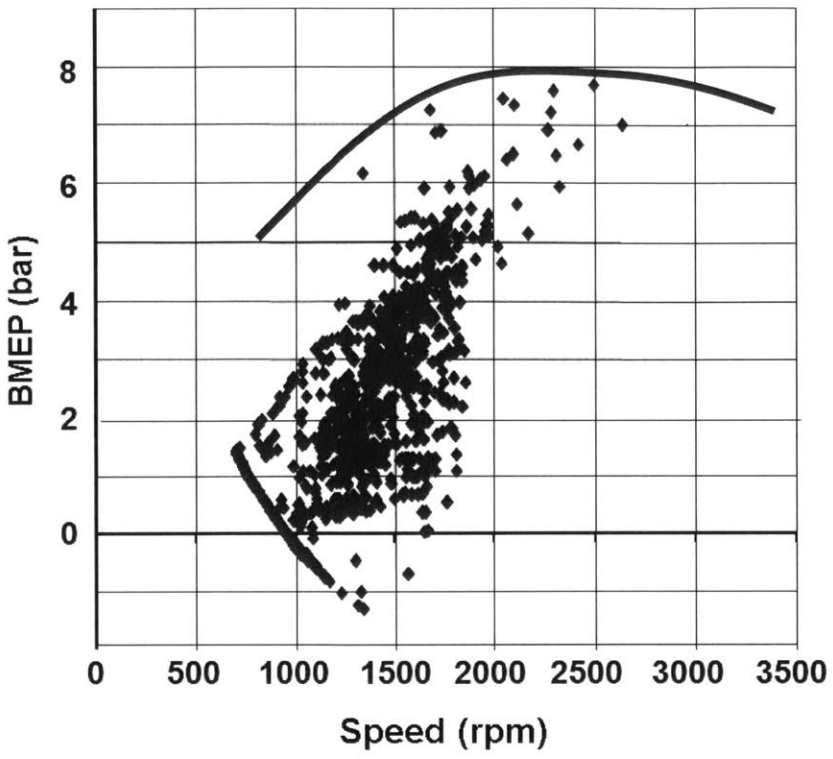

Figure 1-1 LA4 drive cycle results for a small passenger vehicle showing majority of city driving takes place at part load.

To decrease engine displacement there are two options: decrease the number of cylinders and/or decrease individual cylinder size. Due to noise-vibration-harshness (NVH) concerns the number of cylinders is limited to at least 2. Therefore, at some point, individual cylinder size must be reduced. As cylinder size is reduced engine crevice volumes become a major source of inefficiency due to a number of factors, but mainly from disproportionate scaling of the gap between piston and cylinder. Therefore the crevice effect on engine efficiency has become an important loss mechanism to quantify as engine displacement continues to decrease.

1.2 Total Engine Crevices

Engine crevices consist of small spaces within the combustion chamber, filled with unburned mixture, whose characteristic dimension does not allow a flame to penetrate. The various crevices present in modern engines are displayed in Figure 1-2. The head gasket crevice is composed of the gaps between the head gasket and cylinder liner and the head gasket and head.

The spark plug crevice consists of the space between the spark plug threads and engine head ignoring the space between the spark plug central electrode and spark plug body that is large enough for a flame to enter. The valve seat crevice is the space between the valves and their seats in the engine head. The piston ring-pack crevice consists of the top land volume, the side and back top ring volume, and the volume between the first and second rings. Within the piston ring-pack crevice the top land volume and side and back top ring volumes will be collectively known as the piston crevice. This piston crevice is by far the largest crevice and has been shown to account for 80% of the crevice hydrocarbon emissions [12]. In addition, the remaining crevices (valve seat, spark plug thread, and cylinder-head gasket) all scale with engine size, so as engines downsize the piston crevice will only further dominate the total crevice volume. The piston crevice has thusly been chosen as the focus of this project.

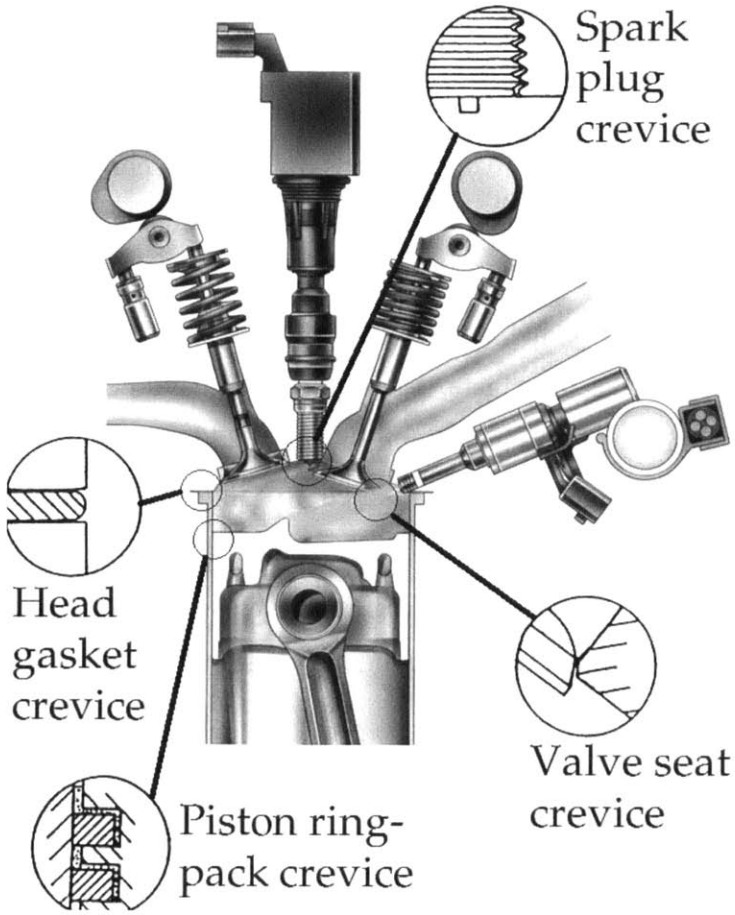

Figure 1-2 Various engine crevices present in a modern spark ignition engine.

1.3 Crevice Mechanism

A crevice becomes a source of inefficiency and hydrocarbon emissions when the unburned mixture trapped within escapes primary combustion. This occurs when the entrance to said crevice is geometrically such that a flame cannot enter. This phenomenon is known as flame quenching and occurs when a flame loses energy (through heat transfer to the walls, burned mixture, and unburned mixture) faster than it can be created from the chemical reaction within the flame. The balance between energy loss and generation is dictated by fuel properties, in-cylinder conditions (pressure, temperature, and composition), and crevice geometry. At the very narrow crevice entrances wall surface area becomes large compared to flame front area and quenching occurs.

1.3.1 Laminar Flame Quenching

Over the past half century laminar flame quenching has been a major topic in the combustion field, with many studies focusing on applications to internal combustion engines. Multiple approaches have been pursued using parallel plates, tubes, channels and other simple geometry to measure this quenching effect. Of particular relevance to engine crevice quenching are the parallel-plate quenching experiments, which find the minimum distance between two large parallel plates that a flame can propagate. Various studies have been completed, successfully relating two plate quench distances to quenching in engine [13–16]. In these studies crevice gaps were varied and tested in engines and compared to laminar flame quenching dimensions. Multiple analysis techniques were used to detect flame quenching using ionization probes [13,14], optical measurements [15], and hydrocarbon emissions data [16]. These studies show the applicability of using simple two plate quench distance calculations for crevice flame quenching in engines.

There are a number of correlations available for finding two plate quench distances given engine conditions [17–19]. Portions of the methods used by Lavoie and Williams are combined in this study to calculate quench distances. Lavoie suggests a correlation for Peclet numbers shown in Equation 1.1 based on experiments using propane:

$$Pe_2 = \frac{9.5}{\varphi}\left(\frac{p}{3}\right)^{.26*\min(1,1/\varphi^2)} \quad [1.1]$$

where Pe_2 is the Peclet number, φ is the fuel/air equivalence ratio, and p is the in-cylinder pressure, in atmosphere. Then, similar to Williams' correlation but with Peclet numbers replacing the experimental constant, the quench distance is calculated based on heat conduction losses using Equation 1.2:

$$d_{q,2} = \frac{Pe_2 k_f}{\rho_u S_L c_{p,f}} \quad [1.2]$$

where $d_{q,2}$ is the two-plate quench distance, k_f is the thermal conductivity at flame conditions, ρ_u is the unburned gas density, S_L is the laminar flame speed, and $c_{p,f}$ is the specific heat at constant pressure at flame conditions. Laminar flame speeds are calculated using correlations found for gasoline [20,21]. Unburned and flame properties are calculated using results from NASA equilibrium programs [22] found in Professor Heywood's textbook [23]. Under normal operating conditions quench distances can range from 0.2 to 0.8 mm, and further details regarding quench distance calculations are available in Appendix A:.

Focusing on the piston crevice, the characteristic quench dimension is the radial clearance between the piston and cylinder. In a rather simplified view, if the radial clearance of the piston is smaller than the laminar flame quench distance upon flame arrival then the flame cannot penetrate into the crevice. Based on this view of flame quenching it is important to accurately measure room temperature piston-cylinder clearance and understand piston and cylinder temperatures so as to estimate thermal expansion.

1.3.2 Piston Thermal Expansion

Piston and cylinder thermal expansion dictate piston-cylinder clearance design in modern engines. The clearance must be large enough to handle thermal expansion at the highest expected component temperatures experienced at full load. These maximum temperatures are similar between engines of dissimilar size. A smaller piston will expand slightly less at a given

temperature, allowing for a slightly tighter clearance, but this benefit does not scale as quickly as clearance volume in engine downsizing. This leads to the piston crevice volume making up a larger percent of the clearance volume in downsized engines. Additionally, because the clearance is designed for maximum load it will be larger under the part load conditions of interest to this study.

Engine component temperatures have been studied while looking at heat transfer characteristics of engines [24–26]. From these component temperatures a simple application of unrestrained thermal expansion can be applied using Equation 1.3:

$$diameter = diameter * [1 + \alpha * (T_{hot} - T_{room\ temp})] \quad [1.3]$$

where α is the coefficient of thermal expansion and T is temperature. For the piston an unconstrained expansion approximation reflects the physics of the actual expansion and for the cylinder lower temperatures and a low coefficient of thermal expansion limit expansion, thus allowing the approximation to remain close.

1.4 Crevice Effect on Efficiency

Unburned fuel-air mixture is pushed into the piston crevice as the charge is pressurized by the piston compression stroke and the expansion of the burned gas. When quenching at the crevice entrance occurs, this unburned fuel-air mixture escapes oxidation in the main combustion process. After the main combustion process completes, the unburned crevice mixture discharges into the cylinder due to the lowering charge pressure and piston downward movement. As the crevice gas mixes with hot burned gases in the cylinder, it is oxidized in a secondary oxidation process, which contributes to engine work output at a discounted rate due to a less favorable heat release schedule.

1.4.1 Crevice Outflow

To fully grasp the crevice effect on efficiency it is vital to understand the outflow and secondary oxidation of trapped unburned crevice gas. In a Schlieren visualization study

conducted at the Sloan Automotive Laboratory Namazian [27] showed that during the expansion stroke the crevice gas slowly expands upward and is left in a thin layer above the crevice as the piston moves downward. Expanding on a crevice outflow model developed by Namazian, Min looked at crevice outflow velocities and characteristics [28,29]. Using normalized velocities it was shown that the escaping gas from the piston crevice flows upward with respect to the piston but downward with respect to the liner. This flow out of the piston crevice was found to be laminar with normalized velocity independent of speed and load. Combined these conclusions show that as the piston moves downward it lays down a thin layer of crevice gas along the cylinder wall in a laminar fashion, with a majority of the crevice mass deposited early in the expansion stroke. In Figure 1-3, a visualization taken from Min [28] shows the laydown process.

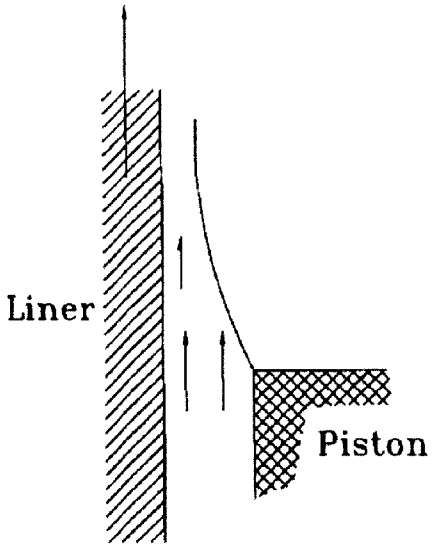

Figure 1-3 Crevice outflow geometry in the reference frame of piston. The outflow is stretched into a thin layer in a laminar fashion by the upward moving liner in the expansion stroke [28].

1.4.2 Crevice Oxidation

Once the crevice gas is deposited on the walls of the cylinder it then has the opportunity to undergo secondary oxidation. A useful approximation in this oxidation process is to treat the crevice gas as vertically stationary along the wall diffusing outward into the bulk burned gas. Min [29] and Wu [30] used this one dimensional approach to simulate crevice gas oxidation. Both of these studies showed that the dominant factor in this oxidation process is bulk gas

temperature and that most hydrocarbons trapped in the crevice are consumed before exiting the cylinder. Min gave a detailed view of crevice oxidation, looking at the time history of crevice gas particles laid along the cylinder. In this view it was shown that crevice gas leaving the piston crevice early in the exhaust stroke is almost fully oxidized. This, combined with the fact that most crevice gas exits early in the expansion stroke, showed that most hydrocarbons trapped in the piston crevice are oxidized before leaving the cylinder. Additionally this study showed an interesting look at heat release piggybacking that caused engine configurations with high crevice volumes to continue crevice gas oxidation further into the expansion stroke. Wu showed the cutoff temperature for nearly complete oxidation to be about 1400 K and found that between 50 and 90 percent of the trapped hydrocarbons are consumed in post flame oxidation. Another study using laser-induced fluorescence to look at both unburned mixture and oxidation reactions confirmed these simulations by showing that nearly all crevice gas exiting the piston crevice is oxidized until bulk gas temperature is dramatically cooled by exhaust valve opening [31].

Knowing that most of the trapped crevice mass, especially that released early, is oxidized in the expansion stroke, it becomes necessary to look at the effect of late oxidation on engine work output. To quantify this effect a curve showing the sensitivity of indicated mean effective pressure to the heat release schedule was computed, and is reproduced in Figure 4 below [32]. This curve has been obtained by perturbing the burn curve $x(\theta)$ with a delta function of a small amount of extra mixture burned at a sequence of crank angles from spark to EVO. This curve shows how substantially little the crevice gas oxidation during the exhaust stroke contributes to engine work output. Thus, the unburned mixture trapped in the piston crevice escaping primary combustion causes a significant degradation of engine efficiency.

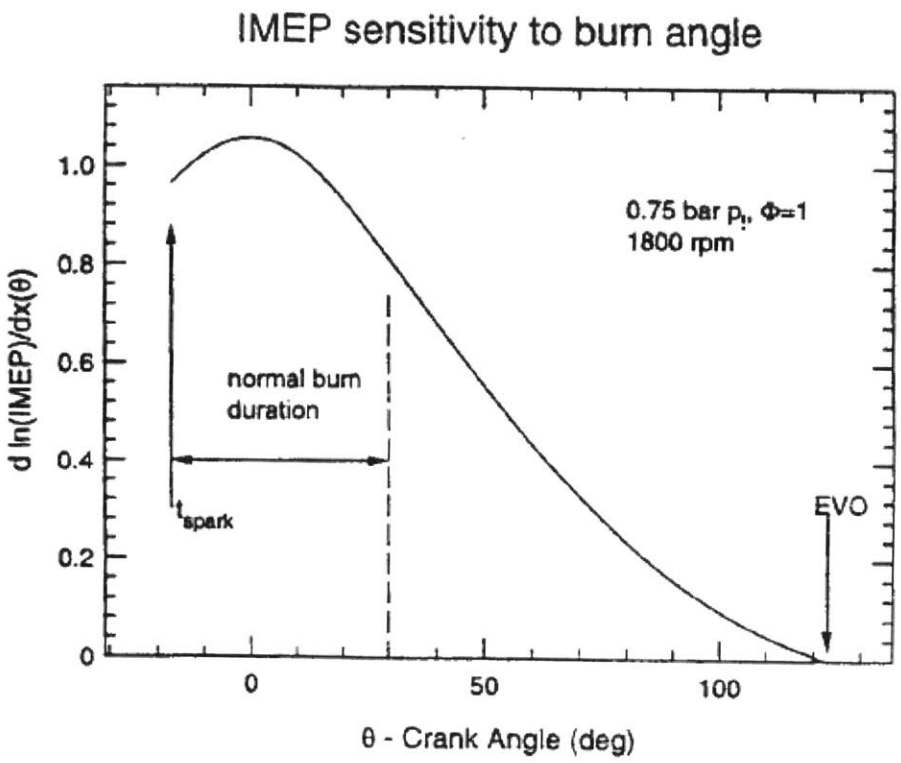

Figure 1-4 Indicated mean effective pressure sensitivity to burn angle. dln(imep)/dx(θ) denotes the percentage change in imep due to a 1 percent additional mass burned at crank angle θ. During the normal burn duration it has a value of about 1.0 [32].

1.5 Crevice Effect on Emissions

Nearly the entirety of previous research on engine crevices has been focused on unburned hydrocarbon emissions. Beginning in 1970 Daniel validated an analytical model with engine experiments to look at crevice quenching, post flame oxidation, exhaust of burned products, and oxidation in the exhaust system [17]. Wentworth then went on to show that the virtual elimination of piston crevices can result in a 47-74 percent reduction in hydrocarbon emissions [33]. Adamczyk used combustion bombs and gas chromatography to quantify different crevice contributions to emissions, showing the importance of the piston crevice [12]. Cheng then completed a broad and thorough study quantifying all of the different hydrocarbon emissions

mechanisms in an SI engine for warmed up and cold start conditions [32]. Min altered piston and head gasket crevices to study their sensitivities with regard to hydrocarbon emissions, showing that the piston crevice had a very small effect on hydrocarbon emissions [28]. Thompson similarly experimented with different piston and ring combinations, employing natural gas to isolate crevice mechanisms, to conclude that hydrocarbon emissions did not change significantly with different piston crevices [34]. Sterlepper used optical-fiber experiments to look at flame entrance into crevices and actually saw that a bigger piston-cylinder clearance resulted in less hydrocarbon emissions due to greater flame penetration [15]. Finally, Boam gave a useful overview of hydrocarbon emissions during the cold start period of engine operation [35].

1.6 Compression Ratio Effect on Efficiency

Increasing compression ratio is a well-known way to improve engine efficiency. These compression ratio increases are predominantly limited by knock concerns at maximum engine load, and this limit is especially noticeable in turbo-downsized engines, where production engine compression ratios lag behind similar naturally aspirated engines. Various fuel and engine control strategies can be employed to abate knock and realize efficiency gains from increasing compression ratio.

As a first look at the compression ratio effect on efficiency an ideal gas constant-volume cycle is investigated. The working fluid in this case has constant specific heat capacities. The cycle consists of an isentropic compression, constant volume heat addition, isentropic expansion, and constant volume heat rejection. The efficiency in this cycle is related to compression ratio in Equation 1.4:

$$\eta_{f,ig} = 1 - \frac{1}{r_c^{\gamma-1}} \qquad [1.4]$$

where $\eta_{f,ig}$ is the indicated gross fuel conversion efficiency, r_c is compression ratio, and γ is the ratio of specific heats. This model gives a very simple relation between compression ratio and efficiency to show that efficiency increases with increased compression ratio. In this cycle many real-engine effects are neglected.

To give a more accurate estimate of the effect of compression ratio on engine efficiency a fuel-air cycle analysis can be used. In this cycle fluid properties and combustion chemistry are taken into account. The working fluid no longer has constant specific heat capacities and its composition changes within the cycle. Results of the fuel-air cycle for various compression ratios and equivalence ratios are shown in Figure 1-5. These results show that indicated efficiencies increase at an ever decreasing rate with increasing compression ratio.

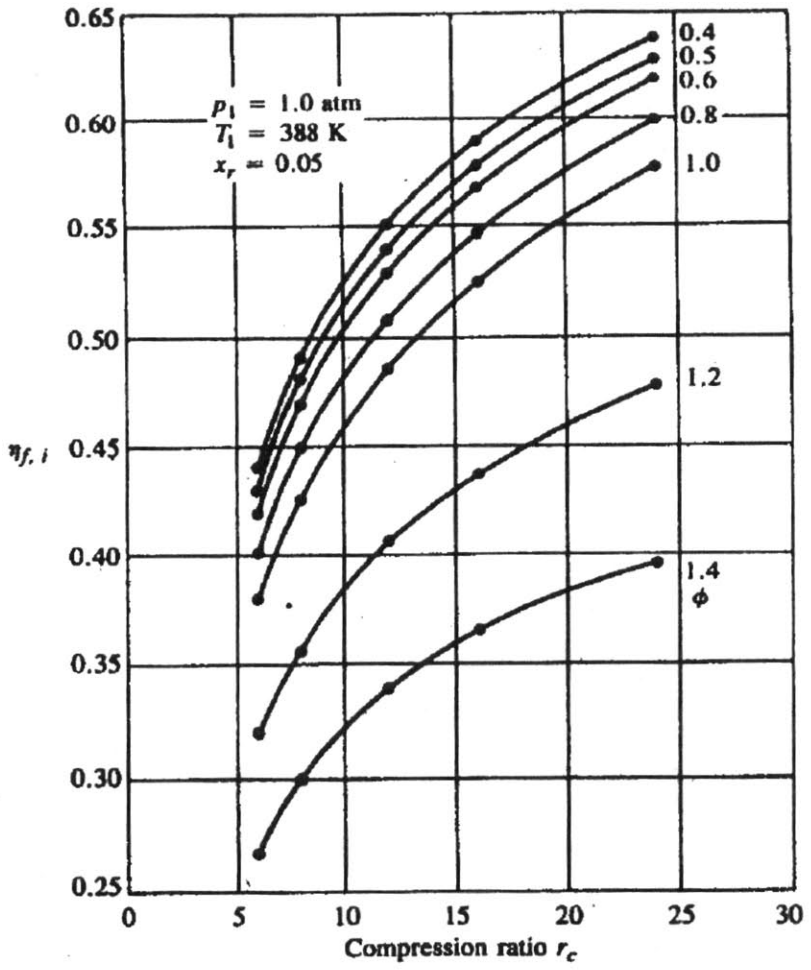

Figure 1-5 Fuel-air cycle results for indicated fuel conversion efficiency as a function of compression ratio and equivalence ratio. Fuel: octane; $p_1 = 1\,atm$, $T_1 = 388\,K$, $x_r = 0.05$ [23].

The fuel-air cycle still leaves out many important engine-related variables when calculating efficiency. Some of these include heat transfer, crevice effects, and burning characteristics. All of these factors lead to a lower increase in indicated efficiency with compression ratio increase than that predicted by the fuel-air cycle analysis. A more realistic and modern look at efficiency changes with compression ratio is given by experimental engine results shown in Figure 1-6. In this plot changes are normalized by those at the lowest compression ratio tested and are significantly lower than those predicted with the fuel-air cycle analysis.

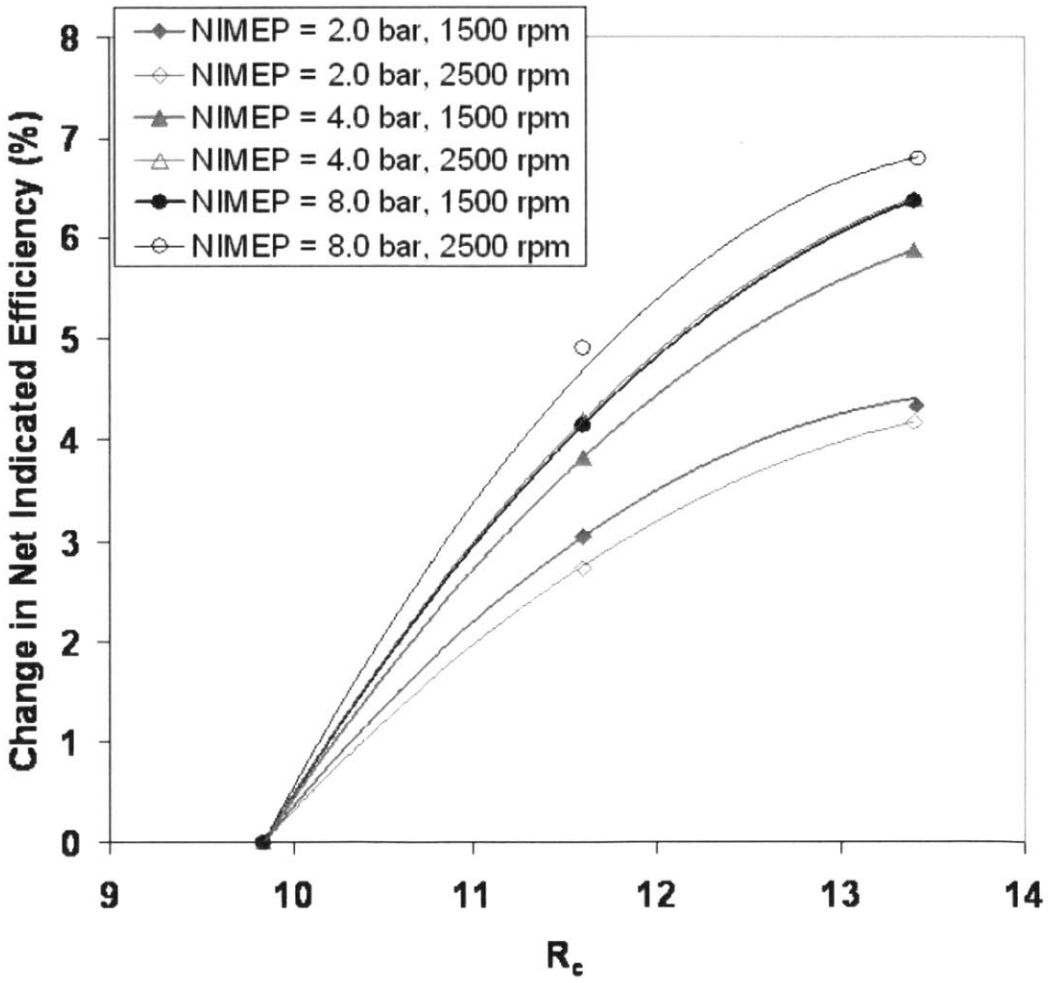

Figure 1-6 Normalized change of net indicated efficiency with compression ratio; lambda=1.0 [36].

1.7 Research Objectives

The objectives of this study are as follows:

1. To understand the loss mechanisms on engine efficiency associated with engine downsizing, with a focus on crevice loss.

2. To experimentally quantify the piston crevice effect on indicated efficiency for a warmed up engine operating at various loads, speeds, and coolant temperatures.

3. To test and verify the effects of the piston crevice on engine out hydrocarbon emissions.

4. To investigate compression ratio effects on indicated efficiency and crevice loss.

5. To recommend a viable course for future engine piston design with a focus on top land height.

This page intentionally left blank

2 Efficiency Simulation Study

2.1 Introduction

As mentioned previously, turbocharged downsized engines have been instituted as a means of increasing engine efficiency. To better understand the efficiency loss mechanisms and how they scale with different engine displacements a simulation study has been completed [37]. Of particular interest is the behavior of the crevice loss, which increases with downsizing because of disproportionate scaling of the crevice gap with engine displacement. This study quantifies the loss mechanisms on engine efficiency using a cycle simulation model containing a friction and crevice model.

2.2 Methodology

In this study engine downsizing is simulated by reducing individual cylinder size. Bore to stroke ratio is kept constant, while engine displacement is reduced from 500 cc/cylinder to 300 cc/cylinder. This constitutes a significant reduction in engine displacement from modern naturally aspirated engines. A standard setup for a modern naturally aspirated engine is used as a baseline in this study with details given in Table 1 below. Throughout this study bore/stroke ratio, con rod/stroke ratio, number of valves, and valve timing are set to baseline values.

Table 2-1 Typical modern naturally aspirated engine geometry used as baseline engine in simulation study.

Displacement Volume/cylinder	500 cc
Compression Ratio	10:1
Bore (mm)/Stroke(mm)	86/86
Connecting Rod to Stroke ratio	1.58
Number of Valves	16
Intake Valve Open	0° BTDC-intake
Intake Valve Close	60° ABDC-intake
Exhaust Valve Open	45° BBDC –exhaust
Exhaust Valve Close	10° ATDC –exhaust

In addition to downsizing crevice loss is expected to change with compression ratio, so this simulation study looks at compression ratio changes ranging from 8 to 20. Finally, two load cases are investigated keeping brake torque output per cylinder at 13.4 Nm for part load and 43.6 Nm for full load. For the reference engine, these torque values correspond to BMEP values of 3.4 and 11 bar, respectively. A summary of the parameters used in this study is presented in Table 2-2.

Table 2-2 Various test parameters used in simulation study.

Displacement Volume/cylinder	300, 400,500 cc
Compression Ratio	8, 12, 16, 20
λ	1
Speed	1600 rpm
Load (as measured by brake torque)	Part (13.4 Nm/cyl); Full (43.6 Nm/cyl)
Spark timing	MBT

Spark timing is fixed at MBT timing so that different cases have similar combustion phasing. In practice, especially at high loads and high compression ratios, spark timing must be retarded for knock. Relaxing this restraint provides a useful upper bound on performance assuming a knock resistant fuel, such as E85 or M85, or a knock abatement strategy [38] is implemented.

Combustion is modeled by using a Wiebie function for the cumulative mass fraction burn profile. Burn duration is 65 crank angle degrees for part load and 55 crank angle degrees for full load, which ensures the heat release schedule is the same across each load.

The exhaust pressure is kept at 1.05 bar for non-boosted operation. When the engine is boosted, the pumping loss depends on the characteristics of the compression system which determines the intake and exhaust pressure. For example, when the intake pressure is higher than the exhaust, the pumping work could be negative (work output in the gas exchange process). To decouple this issue from the discussion, the exhaust pressure is set to the same value as the intake pressure when the engine is boosted so that pumping work is only due to the

valve flow losses. The actual pumping work corresponding to the proper matching of the engine and compression system is to be addressed separately.

2.2.1 Friction Model

Engine friction is calculated using a model developed by Patton, Nitschke, and Heywood [39], which has been updated by Sandoval and Heywood [40]. This model is based on an in-line 4-cylinder configuration with 4 valves per cylinder and double-overhead-cams. It estimates friction from components such as the crank shaft, piston rings and skirt, cam shafts, and valves. These components scale geometrically with bore size. Friction values are apportioned to each cylinder via the frictional mean effective pressure. Pumping and accessory losses are not included in the friction model. The former is already incorporated in the cycle simulation, and is accounted for in the net indicated output. The latter is very much technology dependent (e.g. fuel pumping power for PFI versus DI), and is best left for a separate assessment.

2.2.2 Crevice Model

The piston crevice is by far the most important crevice and so, to simplify the analysis, it is the only crevice modeled. For durability reasons the top land height is taken to be 6 mm. Radial clearance between the piston and liner is estimated based on thermal expansion considerations presented earlier in 1.3.2. The side and back top ring volumes are assumed to be a fixed fraction of the top land volume. The full crevice specifications are shown in Table 3.

Table 2-3 Crevice Geometry at part and full load points.

	Part Load	Full Load
Brake Torque (Nm/ cylinder)	13.37	43.63
Avg Piston Temperature (K)	430	490
Avg Liner Temperature (K)	360	390
Head Temperature (K)	380	415
Crevice Temperature (K)	425	480
Top land / liner clearance (mm)	0.300	0.270
Side and Back Top Ring Volume/Top Land Volume	0.65	0.7
Top land height (mm)	6	6

In analyzing the crevice effect on engine efficiency it is important to know how much unburned-mixture has escaped primary oxidation. This study assumes that flame arrival coincides with the peak pressure point, which results in a maximum for trapped crevice mass. Since the crevice volume is in pressure equilibrium with the combustion chamber this peak crevice mass can be found using Equation 2.1:

$$m_{crev} = \frac{(p_{peak} - MAP)V_{crev}}{R_u T_{crev}} \quad [2.1]$$

where m_{crev} is the mass trapped in the crevice, p_{peak} is peak pressure, MAP is manifold absolute pressure, V_{crev} is crevice volume, R_u is the unburned gas constant, and T_{crev} is crevice gas temperature. The fuel mass trapped in the crevice is then calculated from m_{crv} based on the air-fuel ratio and residual gas fraction.

After primary oxidation has completed, in-cylinder pressure decreases and trapped crevice mixture is released into the combustion chamber. Based on crevice outflow and oxidation considerations explained in Chapter 1, full and instant oxidation is assumed as crevice mixture is released. This assumption is combined with the heat release schedule sensitivity curve from Figure 1-4 to find the efficiency of the secondary crevice oxidation.

The increase in GIMEP due to the in-cylinder secondary crevice oxidation is small compared to the overall GIMEP. Therefore, the change in GIMEP is approximated by Equation 2.2:

$$\Delta GIMEP = GIMEP \int_{outflow} \frac{d\ln(GIMEP)}{dx} \frac{dx}{dm_f} \frac{dm_f}{d\theta} d\theta \quad [2.2]$$

where GIMEP is the gross indicated mean effective pressure, x is mass fraction burned, m_f is fuel mass, and θ is crank angle. Since $dx/dm_f = 1/m_f$, the gross indicated efficiency from the secondary oxidation is given by Equation 2.3:

$$\eta'_{i,g} = \frac{\Delta GIMEP * V_d}{Q_{LHV} \int_{outflow} \frac{dm_{f,crev}}{d\theta} d\theta} = \eta_{i,g} \left[\frac{\int_{outflow} \frac{d \ln(GIMEP)}{dx} \frac{dm_{f,crev}}{d\theta} d\theta}{\int_{outflow} \frac{dm_{f,crev}}{d\theta} d\theta} \right] \quad [2.3]$$

where $\eta'_{i,g}$ is the gross indicated efficiency of burning crevice gas, V_d is displacement volume, Q_{LHV} is the lower heating value of the fuel, and $m_{f,crev}$ is the mass of fuel in the crevice. Figure 2-1 shows the heat release schedule sensitivity curve [32] alongside the crevice outflow [28,29] (positive for outflow; negative for inflow) for the reference engine at part load (see Table 2-3 for crevice condition). The value of the square bracket term in [2.3] is simply the integral of product of these two curves during the crevice outflow divided by the integral of the crevice outflow. The value of the square bracket comes out to 0.62, which is rounded off to a nominal value of 0.6. This nominal value of $\eta'_{i,g}$ is equal to 60% of the average overall fuel conversion efficiency, and this is emphasized in Equation 2.4. It is also insensitive to load, and is used for both the part load and full load calculation. It is important to remember that this value for $\eta'_{i,g}$ is an upper estimate since it was assumed that all crevice mixture is oxidized instantaneously upon crevice exit.

$$\eta'_{i,g} = \eta_{i,g} * [0.6] \quad [2.4]$$

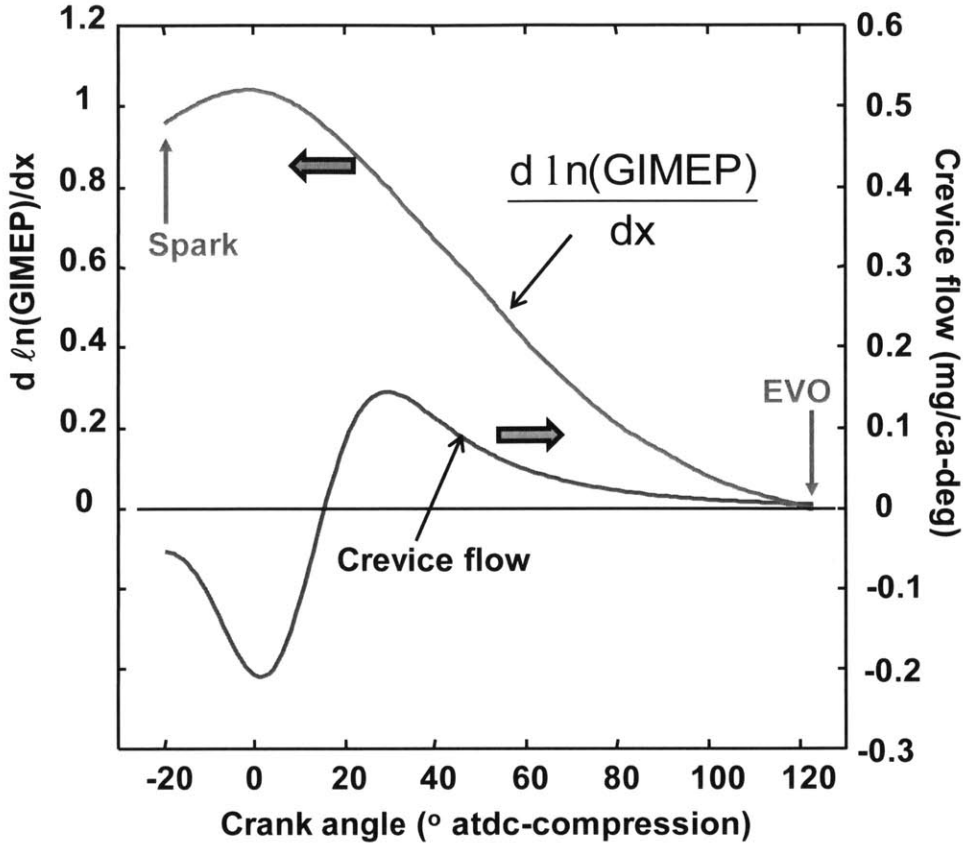

Figure 2-1 Sensitivity of GIMEP to heat release schedule plotted alongside crevice outflow of reference engine (see Table 2-1) operating at part load (see Table 2-3).

2.2.3 Work Accounting

The brake work output comprises the gross work minus the losses and is displayed in Equation 2.5:

$$W_{brake} = W_{g,s} - E_{crev}(\eta_{i,g} - \eta'_{i,g}) - W_p - W_f \qquad [2.5]$$

Here, $W_{g,s}$ is the indicated gross work output of the engine obtained from the cycle simulation without the crevice loss. The second term on the right hand side represents the work loss due to the crevice presence: E_{crev} is the fuel energy of the trapped fuel in the crevice volume at peak pressure, calculated from Equation 2.1 by accounting for A/F and residual fraction; $\eta_{i,g}$

is the gross indicated fuel conversion efficiency of the charge; $\eta'_{i,g}$ is the gross indicated fuel conversion efficiency of the crevice mass from secondary oxidation. The pumping and friction work losses are W_p and W_f. In the following results, the work loss terms are normalized by the fuel energy.

2.3 Part Load Results

2.3.1 Pumping Loss

The manifold absolute pressure (MAP) is varied to match indicated torque per cylinder, and is presented in Figure 2-2 for the part load case. As the engine is downsized, MAP must increase to allow a similar mass of air at the smaller displacement volume. As compression ratio is increased the engine becomes more efficient and so MAP decreases slightly to match the load. Even at the lowest compression ratio and displacement volume the engine is still throttled.

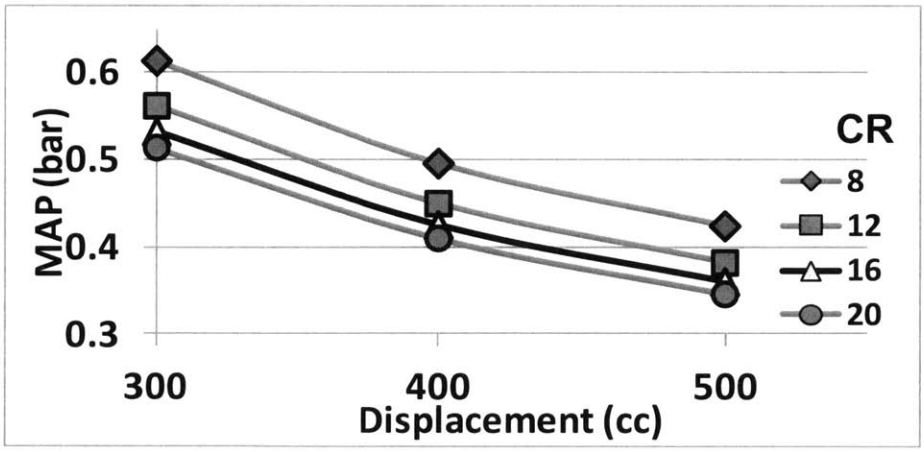

Figure 2-2 Manifold absolute pressure at part load condition.

Pumping work per unit fuel energy follows MAP trends very closely and is displayed in absolute terms for the part load case in Figure 2-3 (a). These values are normalized by those at V_d = 500 cc per cylinder and are shown in Figure 2-3 (b).

With downsizing the reduction in pumping work per fuel energy is significant and amounts to 1.5-2 %-points per 100 cc decrease in per cylinder V_d. The normalized values are insensitive

to compression ratio and are approximately linear with changing displacement volume. A decrease in per cylinder V_d of 100 cc results in a 25 % decrease in the normalized pumping work per fuel energy.

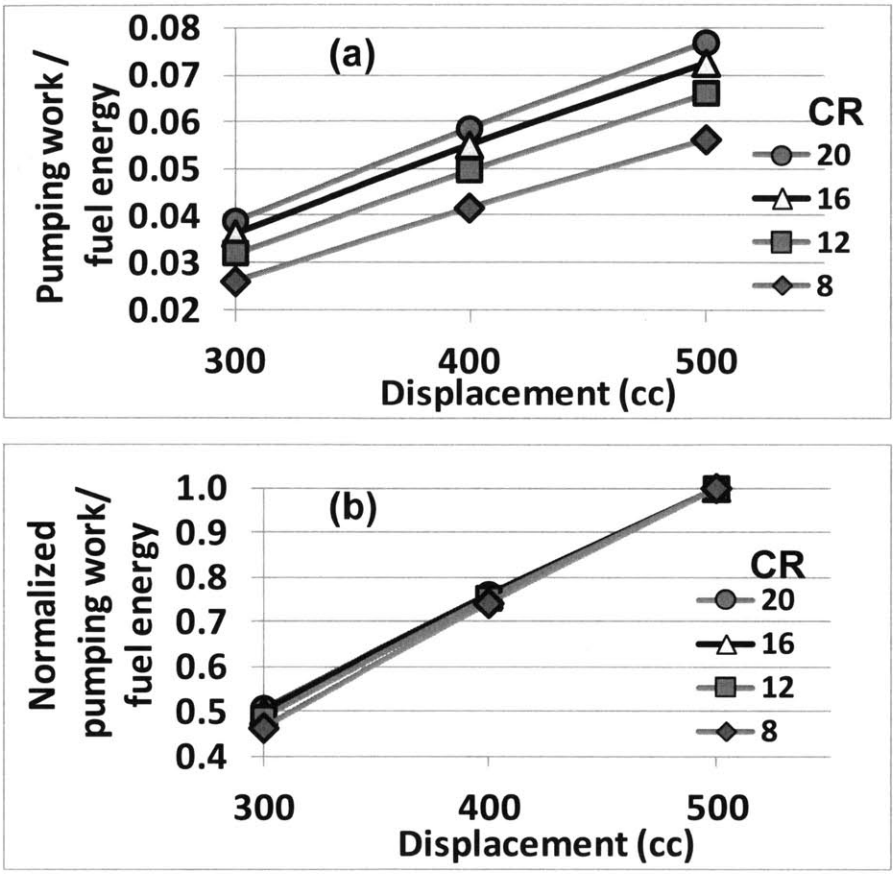

Figure 2-3 Pumping work at part load; (a) pumping work/fuel energy; (b) values of (a) normalized by those at 500 cc V_d.

2.3.2 Friction Loss

Component friction work per fuel energy at the part load condition is shown in Figure 2-4 (a), with values normalized by those at V_d = 500 cc per cylinder in Figure 2-4 (b). For a fixed torque, the fuel energy supplied is approximately the same. The friction term consists of (i) contribution from parts such as the crank seal and valve train which are independent of the gas load, and (ii) from parts dependent on the gas load, such as the gas load sensitive parts of the ring and piston skirt friction. Note that the non-gas load sensitive parts of the ring and skirt have been separated out to (i). The relative magnitude of (i) to (ii) is approximately 9 to 1.

With engine downsizing, there is less surface area so (i) decreases, but more gas loading with higher MAP values so (ii) increases. Taking into account the aforementioned ratio of (i) to (ii) there is a net decrease in friction work per fuel energy with engine downsizing.

As compression ratio is increased the friction work per fuel energy increases. This is due partly from the increase associated with higher gas loading, but mainly from the decrease in fuel energy supplied due to a higher indicated efficiency at the higher compression ratio.

With downsizing the reduction in friction work per fuel energy amounts to 0.75 %-points per 100 cc decrease in per cylinder V_d. The normalized values are insensitive to compression ratio. A decrease in per cylinder V_d of 100 cc results in a 10-13 % decrease in the normalized friction work per fuel energy.

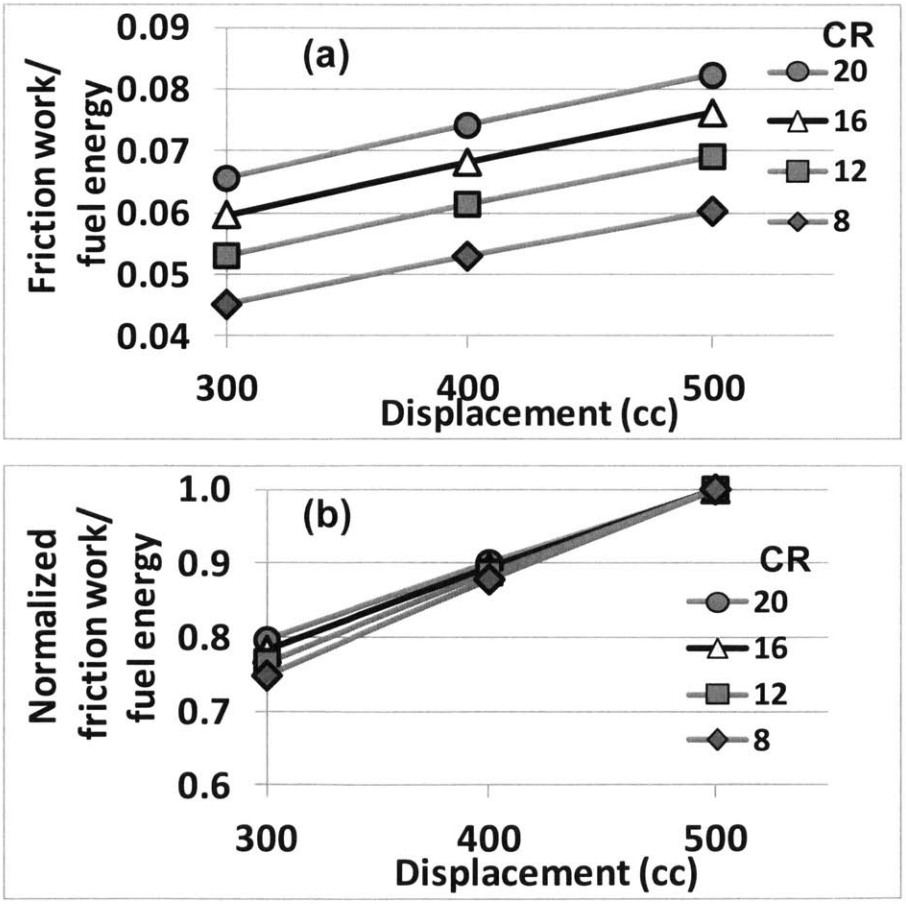

Figure 2-4 Component friction work at part load; (a) friction work/fuel energy; (b) values of (a) normalized by those at 500 cc V_d.

2.3.3 Heat Loss

Heat loss per fuel energy at the part load condition is shown in Figure 2-5. As the engine is downsized heat loss per fuel energy decreases by 1 %-point per 100 cc decrease in per cylinder V_d. This result is roughly independent of compression ratio.

The heat loss term is independent of the compression ratio because of the charge temperature behavior with compression ratio change. This behavior is shown in Figure 2-6, in which the pressure, unburned gas temperature, and burned gas temperature are plotted for compression ratios of 8 and 20. The major factor in heat loss calculations is the burned gas temperature. For the higher compression ratio the burned gas temperature reaches is higher during compression and combustion, but quickly drops below the low compression ratio value during the expansion stroke. Thus, the higher heat transfer at the beginning of the cycle is compensated by the lower heat transfer later on in the cycle. The net result, which has also included the effects of pressure and surface area, is that the overall heat loss is insensitive to compression ratio.

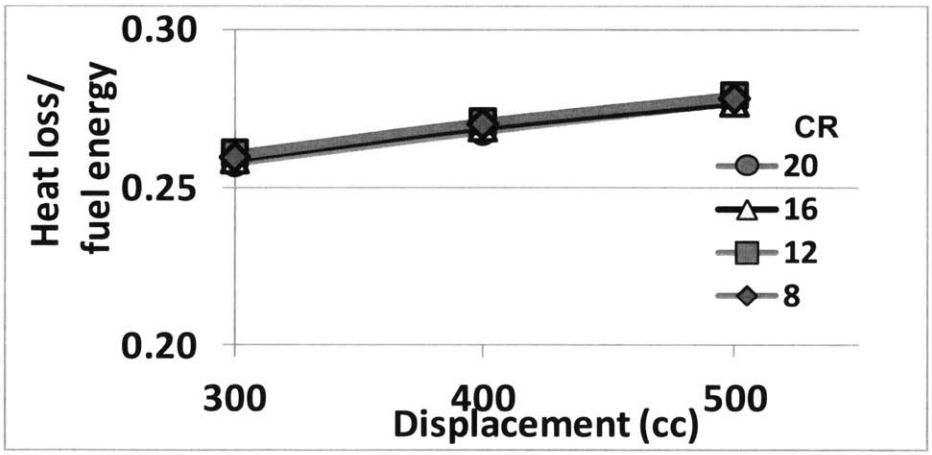

Figure 2-5 Heat Loss per fuel energy at part load.

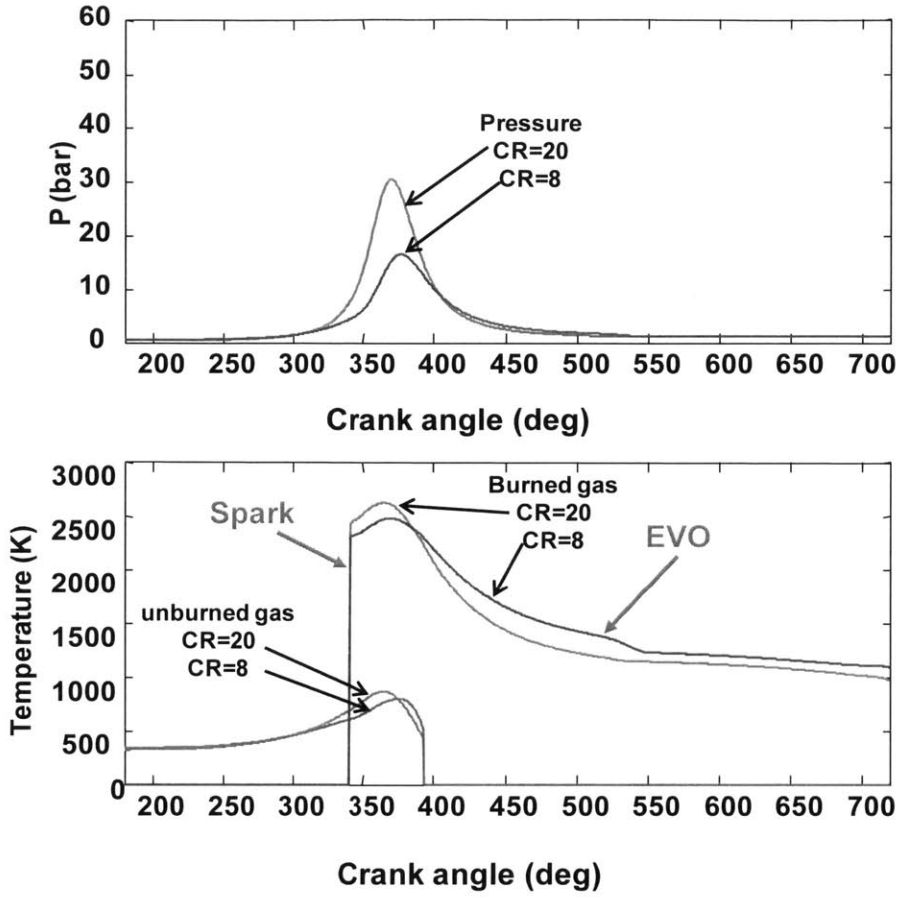

Figure 2-6 Charge behavior for CR=8 and 20 at part load.

2.3.4 Crevice Loss

Crevice loss per fuel energy at the part load condition is shown in Figure 2-7 (a), with values normalized by those at V_d = 500 cc per cylinder in Figure 2-7 (b).

With engine downsizing, as cylinder displacement is decreased crevice volume decreases at a slower rate due to thermal expansion concerns described in Chapter 1. At higher compression ratios clearance volume is decreased while crevice volume remains constant, meaning a larger proportion of the unburned mixture will be trapped in the crevice during flame quenching at the crevice entrance. The magnitude of the crevice work loss is significant and is equal to a few percent of the fuel energy.

With engine downsizing the increase in crevice work loss per fuel energy amounts to 0.5 %-points per 100 cc decrease in per cylinder V_d. The normalized values are insensitive to compression ratio. A decrease in per cylinder V_d of 100 cc results in a 20 % decrease in the normalized crevice work loss per fuel energy.

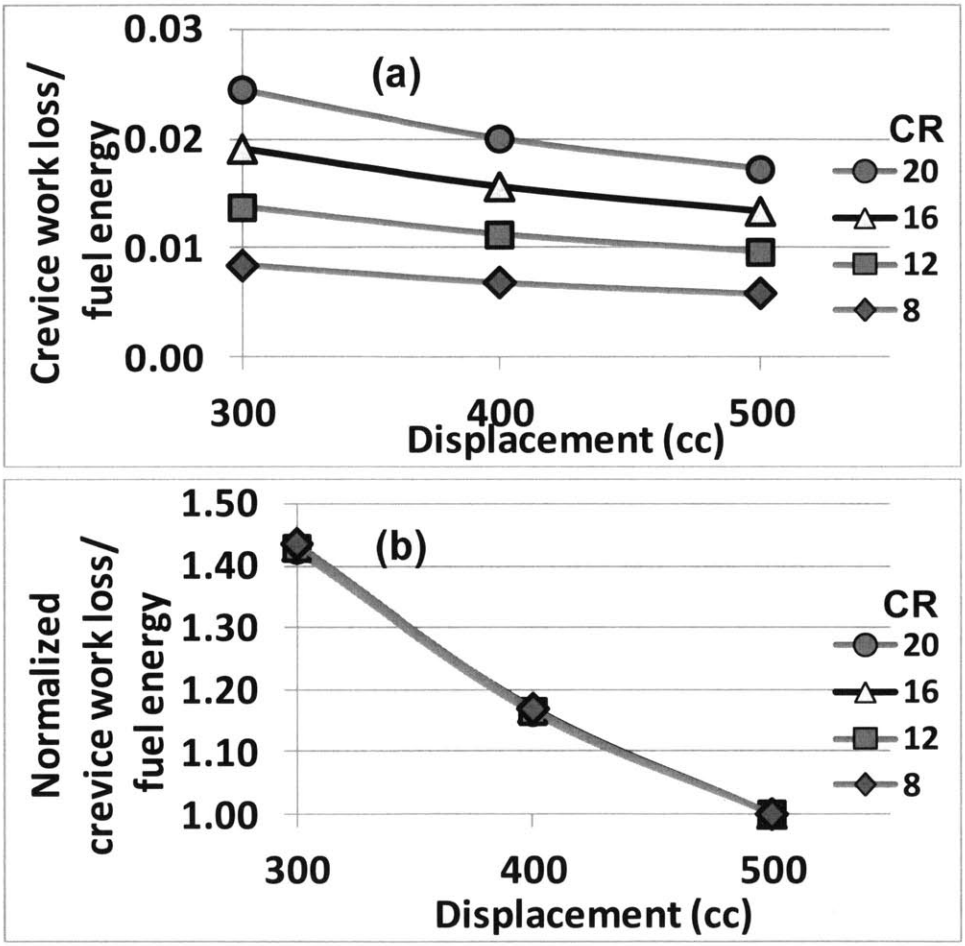

Figure 2-7 Crevice work at part load; (a) crevice work loss/fuel energy; (b) values of (a) normalized by those at 500 cc V_d.

2.3.5 Brake Efficiency

Brake conversion efficiency at the part load condition is shown in Figure 2-8 (a), with values normalized by those at V_d = 500 cc per cylinder in Figure 2-8 (b).

Downsizing results in higher brake efficiencies due to the combination of factors presented thus far. Increased compression ratio results in higher brake conversion efficiency at an ever diminishing rate, mainly due to pumping and friction considerations.

With downsizing the increase in brake conversion efficiency amounts to 2.5 %-points per 100 cc decrease in per cylinder V_d. The normalized values are insensitive to compression ratio and approximately linear. A decrease in per cylinder V_d of 100 cc results in a 10 % increase in brake conversion efficiency.

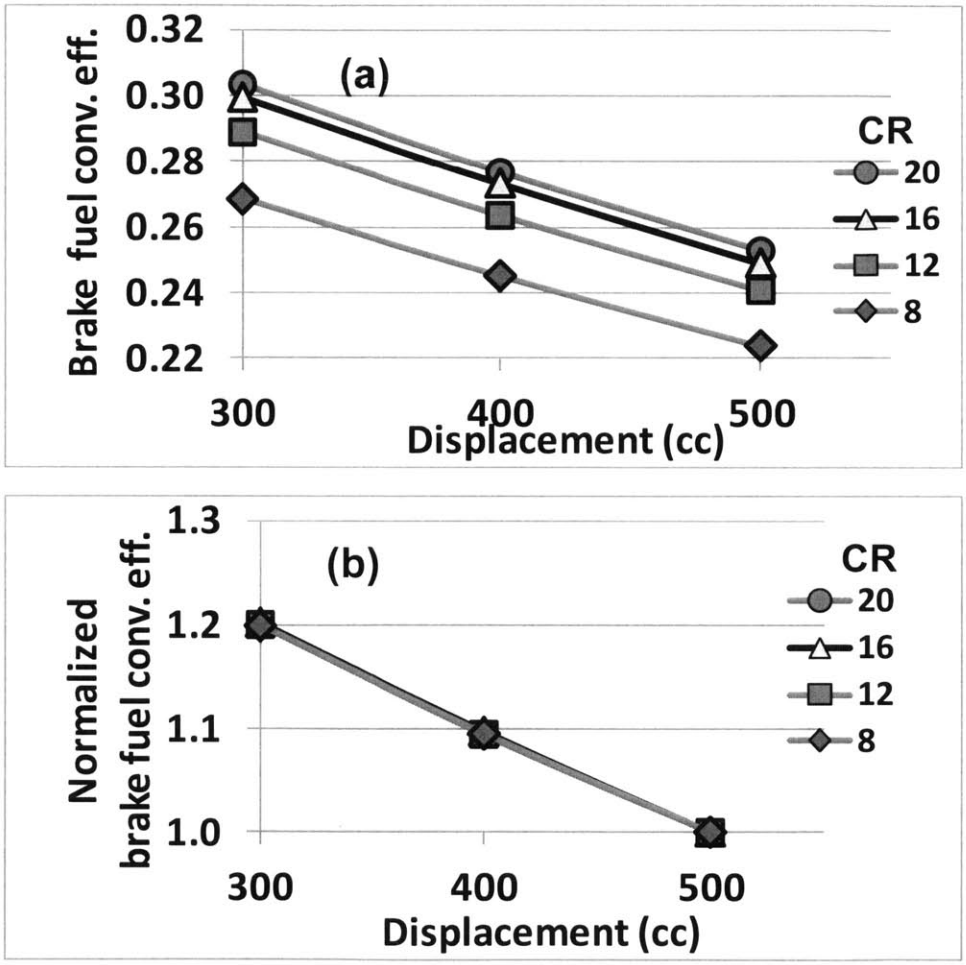

Figure 2-8 Brake fuel conversion efficiency at part load; (a) pumping work/fuel energy; (b) values of (a) normalized by those at 500 cc V_d.

2.3.6 Component Breakdown

The work output has been broken down into the components discussed thus far for the CR=8 and CR=20 part load cases. The CR=8 part load deconstruction is shown in Figure 2-9 and the CR=20 part load deconstruction is shown in Figure 2-10. In the following, work will be discussed as a fraction of the fuel energy. In both compression ratio cases, the gross indicated work remains approximately the same as the engine is downsized. The gain in brake work is due to the reduction of pumping work and friction work. The crevice loss increases with decreasing displacement volume and is especially significant in the high compression ratio case.

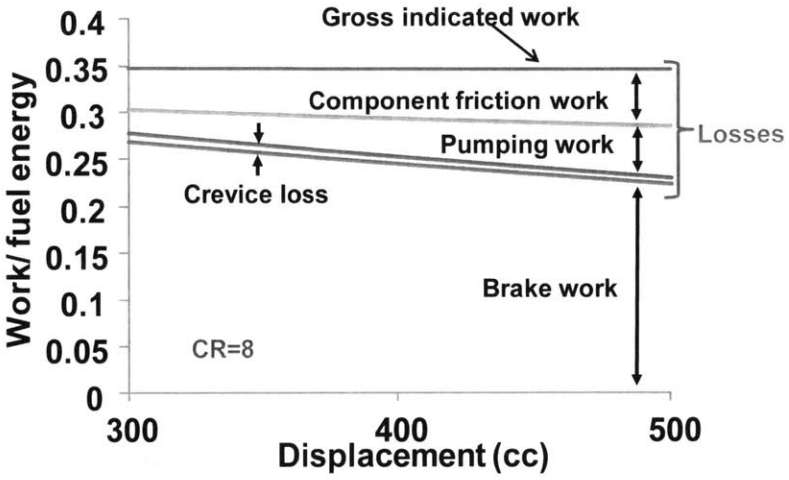

Figure 2-9 Deconstruction of engine work output at part load; CR=8, 1600 rpm.

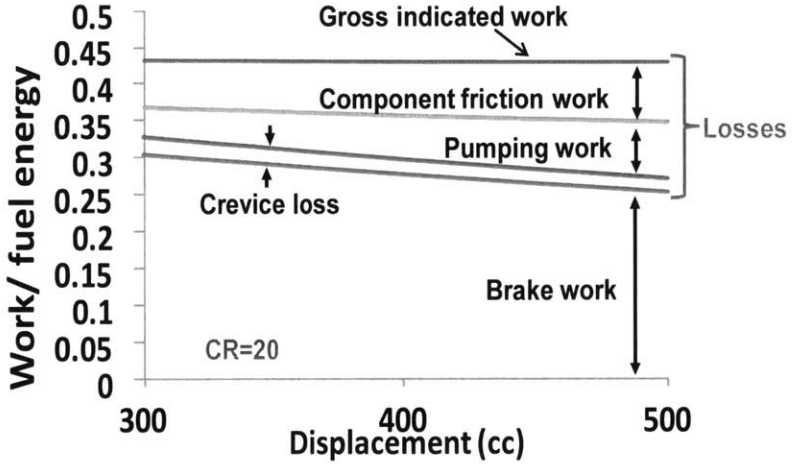

Figure 2-10 Deconstruction of engine work output at part load; CR=20, 1600 rpm.

2.4 Full Load Results

2.4.1 Pumping Loss

MAP is varied to match full load torque per cylinder and is shown in Figure 2-11. For most of the cases tested the engine operates under boosted conditions. For these boosted cases the exhaust pressure is matched to MAP to eliminate all pumping loses save those from valve flow loss (which are very small). For the non-boosted cases exhaust pressure is kept at 1.05 bar. The pumping work per fuel energy for the full load condition is shown in Figure 2-12.

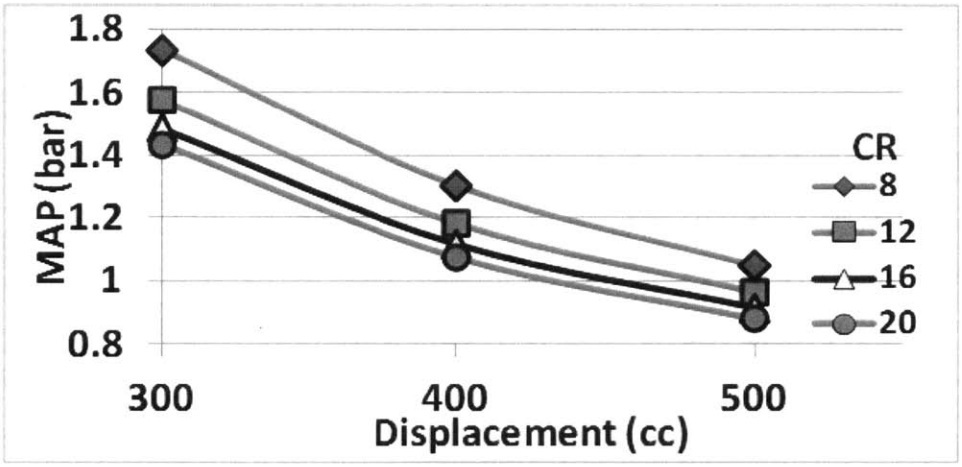

Figure 2-11 Manifold absolute pressure at full load.

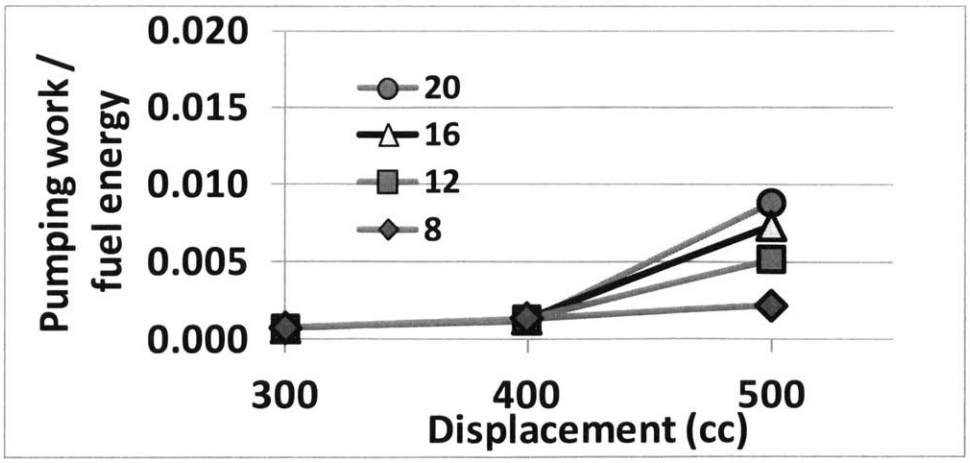

Figure 2-12 Pumping work per fuel energy at full load.

2.4.2 Friction Loss

Component friction work per fuel energy at the full load condition is shown in Figure 2-13 (a), with values normalized by those at V_d = 500 cc per cylinder in Figure 2-13 (b). The friction work per unit fuel energy is approximately half of that at part load, and it decreases approximately linearly with decreasing displacement volume.

With downsizing the reduction in friction work per fuel energy amounts to 0.34 %-points per 100 cc decrease in per cylinder V_d. This same 100 cc decrease results in an 8-12 % decrease in the normalized friction work per fuel energy, with the slightly larger decrease being at lower compression ratio.

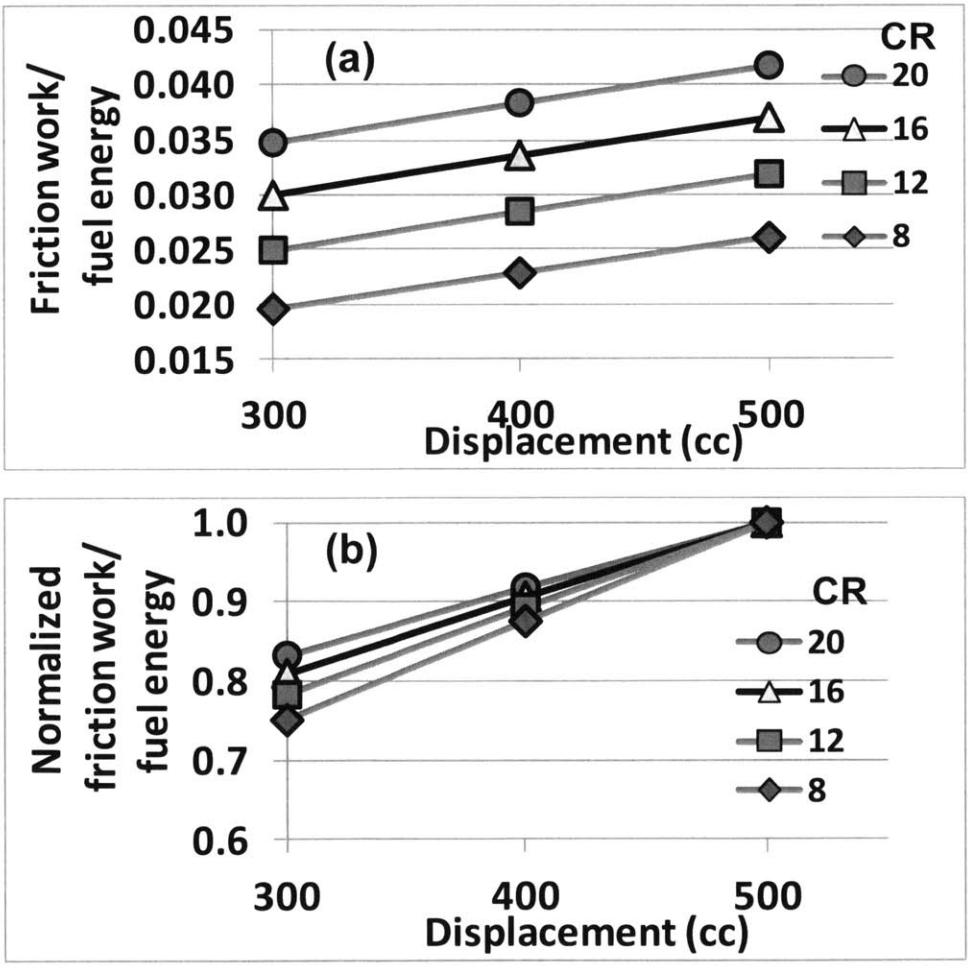

Figure 2-13 Friction work at full load; (a) friction work/fuel energy; (b) values of (a) normalized by those at 500 cc V_d.

2.4.3 Heat Loss

Heat loss per fuel energy at the full load condition is shown in Figure 2-14. These values are approximately 6 %-points lower than corresponding part load values and are insensitive to compression ratio. As the engine is downsized heat loss per fuel energy decreases by 0.75 %-point per 100 cc decrease in per cylinder V_d.

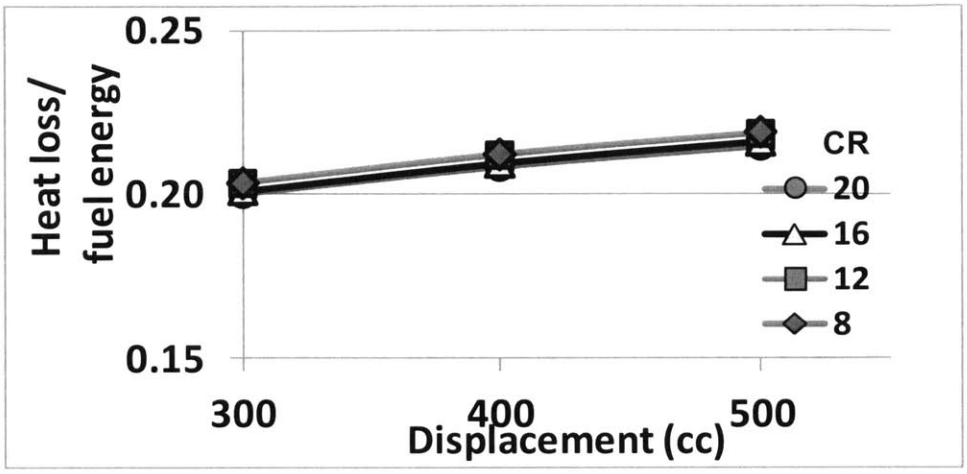

Figure 2-14 Heat loss per fuel energy at full load.

2.4.4 Crevice Loss

Crevice loss per fuel energy at the part load condition is shown in Figure 2-15 (a), with values normalized by those at V_d = 500 cc per cylinder in Figure 2-15 (b). These plots are nearly identical to those from the part load case due to the fact that crevice fuel mass as a fraction of the charge fuel mass is almost independent of load. At the higher load, crevice volume is smaller, crevice temperature is higher, and peak pressure is higher; these effects result in the fuel mass trapped in the crevice remaining a constant fraction of charge fuel mass.

With engine downsizing the increase in crevice work loss per fuel energy amounts to 0.5 %-points per 100 cc decrease in per cylinder V_d. The normalized values are insensitive to compression ratio. A decrease in per cylinder V_d of 100 cc results in a 20 % decrease in the normalized crevice work loss per fuel energy.

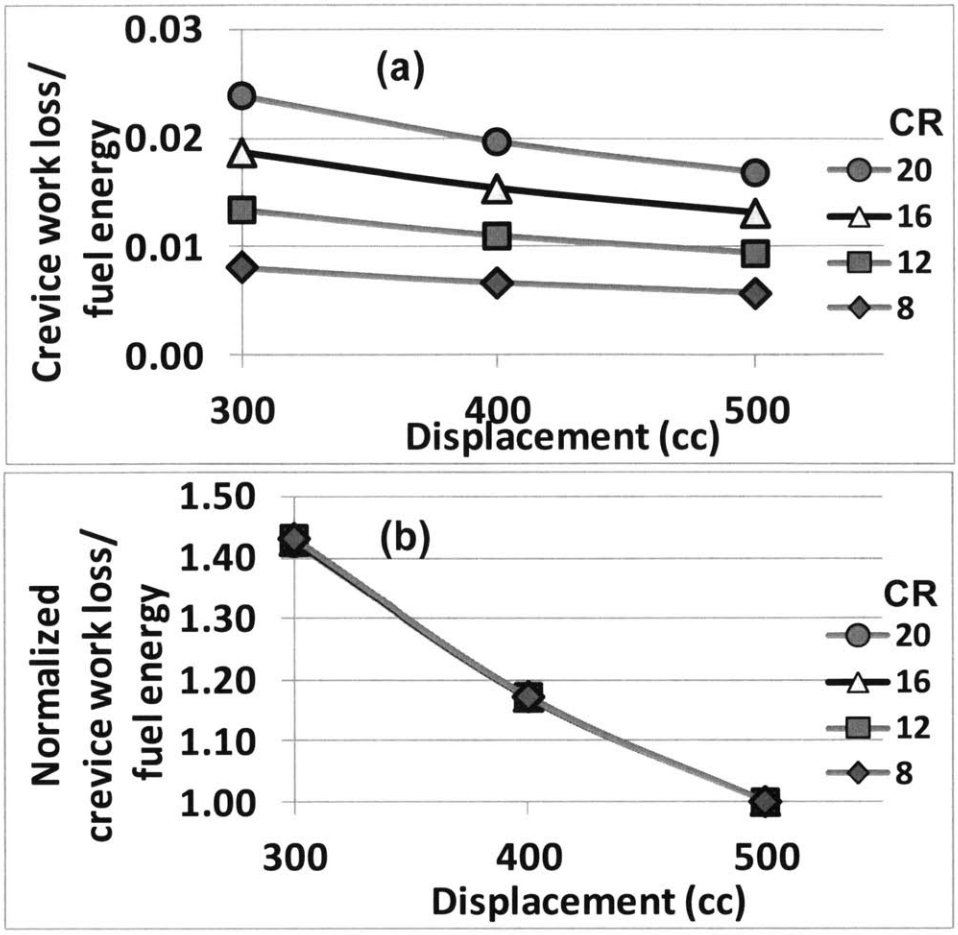

Figure 2-15 Crevice work loss at full load; (a) crevice work loss/fuel energy; (b) values of (a) normalized by those at 500 cc V_d.

2.4.5 Brake Efficiency

Brake conversion efficiency at the full load condition is shown in Figure 2-16 (a), with values normalized by those at V_d = 500 cc per cylinder in Figure 2-16 (b). The efficiency is significantly higher than that at part load but improvement with downsizing is much smaller.

With downsizing the increase in brake conversion efficiency amounts to 0.7 %-points per 100 cc decrease in per cylinder V_d. This same 100 cc decrease results in a 1.75 % increase in brake conversion efficiency. The CR=8 plot in Figure 2-16 (b) differs from the others because at the normalizing displacement volume of 500 cc per cylinder a compression ratio of 8 does not require boosting to match the full load point. This results in a different reference point for the normalization and so the plot is different.

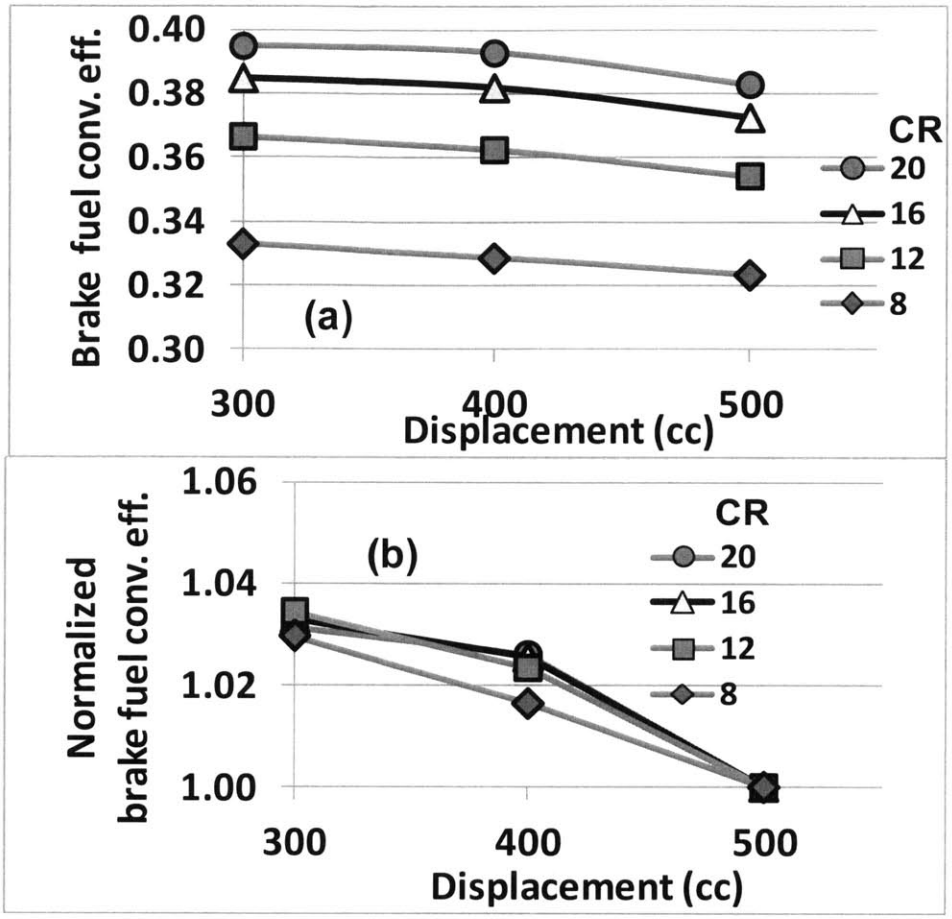

Figure 2-16 Brake fuel conversion efficiency at full load; (a) brake fuel conversion efficiency; (b) values of (a) normalized by those at 500 cc V_d.

2.4.6 Component Breakdown

The work output has been broken down into the components discussed thus far for the CR=8 and CR=20 full load cases. The CR=8 full load deconstruction is shown in Figure 2-17 and the CR=20 full load deconstruction is shown in Figure 2-18. Compared to the part load case the pumping work is nearly insignificant, while the crevice loss becomes more prominent.

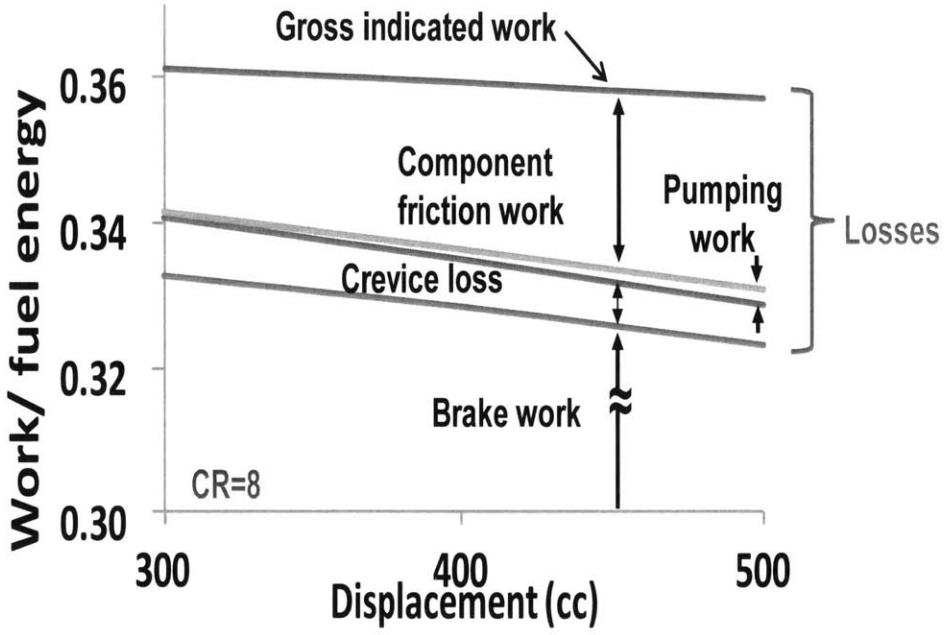

Figure 2-17 Deconstruction of engine work output at full load; CR=8, 1600 rpm.

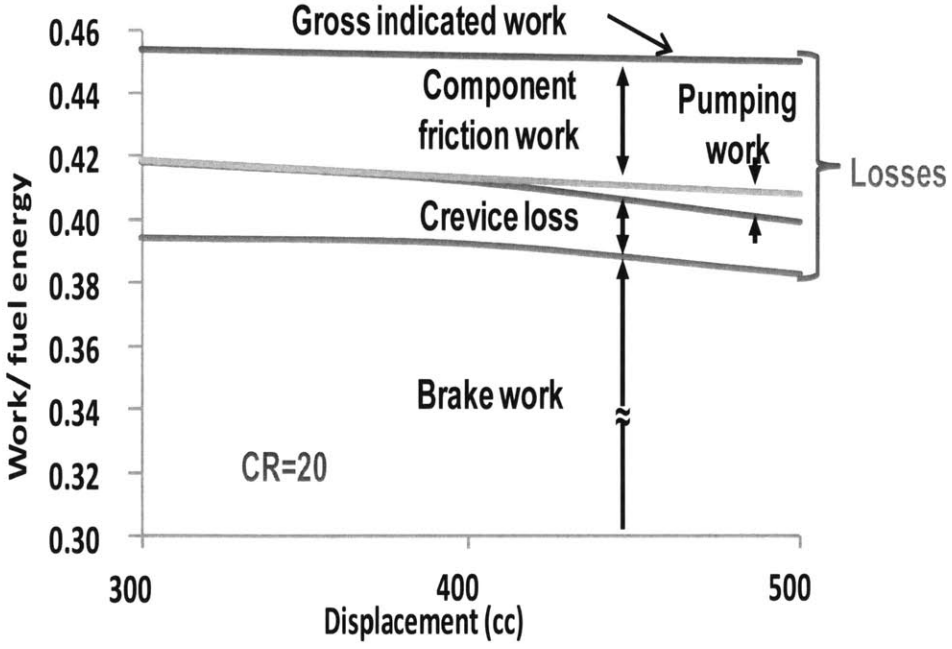

Figure 2-18 Deconstruction of engine work output at full load; CR=20, 1600 rpm.

2.5 Summary and Conclusions

The loss mechanisms associated with engine downsizing and compression ratio change are assessed. Of interest are the extents of friction loss, pumping loss, and crevice loss. These losses are deconstructed via a cycle simulation model which encompasses a friction model and a crevice loss model. Engine displacement is downsized from 500 cc to 300 cc per cylinder and compression ratio is varied from 8 to 20. MAP is changed to match constant torque values per cylinder for part and full load conditions.

The sensitivities of the losses with respect to downsizing are summarized in Table 2-4. These sensitivity values serve as a framework to make assessment of the effects of downsizing on engine losses.

With a focus on crevice loss, the absolute value of the loss on brake conversion efficiency is significant and on the order of a few percent of fuel energy. Crevice loss increases with engine downsizing and compression ratio increase because crevice volume becomes a larger proportion of engine clearance volume. The crevice loss per fuel energy is independent of load since fuel trapped in the crevice as a fraction of total fuel mass is almost constant across load.

Table 2-4 Effect of downsizing on loss mechanism and brake work at part and full load points; 1600 rpm.

	Part load	Full load
Pumping work: W_p / fuel energy	-1.5–2 %-point (~-25% in relative value) per 100cc V_d reduction; insensitive to CR	Pumping work depends on engine/compression system matching. The valve flow losses are small compared to the other losses under boosted operation
Friction work: W_f/ fuel energy	-0.75 %-point (~-10% in relative value) per 100cc V_d reduction	Values are lower than that of the part load by about factor of 2; absolute sensitivity is less: -0.34 %-point (~-10% in relative value) per 100cc V_d reduction
Heat loss: Heat loss/ fuel energy	-1%-point per 100cc Vd reduction; result insensitive to CR	-0.75 %-point per 100cc Vd reduction; result insensitive to CR
Crevice loss: Crevice loss/ fuel energy	+0.5 %-point (+20% in relative value) per 100cc Vd reduction; result insensitive to CR	Value and sensitivity almost identical to part load case, since fuel trapped as fraction of total fuel mass is almost independent of load
Brake fuel conversion efficiency	+2.5 %-point (+10% in relative value) per 100cc Vd reduction; result insensitive to CR	Efficiency is higher at full load, but sensitivity to downsizing is lower: +0.7 %-points (+1.75% in relative value) per 100cc Vd reduction

3 Experimental Method

To investigate and quantify the effects of the piston crevice, compression ratio, and operating conditions on indicated engine efficiency a series of experiments have been completed. These experiments were performed over a broad test matrix on a single cylinder research engine in the Sloan Automotive Laboratory.

3.1 Engine Setup

The experimental setup includes a single cylinder research engine, a variable speed dynamometer, fuel and air supply systems, and various control and data collection equipment.

3.1.1 Engine Specifications

The research engine used consists of a Ricardo MK III single cylinder crankcase with a Volvo B5254 pent-roof, 4-valve, central spark plug cylinder head. Additional engine specifications are given in Table 3-1. This engine setup is representative of modern passenger vehicle engines with regard to bore size, bore to stroke ratio, and valve timing.

Table 3-1 Experimental engine specifications.

Bore [mm]	83
Stroke [mm]	86
Connecting Rod Length [mm]	158
Displaced Volume [cc]	465
Piston 1 Clearance Vol. [cc]/Comp. Ratio	56/9.24:1
Piston 2 Clearance Vol. [cc]/Comp. Ratio	47/10.87:1
Piston 3 Clearance Vol. [cc]/Comp. Ratio	40/12.57:1
IVO - 0.1 mm (BTDC)	10
IVC - 0.1 mm (ABDC)	50
EVO - 0.1 mm (BBDC)	40
EVC - 0.1 mm (ATDC)	20

Compression ratio change was accomplished using three different piston designs. These pistons were custom forged and are shown photographically in Figure 3-1. The low compression

ratio piston is very similar to the stock Volvo piston coming with the head. The two higher compression ratio pistons have piston crown protrusions to decrease combustion chamber clearance volume. Figure 3-2 then shows the pent-roof, centrally located spark Volvo head and a cross section of the highest compression ratio piston in the combustion chamber at TDC.

Figure 3-1 Low, medium, and high compression ratio pistons, left to right.

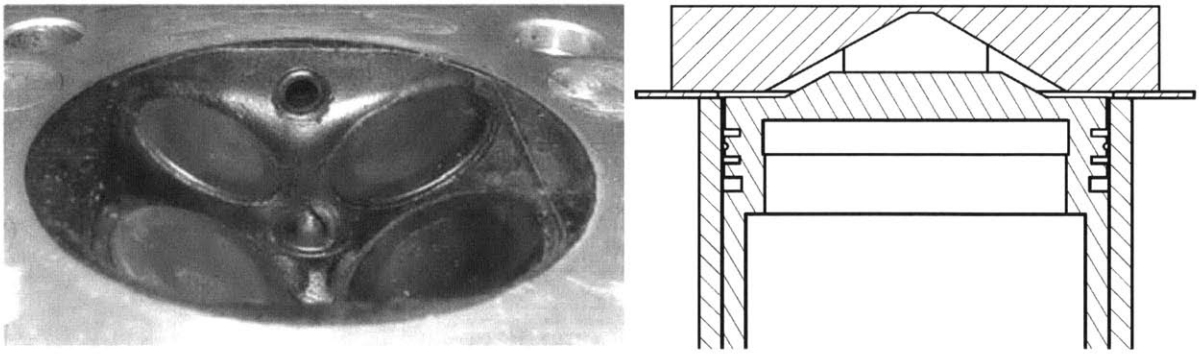

Figure 3-2 Picture of pent-roof, central spark Volvo head and cross section of highest compression ratio piston in combustion chamber at TDC.

An Eaton Dynamatic AF-6360 50 hp dynamometer is connected to the engine by a drive shaft, and controlled by an Eaton Dynamatic Adjustable Frequency Drive. The dynamometer is able to motor the engine and absorb extra power supplied by the engine while firing. It automatically adjusts torque to maintain constant engine speed at a manual set-point.

3.1.2 Air Inductance System

The intake air system is shown in Figure 3-3 and can be switched between ambient and boosted operation. In this study the boosted side of the intake system was used to calibrate the laminar flow element before every day of testing. The ambient side was then used for all engine tests. Air flows through a filter to limit dust and other small debris. A damping tank is used to reduce flow pulsations and mostly eliminate intake tuning. A throttle plate controls air mass flow into the engine.

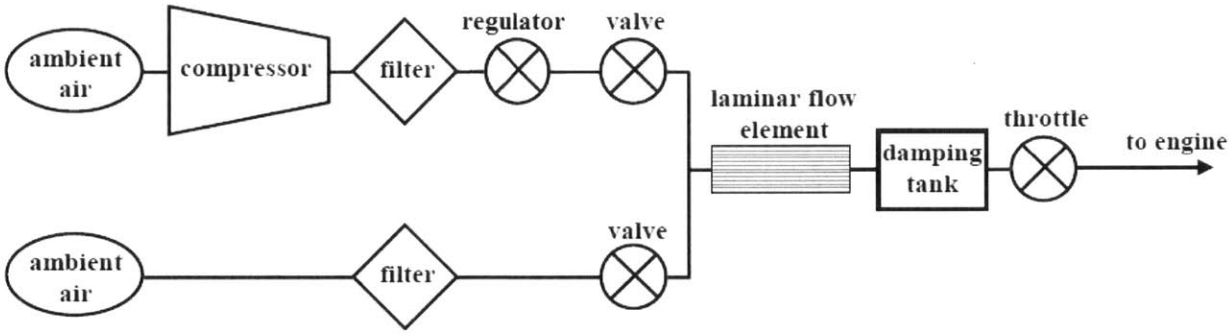

Figure 3-3 Intake air system schematic.

Previous experiments looked at tumble and swirl in this engine by adding different turbulence plates immediately before the intake port [41]. These turbulence plates are shown in Figure 3-4. It was found that the 2/3 asymmetric plate caused the most beneficial charge motion for combustion, so it was left in for these experiments.

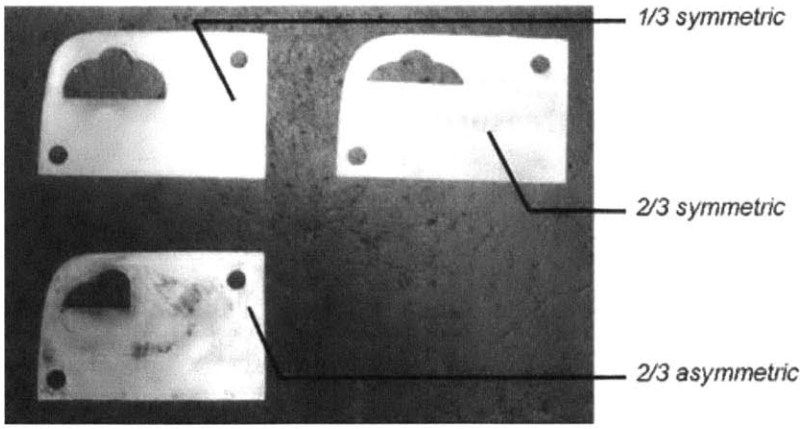

Figure 3-4 Various charge motion plates used in previous experiments [41].

3.1.3 Fuel System

The fuel system is shown in Figure 3-5. Fuel is drawn from a tank with a pump and passed through a filter on its way to the engine. At the engine, a differential backpressure regulator tied to MAP attempts to keep the pressure drop across the injector constant by varying fuel return flow. Fuel bypassing the injector is returned to the fuel tank through a heat exchanger to keep fuel temperature close to ambient conditions. Various slop tanks and a nitrogen tank allow for easy purging of the fuel system after use.

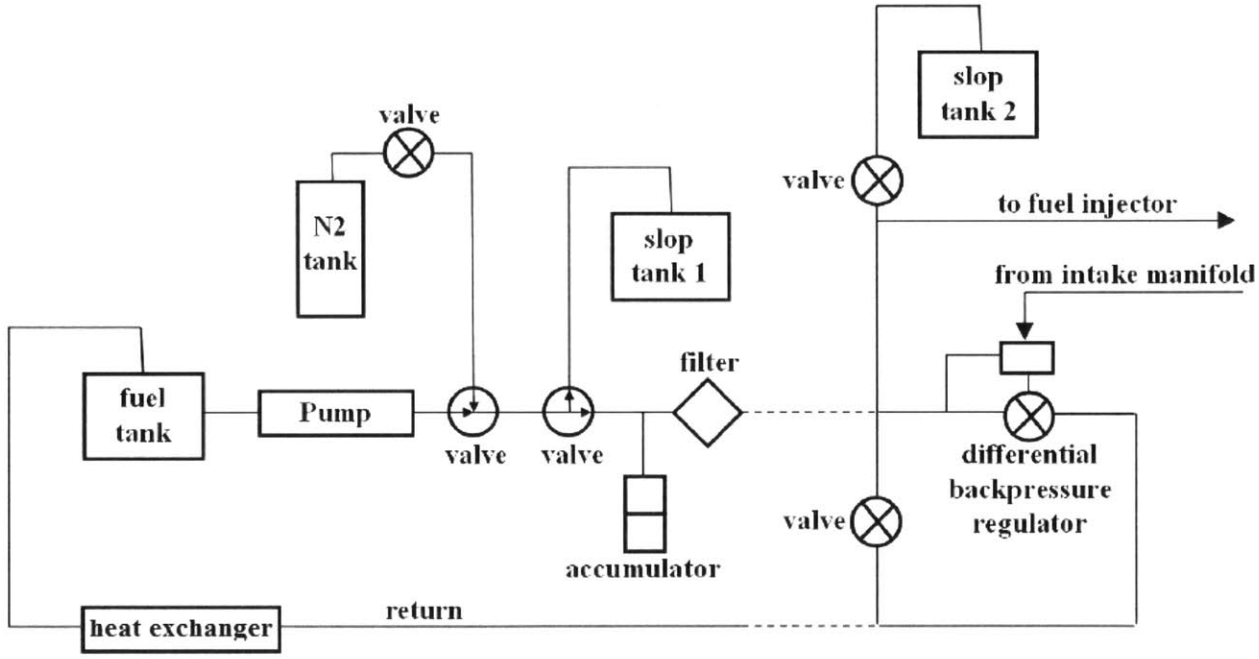

Figure 3-5 Fuel system schematic.

3.2 Engine Control and Measurement

3.2.1 Engine Control Unit

A MoTeC M4 engine controller is used to control the injector and ignition system. The injection timing is set to 385° BTDC and the dwell is set to 6 ms. The injector pulse width and spark timing can be adjusted while the engine is running.

3.2.2 Data Acquisition System

Voltage signals are fed from their respective sources into a BNC 2090 board via BNC cables. A National Instruments PCI-6023E data acquisition card reads these voltage signals at two different rates. Low speed data collection at 20 kHz is used for crank angle resolved data, and 100 kHz data collection is used for fuel injector pulse width measurements. Triggering and clock rate are set by a BEI H25 incremental encoder coupled to the crank shaft. LabView 8.5 is used to analyze engine variables in real time and to record raw voltages for future in-depth analysis.

3.2.3 Manifold Absolute Pressure Measurement and Control

An Omega PX176 absolute pressure transducer is located between the throttle and engine to measure MAP. A digital readout displays the MAP value and the raw voltage from the sensor is fed into the DAQ system for future analysis. MAP is manually varied using a stepper motor to open and close a throttle valve.

3.2.4 In-Cylinder Pressure Measurement

A Kistler 6125A piezoelectric pressure transducer equipped with a flame arrestor measures cylinder pressure. The transducer is mounted such that its face is flush to the combustion chamber wall. The mounting hole for the transducer is visible in the picture of the engine head in Figure 3-2. The signal from the transducer is fed into a charge amplifier where it is converted to a signal voltage. The pressure transducer was calibrated multiple times with a dead weight calibrator to ensure continued accuracy.

Encoder phasing, which is the rotational alignment of encoder pulses with crankshaft position, and absolute pressure pegging are critical to accurate cylinder pressure measurement and analysis [42]. Absolute pressure pegging is accomplished using the MAP reading near BDC, corrected for sensor response time. Encoder phasing is determined to within +/- 0.05 crank angle degrees using an AVL capacitive TDC sensor. Results of encoder phasing experiments are shown in Figure 3-6, where approach and retreat of the piston from TDC coincide during both TDC compression and TDC gas exchange with the correct encoder offset.

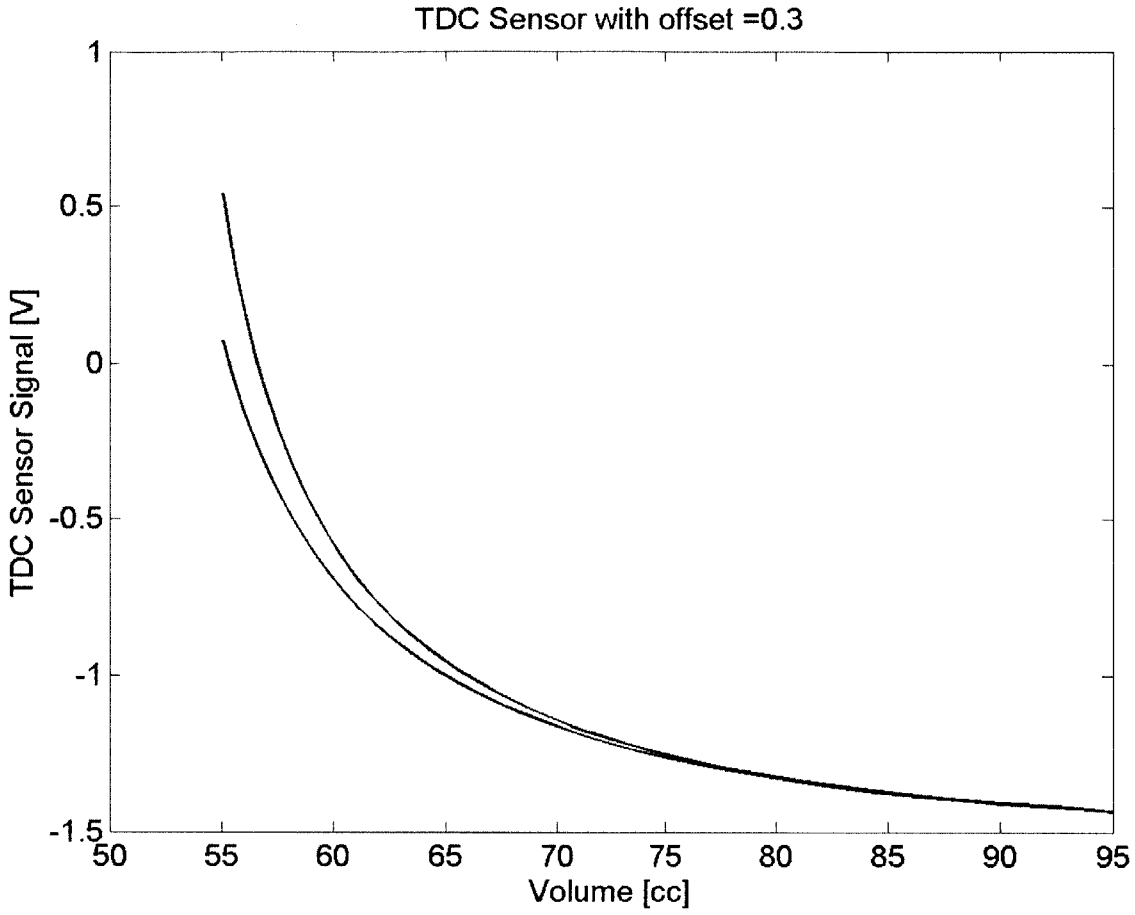

Figure 3-6 Results of encoder phasing experiments using AVL capacitive TDC sensor with correct offset applied.

3.2.5 Fuel Flow Measurement

The engine setup is port fuel injected with the fuel injector aimed at the intake valves. Fuel injected per cycle is measured using an experimental calibration based on fuel injector pulse width. This approach relies on the equation of liquid flow through an orifice explained in Appendix B:. Essentially, taking out the pressure drop across the injector and density of the gasoline, it can be found that fuel mass flow is linear with pulse width. The linear equation was found through multiple careful calibrations. To get actual fuel mass flow the injector pulse width is input into the experimental calibration equation and later corrected for injector pressure drop and fuel density. Injector pressure drop is measured using fuel pressure and MAP values during injection, corrected for sensor response times. Fuel density is calculated based on ambient and

intake temperatures. Fuel pressure is measured by an Omega PX181-200GV differential pressure transducer, and fuel temperature is measured using an Omega K-type thermocouple. The injector pulse width and fuel pressure voltages are recorded directly by the DAQ system, while relavent temperatures are recorded by hand. Accurate fuel flow measurements are vital to this study as expected changes in indicated efficiency are small.

3.2.6 Air Flow Measurement

Volumetric air flow is obtained by measuring differential pressure with a Druck LP 1000 Series differential pressure sensor across a laminar flow element. This volumetric flow rate is converted to a mass flow rate using the ideal gas law with damping tank pressure and temperature. Damping tank pressure is measured with an Omega PX176 absolute pressure transducer, and damping tank temperature is measured with an Omega K-type thermocouple. The air mass flow rate is corrected for water content using a humidity measurement.

Air flow calibration was completed before every day of testing by flowing air across an O'Keefe critical flow orifice in series before the air flow measurement system. This approach relies on the equation of gaseous flow through an orifice explained in Appendix B:. Pressure upstream of the critical orifice was varied, while differential pressure drop across the laminar flow element was recorded (pressure drop between orifice exit and laminar flow meter exit to ambient conditions was neglected). The calibration corrects for density effects and a digital display is set to read volumetric flow rate referenced to standard conditions. The digital display value is hand recorded.

3.2.7 Air-Fuel Ratio Measurement

A Universal Exhaust Gas Oxygen (UEGO) sensor measures the oxygen content of exhaust gas. A Horiba Mexa-110λ analyzer reads this signal and displays relative air-fuel ratio (λ).

3.2.8 Hydrocarbon Emissions Measurement

A Cambustion HFR400 fast-response flame ionization detector (FID) is used to measure hydrocarbon emissions. The fast-response FID consists of a main control unit (MCU) and two remote sampling heads. Sample gas is drawn from the exhaust system through a heated sampling

tube and into the center of a hydrogen flame within each sampling head. The oxidation of hydrocarbons in the flame produces ions collected with a high voltage metal collector above the flame. The rate of ionization, and thus current across the collector, is proportional to hydrocarbon concentration in the sample, allowing the hydrocarbon concentration to be quantified with a simple linear calibration. The FID is calibrated multiple times each testing day using two calibration gases of known hydrocarbon concentration and test cell air as a zero.

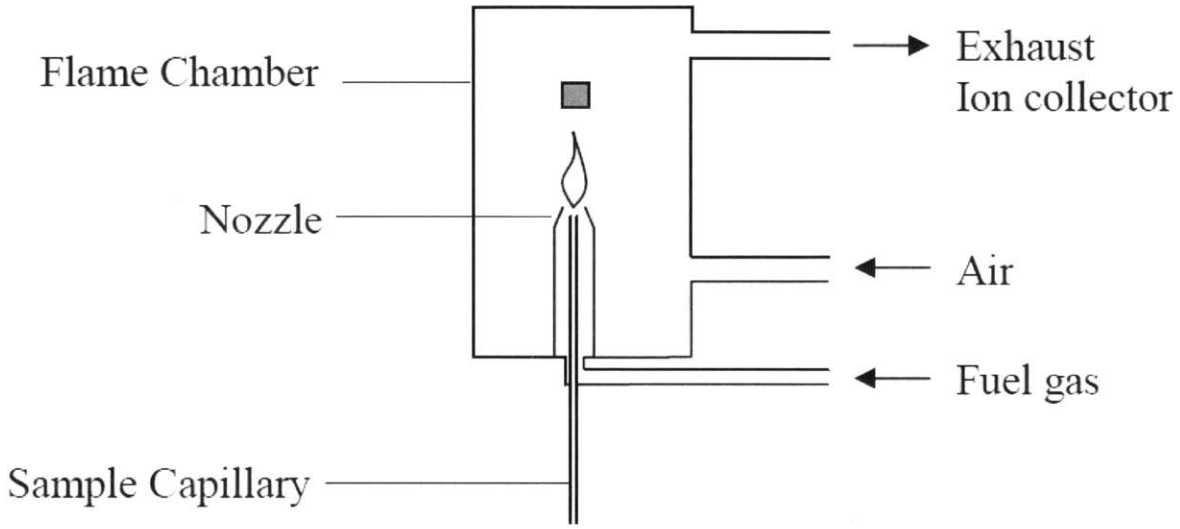

Figure 3-7 Schematic of fast-response FID sampling head from Cambustion used in hydrocarbon emissions measurement [43].

3.2.9 CO and CO_2 Emissions Measurement

A Horiba MEXA-554 NDIR is used to measure CO and CO_2 emissions. Hot exhaust sample is drawn through copper tubing submerged in an ice-water condenser, enters a Buchner vacuum flask, and is drawn through a carbonate desiccant before entering the NDIR. This process ensures the sample is completely dry to allow for accurate CO and CO_2 measurements with this device. Water content is calculated analytically to find wet exhaust concentrations.

3.2.10 Temperature Measurement and Control

Various temperatures are measured throughout the engine setup using Omega K-type thermocouples at the following locations:

- Engine coolant inlet
- Engine oil inlet
- Intake, about 4 cm from intake port inlet
- Exhaust, about 3 cm from exhaust port outlet
- Damping Tank

Engine coolant and oil temperatures are controlled to about +/- 1°C by overcooling with a cold-water heat exchanger, and then heating to desired temperature with an electric heater. The electric heater is controlled via an electronic thermostat to reach a given set point.

3.3 Total Engine Crevices

For this engine setup all crevice volumes present have been measured and are displayed in Table 3-2. These crevices are shown in Figure 3-8 and consist of the spark plug crevice, valve seat crevice, head gasket crevice, and piston crevice. To calculate component crevice volumes a characteristic quench distance of 0.4 mm is used as the crevice beginning. The piston crevice is by far the largest crevice volume, accounting for approximately 83% of the total crevice volume. This confirms the decision to make the piston crevice volume the focus of this experimental study. It is important to note that there is an additional spark plug installed across from the pressure transducer from prior experiments. This doubles the spark plug crevice in relation to a normal engine, but has little effect on the total crevice volume. The valve seat and head gasket crevices are found to be insignificant to the total crevice volume. The total engine crevice volume as a fraction of clearance volume ranges from 2.7% to 3.7% and increases with higher compression ratio.

Table 3-2 Total engine crevices for all three compression ratios tested, measured at room temperature.

	CR = 9.24		CR = 10.87		CR = 12.57	
	Volume [mm^3]	Percent	Volume [mm^3]	Percent	Volume [mm^3]	Percent
Spark Plug Crevice	187	12.0	187	12.0	187	12.5
Valve Seat Crevice	32	2.0	32	2.0	32	2.1
Head Gasket Crevice	37	2.4	37	2.4	37	2.5
Piston Crevice	1294	83.5	1296	83.5	1238	82.9
Total Crevice Volume	1550	100.0	1552	100.0	1494	100.0
Clearance Volume [mm^3]	56450		47150		40220	
Total Crev / Clearance [%]	2.7		3.3		3.7	

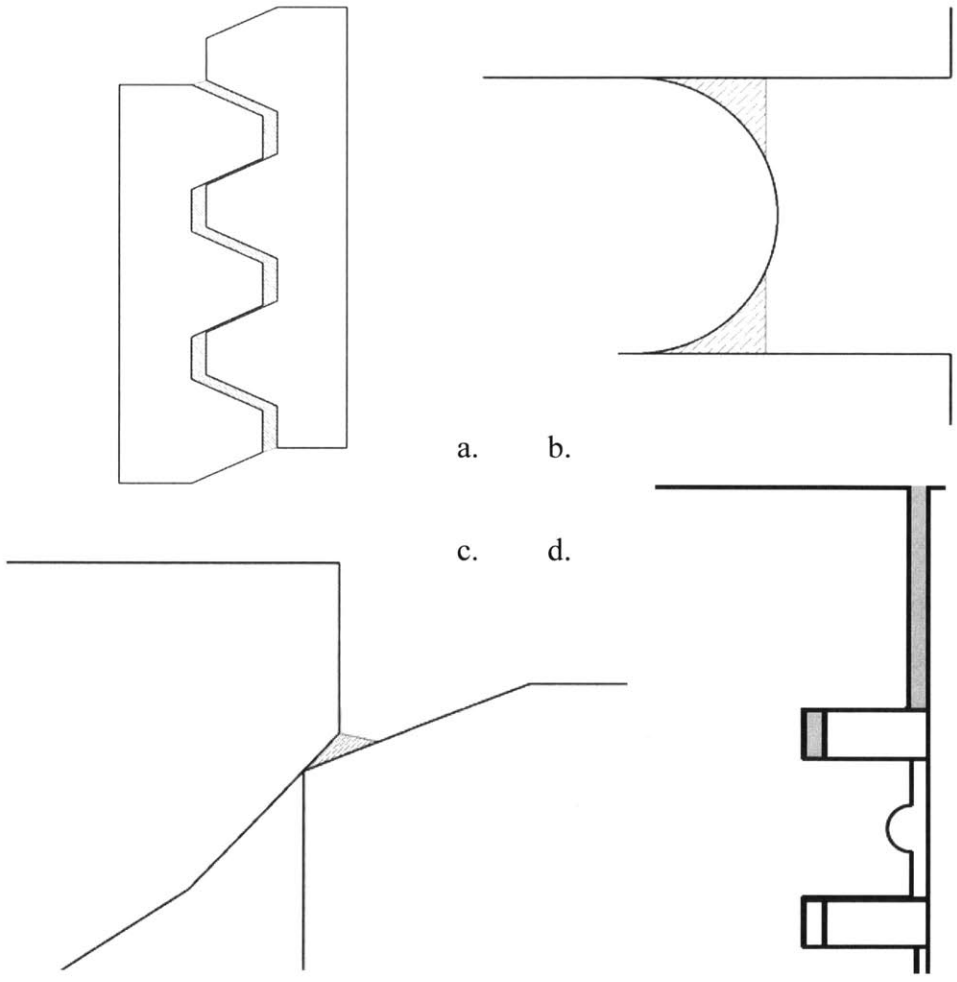

Figure 3-8 Drawings of (a) spark plug thread crevice, (b) head gasket crevice, (c) valve seat crevice, and (d) piston crevice.

3.4 Piston Crevice Measurements and Modifications

The piston crevice has been precisely measured for each of the three compression ratio pistons used in this study. A to-scale drawing of the lowest compression ratio piston crevice is shown in Figure 3-9 and detailed piston crevice volume sizes are shown in Table 3-3. Crevice volumes are calculated at room temperature (cold) and at the maximum engine temperatures expected in this study (hot). The piston crevice dimensions and volumes are very similar between the different compression ratio pistons. Inter-ring crevice volume is reported, but the main focus of this study is the piston crevice volume containing the top land volume, top ring side clearance volume, and top ring back clearance volume. Piston crevice volume as a fraction of clearance volume ranges from 1.8% to 3.1% with increased values at higher compression ratios and decreased values at higher temperature.

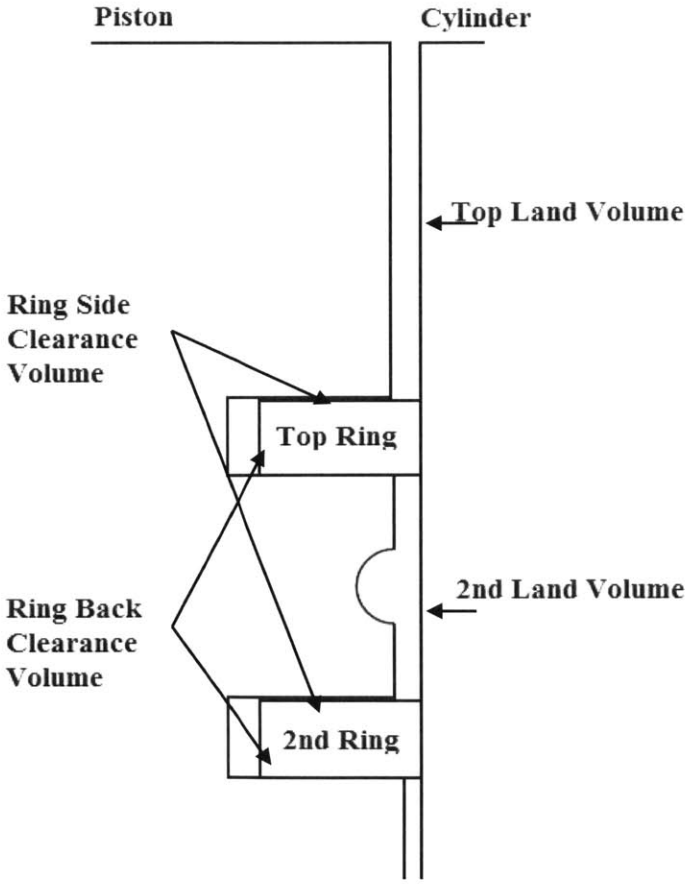

Figure 3-9 To-scale drawing of piston-ring pack crevices for low compression ratio piston showing locations of crevice volumes listed in Table 3-3.

Table 3-3 Summary of piston-ring pack crevice volumes for all three compression ratio pistons tested; cold refers to room temperature measurements; hot refers to measurements under maximum load conditions expected for this set of experiments.

	CR = 9.24		CR = 10.87		CR = 12.57	
	Cold	Hot	Cold	Hot	Cold	Hot
Top Land Volume [mm^3]	1018	781	1033	794	973	735
Top Ring Side Clearance Volume [mm^3]	46	45	37	36	37	36
Top Ring Back Clearance Volume [mm^3]	229	191	226	187	228	189
Total Piston Crevice Volume [mm^3]	1294	1017	1296	1018	1238	961
2nd Land Volume [$mm^{3]}$]	768	639	775	646	740	610
2nd Ring Side Clearance Volume [mm^3]	36	36	32	32	40	41
2nd Back Clearance Volume [$mm^{3]}$]	161	127	159	125	159	125
Total Inter-Ring Crevice Volume [$mm^{3]}$]	965	802	966	804	939	777
Clearance Volume [mm^3]	56450		47150		40220	
Piston Crevice / Clearance [%]	2.3	1.8	2.7	2.2	3.1	2.4

Three modifications are made to each compression ratio piston to vary piston crevice volume. These modifications are drawn out in Figure 3-10 and summarized in Table 3-4. Two of the changes increase piston crevice volume by adding grooves to the top land and one decreases piston crevice volume by moving up the top ring. Modifications were planned so as to minimize machining time, while allowing for one piston to be used at all piston crevice volumes for a given compression ratio. The first groove is half of the radial width of the control piston top ring groove, and is located 3 mm below the piston crown. The second groove extends the first groove radially inward matching the dimensions as the top ring groove. The new top land configuration moves the top ring up to the groove 2 cutout, moves the second ring up to the original top ring groove, and leaves the original second ring groove empty.

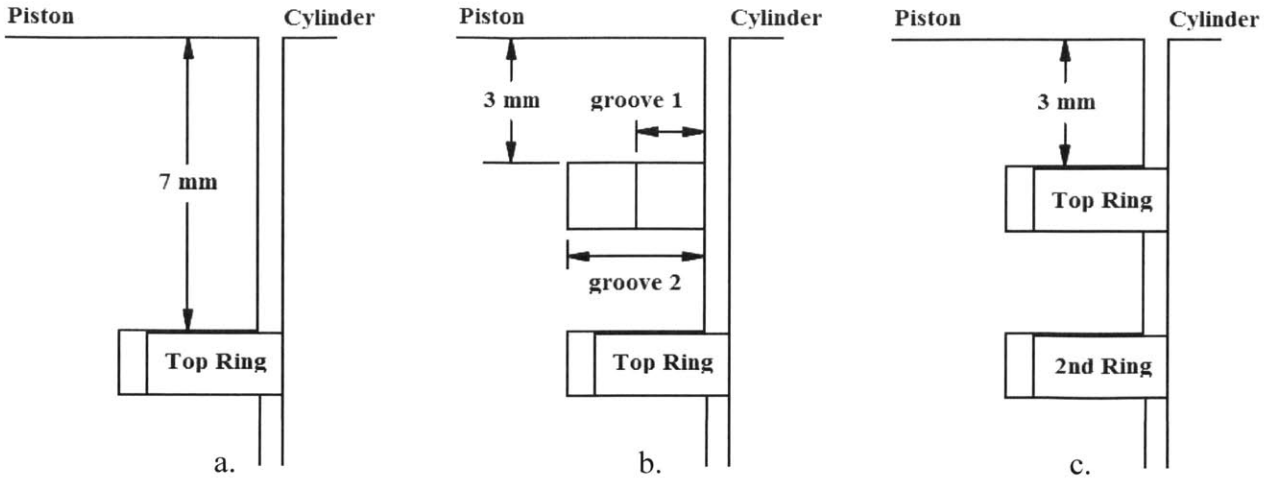

Figure 3-10 Piston crevice modifications; (a) control piston, (b) increased crevice volume, (c) decreased crevice volume.

Table 3-4 Piston crevice modification dimensions and percent change in total piston crevice volume for each compression ratio piston.

			CR = 9.24	CR = 10.87	CR = 12.57
Modification	**Groove Thickness [mm]**	**Top Land Height [mm]**	**Piston Crevice Volume Increase [%]**	**Piston Crevice Volume Increase [%]**	**Piston Crevice Volume Increase [%]**
Control (0)	0	7	0	0	0
Groove 1 (1)	1.608	7	48.5	48.5	50.8
Groove 2 (2)	3.216	7	95.1	95.0	99.5
New Top (3)	N/A	2.997	-44.8	-45.6	-44.8

3.5 Experiments

3.5.1 Procedure

At the beginning of each test day oil and coolant temperatures are warmed up to desired values, the laminar air flow meter is calibrated, the NDIR is calibrated, and FID is warmed up and calibrated. The procedure for each spark sweep is as follows:

1. Set engine speed with dynamometer controller.
2. Run engine until it is fully warmed up and at steady state.
3. Adjust fuel and air flow to get desired air-fuel ratio and MAP.
4. Make initial estimate of MBT timing from real-time NIMEP calculation.
5. Run spark sweep at +/- 7° from estimated MBT timing, recording data at each spark timing.
6. Pick MBT point based on NIMEP and COV values over the spark sweep.

3.5.2 Fuel

The fuel used in these experiments is a high octane Tier II EEE emission certification fuel from Haltermann Solutions. This fuel allows for experiments to extend to high compression ratios where knock could limit a lower octane fuel. It also means fuel properties are nearly constant across different tests because of the strict quality controls required of a federal emission certification fuel.

3.5.3 Test Matrix

The test matrix for the efficiency experiments is shown in Table 3-5. At every speed and MAP combination for each compression ratio a spark sweep was run. The highest loads at the two higher compression ratios are knock limited, so they were not included in the experiments. This test matrix was completed for 50°C and 80°C coolant temperatures. A total of 60 spark sweeps were taken for these experiments. MBT timing is used in all data results and analysis.

Table 3-5 Test matrix for efficiency experiments.

	1500, 2000, 2500 RPM			
CR \ MAP [bar]	**0.4**	**0.6**	**0.8**	**WOT**
9.24	X	X	X	X
10.87	X	X	X	
12.57	X	X	0.75	

This page intentionally left blank

4 Analysis Tools

Engine-out experimental data is post-processed using various Matlab scripts to look at combustion characteristics, efficiency values, and emissions data.

4.1 One Zone Heat Release

A one zone heat release analysis has been created based on methods previously developed at the MIT Sloan Automotive Lab [26,44]. This technique applies the first law of thermodynamics with the combustion chamber as the control volume. The application of the first law on this system is represented pictorially in Figure 4-1.

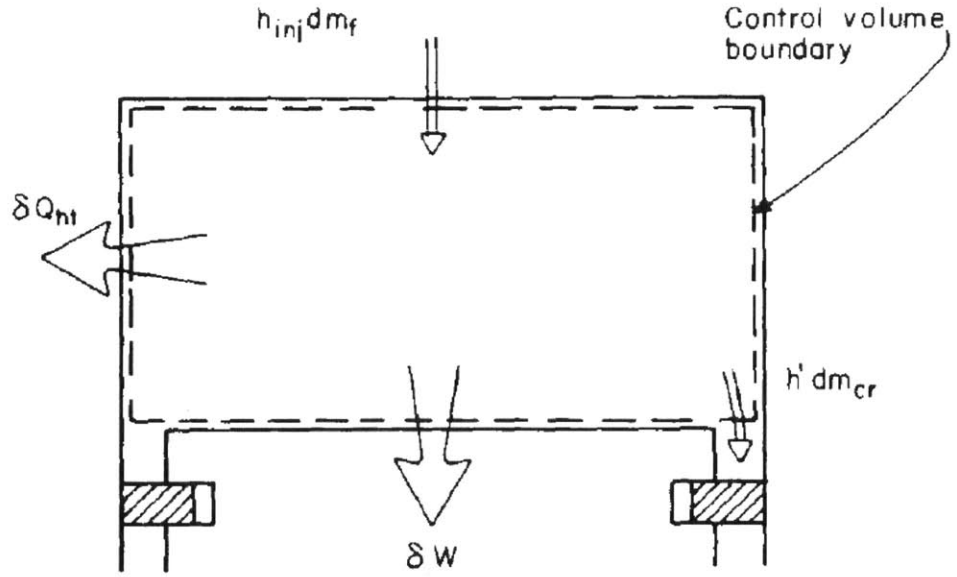

Figure 4-1 Schematic of thermodynamic system and sign convention [26].

Using the sign convention shown in Figure 4-1 the first law on the combustion chamber system solved for the chemical heat release is written in Equation 4.1:

$$\delta Q_{ch} = dU_s + \delta W + \sum h_i dm_i + \delta Q_{ht} \qquad [4.1]$$

where δQ_{ch} is the chemical energy release by combustion, dU_s is the change in sensible energy from reactants to products, δW is the work done by the piston, $h_i dm_i$ is the enthalpy flow across the boundary, and δQ_{ht} is the heat transfer across the system boundary. These terms are converted to expressions containing known quantities such as cylinder pressure and volume using thermodynamic and mathematical approaches. Details of this process are presented by Cheung [44]. The result is a convenient form of the one zone heat release expression in terms of crank angle (θ) shown in Equation 4.2:

$$\frac{dQ_{ch}}{d\theta} = \frac{\gamma}{\gamma - 1} p \frac{dV}{d\theta} + \frac{1}{\gamma - 1} V \frac{dp}{d\theta} + \frac{dQ_{ht}}{d\theta} + V_{cr}\left[\frac{T'}{T_{crev}} + \frac{T}{T_{crev}(\gamma - 1)} - \frac{1}{bT_{crev}} \ln\left(\frac{\gamma - 1}{\gamma' - 1}\right)\right]\frac{dp}{d\theta} \quad [4.2]$$

Where γ is the ratio of specific heats, p is in-cylinder pressure, V is volume, V_{cr} is crevice volume, T is in-cylinder temperature, T_{crev} is crevice gas temperature, $T'$and γ' are in-cylinder gas temperature and in-cylinder gas ratio of specific heats when flow is entering the crevice and are crevice gas temperature and crevice gas ratio of specific heats when flow is exiting the crevice, b is the linear constant at crevice conditions from Equation 4.3, and θ is crank angle. Equation 4.2 requires specific heat ratios for various conditions, a heat transfer calculation, and an accurate crevice specification. In the crevice term the two variables with apostrophes change based on whether flow is into or out of the crevice. This will be further explained in Section 4.1.4.

4.1.1 Ratio of Specific Heats

Ratios of specific heats for various temperatures and engine processes were taken from Cheung [44]. These ratios are approximately linear with temperature and are of the form shown in Equation 4.3:

$$\gamma(T) = a + bT \quad [4.3]$$

where a and b are constants. During compression and expansion a and b are nonzero real values and during combustion the ratio of specific heats is approximated as a constant value with b set to zero. The b in Equation 4.3 corresponds to the b in Equation 4.2 for the crevice gas. Data taken from Cheung is based on Indolene at stoichiometric conditions with interpolation to account for the residual mass fraction.

4.1.2 Residual Mass Fraction

A residual mass fraction model was created based on similar previous models and residual analyses [23,45]. Residual gas trapped in the cylinder is the result of two causes: nonzero volume in the combustion chamber at IVO and exhaust backflow during valve overlap. The definition of residual fraction and its components are presented in Equation 4.4:

$$x_r = \frac{m_r}{m} = x_{r,IVO} + x_{r,backflow} \qquad [4.4]$$

where x_r is the residual mass fraction, m_r is residual mass, m is total charge mass, $x_{r,IVO}$ is the residual mass fraction due to trapped mass at IVO, and $x_{r,backflow}$ is residual mass due to exhaust backflow. Mass trapped in the combustion chamber at IVO can be calculated by assuming the in-cylinder mass in the exhaust process undergoes an isentropic expansion [23]. This analysis yields Equation 4.5. The trapped mass at IVO is sensitive to equivalence ratio, but since all conditions tested are at stoichiometric this sensitivity is neglected.

$$x_{r,IVO} = \frac{1}{r_c} * \frac{(p_e/p_i)^{1/\gamma}}{\left[1 + \frac{Q^*}{c_v T_i r_c^{\gamma-1}}\right]^{1/\gamma}} \qquad [4.5]$$

$$Q^* = \frac{m_f Q_{LHV}}{m} \qquad [4.6]$$

Here, r_c is compression ratio, p_e is exhaust pressure, p_i is intake pressure, γ is the ratio of specific heats at exhaust conditions, c_v is the specific heat at constant volume for intake conditions, T_i is intake temperature, m_f is fuel mass, Q_{LHV} is fuel lower heating value, and m is

total charge mass. During the valve overlap period, when both the intake and exhaust valves are open, exhaust can flow back into the cylinder if cylinder pressure is lower than exhaust pressure. This is modeled by looking at pressure driven flow across the exhaust valve; a detailed description of which is given in Appendix B:. Using the calculated exhaust mass backflow the residual fraction from backflow is calculated using Equation 4.7:

$$x_{r,backflow} = \int \frac{\dot{m}_{backflow}}{\rho_i V_d \left(\frac{r_c + 1}{r_c}\right)} \frac{1}{6 * RPM} d\theta \qquad [4.7]$$

Where $\dot{m}_{backflow}$ is the exhaust mass back flow rate, ρ_i is intake density, V_d is displacement volume, r_c is compression ratio, and RPM is engine speed in rpm.

4.1.3 Heat Transfer

Energy is lost from in-cylinder gases through the boundaries of the combustion chamber by heat transfer. In the thermodynamic environment of the combustion chamber convection is the dominant mode of heat transfer. This convective heat transfer rate is given in Equation 4.8:

$$\frac{dQ_{ht}}{dt} = Ah_c(T - T_{boundary}) \qquad [4.8]$$

where A is the combustion chamber surface area, h_c is the convective heat transfer coefficient, T is average in-cylinder temperature, and $T_{boundary}$ is wall temperature for the combustion chamber boundaries. The convective heat transfer coefficient is modeled on Woschni's correlation with a few additional considerations using Equation 4.9:

$$h_c = 3.26 c_1 B^{m-1} p^m T^{0.75-1.62m} w^m \qquad [4.9]$$

where c_1 is a calibration constant, B is cylinder bore, p is in-cylinder pressure, T is in-cylinder temperature, m is set to 0.8, and w is the characteristic velocity contributed by piston movement, charge motion, and combustion defined in Equation 4.10:

$$w = 2.28 * \bar{S}_p + 0.308 * (U_{tumble} + U_{swirl}) + .00324 c_2 \frac{V_d T_{IVC}}{p_{IVC} V_{IVC}} (p - p_m) \quad [4.10]$$

Where $\bar{S}_p$ is mean piston speed, U_{tumble} is tumble velocity, U_{swirl} is swirl velocity, c_2 is a calibration constant, V_d is displacement volume, T_{IVC} is in-cylinder temperature at IVC, p_{IVC} is in-cylinder pressure at IVC, V_{IVC} is cylinder volume at IVC, p is in-cylinder pressure, and p_m is motored in-cylinder pressure. The first term to the right of the equals sign represents charge motion induced by the piston, the second term represents charge motion from engine tumble and swirl, and the third term represents charge motion induced by combustion. The charge motion term from combustion looks at the difference between actual and motored pressure referenced to IVC. Motored pressure is calculated based on an isentropic cycle given the initial mass, pressure, and temperature. The constant c_2 is used to calibrate the extent to which combustion affects the charge motion. Engine tumble and swirl have been thoroughly investigated on a steady flow rig for this engine setup generating flow coefficients used in this heat transfer analysis [41]. These flow coefficients are combined with engine variables in Equation 4.11 to find tumble and swirl ratios:

$$R_{tumble/swirl} = \pi \eta_v B L \left[\int_{\theta 1}^{\theta 2} (A_v C_D) C_{tumble/swirl} d\theta \right] \Big/ \left[\int_{\theta 1}^{\theta 2} (A_v C_D) d\theta \right]^2 \quad [4.11]$$

Where $R_{tumble/swirl}$ are tumble or swirl ratios, η_v is volumetric efficiency referenced to intake manifold conditions, B is bore, L is stroke, A_v is valve curtain area, C_D is valve discharge coefficient, and $C_{tumble/swirl}$ are the tumble or swirl coefficients. The integrals in Equation 4.11 are calculated while the intake valves are open. These tumble and swirl ratios are then input into Equation 4.12 to find tumble and swirl velocities:

$$U_{tumble/swirl} = \pi N B R_{tumble/swirl} \quad [4.12]$$

where $U_{tumble/swirl}$ are tumble or swirl velocities, N is engine speed in rev/s, B is bore, and $R_{tumble/swirl}$ are tumble or swirl ratios. Tumble and swirl velocities are then input back into Equation 4.10 to assess the heat transfer impact of added charge motion from engine tumble and swirl. This heat transfer model is based on Woschni's correlation with the effects of tumble and swirl added for this specific engine setup. Two calibration constants, c_1 and c_2, are added to the model to allow for adjustment of the heat transfer impact.

4.1.4 Crevice Model

In this model the piston crevice is the only crevice included and crevice volume is calculated based on thermal expansion considerations. The fourth term to the right of the equals sign in Equation 4.2 represents the crevice volume impact on heat release. When cylinder pressure is rising, mass is flowing into the crevice and therefore the terms with apostrophes are evaluated at in-cylinder conditions. When cylinder pressure is falling, mass is flowing out of the crevice and therefore the terms with apostrophes are evaluated at crevice conditions. This crevice model essentially finds the enthalpy change due to flow into and then out of the piston crevice. Crevice temperature is calculated as an average of piston top land temperature and upper liner temperature. Blowby is neglected in this model.

4.2 Crevice Hydrocarbon Emission Model

A basic hydrocarbon emission model is used to check provide bounds on expected hydrocarbon emissions while checking validity of FFID measurements. This model is based on a broad study of hydrocarbon emissions mechanisms performed at the Sloan Automotive Laboratory [32], which is summarized in the flowchart in Figure 4-2. Three scenarios are investigated for each operating point: all fuel trapped in piston crevice is exhausted as HC emission, all fuel trapped in piston crevice is oxidized, all fuel trapped in piston crevice is oxidized according to the flowchart. The three cases only differ in treatment of the HC emissions from the piston crevice and leave all other sources as values seen in Figure 4-2.

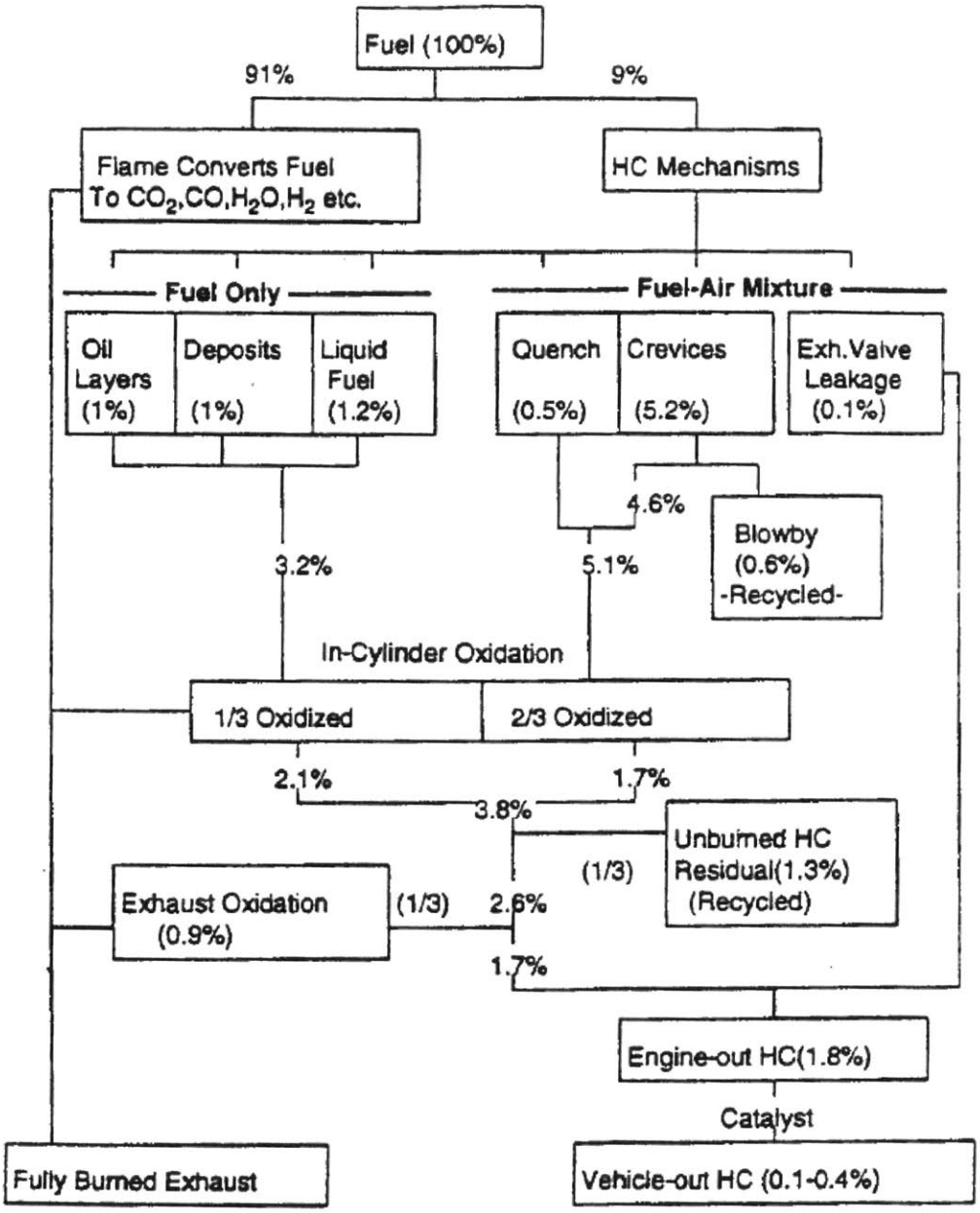

Figure 4-2 Complete flow chart for the gasoline fuel, which enters each cylinder, through both the normal combustion process (left side) and the unburned hydrocarbon mechanisms (right side). Numbers in parenthesis denote an HC emission index (% of gasoline entering the cylinder each cycle) for each step in the total process [32].

4.3 Piston-Ring Pack Model

A dynamic piston-ring pack model has been developed at the Sloan Automotive Lab to study friction, oil consumption, wear, and blowby [46–49]. In quantifying these areas this model specifically examines ring-liner lubrication, gas flows, ring dynamics, and the influence of piston and ring design parameters. In this study the gas flow calculation given different piston design parameters and in-cylinder conditions is of particular interest.

The model requires in-cylinder pressure, detailed piston and ring dimensions, and liner and piston finite element analyses at warmed up temperatures. The latter requirement has been approximated with similar piston and cylinder sizes as this data was not readily available for the custom pistons tested.

Outputs of the dynamic piston-ring pack model include: pressures of different cavities, mass flow rate between different cavities, axial forces, moments on the top two rings, axial relative location of the top two rings, and hydrocarbon emission index from piston crevice. Blowby values and hydrocarbon emission indices have been extracted from the output files for a number of different cases. The different experimental conditions simulated are summarized in Table 4-1. In the table the first row indicates the baseline case and bolded experimental parameters in subsequent rows show deviations from the baseline.

Table 4-1 Experimental test points simulated using the dynamic piston-ring pack model.

Compression Ratio	Crevice Groove	Coolant Temp [°C]	Speed [RPM]	MAP [bar]
9.24	control	80	2000	0.6
10.87	control	80	2000	0.6
12.57	control	80	2000	0.6
9.24	**groove 2**	80	2000	0.6
9.24	**New Top**	80	2000	0.6
9.24	control	80	**1500**	0.6
9.24	control	80	**2500**	0.6
9.24	control	80	2000	**0.8**

5 Experimental Results and Analysis

5.1 Part Load Definition

To best analyze the experimental results two part load NIMEP values are chosen based on a constant indicated torque per cylinder of 13.36 Nm. The first of these is based on the displacement volume of the research engine, and is representative of current naturally aspirated engines at part load. The second is based on a turbo-downsized engine displacement of 300 cc per cylinder, which would signify an aggressive turbo-downsizing strategy. These part load points are summarized in Table 5-1.

Table 5-1 Part load NIMEP values for naturally aspirated and turbo-downsized displacement volumes.

	Naturally Aspirated	Turbo-Downsized
Indicated Torque per Cylinder [N*m]	13.36	13.36
Displacement Volume [cc]	465	300
NIMEP [bar]	3.6	5.6

5.2 Baseline Case

5.2.1 Case Definition

The baseline case in this investigation is summarized in Table 5-2. The low compression ratio piston is chosen since it is representative of the stock piston of the Volvo head. A mid-speed is chosen along with a warmed up coolant temperature to best approximate actual engine conditions. In the baseline, as in all data points discussed, the relative air-fuel ratio (λ) is set to 1 and MBT timing is used. This baseline will be the basis for which different trends with engine conditions and piston geometry will be researched.

Table 5-2 Baseline testing conditions.

Compression Ratio	9.24
Engine Speed [RPM]	2000
Coolant Temperature [°C]	80
Lambda [λ]	1
Spark Advance	MBT Timing

5.2.2 Mass Trapped in Piston Crevice

Mass trapped in the piston crevice plays a vital role in the crevice effect on engine efficiency. To calculate the approximate mass trapped in the crevice an approach identical to that used in the simulation study is applied to experimental data. Equation 5.1 is used to calculate this approximate trapped crevice mass:

$$m_{crev} = \frac{(p_{peak} - MAP)V_{crev}}{R_u T_{crev}} \qquad [5.1]$$

where m_{crev} is the mass trapped in the crevice, p_{peak} is peak pressure, MAP is manifold absolute pressure, V_{crev} is crevice volume, R_u is the unburned gas constant, and T_{crev} is crevice gas temperature. To find trapped crevice masses the values in [5.1] are measured and evaluated from experiments. At the baseline case (Table 5-2) four different MAP values are tested at each modified piston geometry; peak pressures are plotted versus NIMEP in Figure 5-1, crevice temperatures are plotted versus NIMEP in Figure 5-2, crevice volumes are plotted versus NIMEP in Figure 5-3, and trapped crevice masses are plotted versus NIMEP in Figure 5-4. Experimental data points are plotted as small markers, with a color-matched dashed line representing a modified cubic interpolation connecting them. The two part load NIMEP values (Table 5-1) are interpolated and plotted for each piston crevice modification.

Peak pressure increases linearly with increasing NIMEP for each of the piston crevice modifications tested. This is the expected trend as more mass is allowed into the cylinder at higher load resulting in higher initial, compression and combustion pressures. The peak pressure is independent of piston crevice modification at this baseline case. This is also expected because changing the crevice volume should have little effect on initial mass in the cylinder.

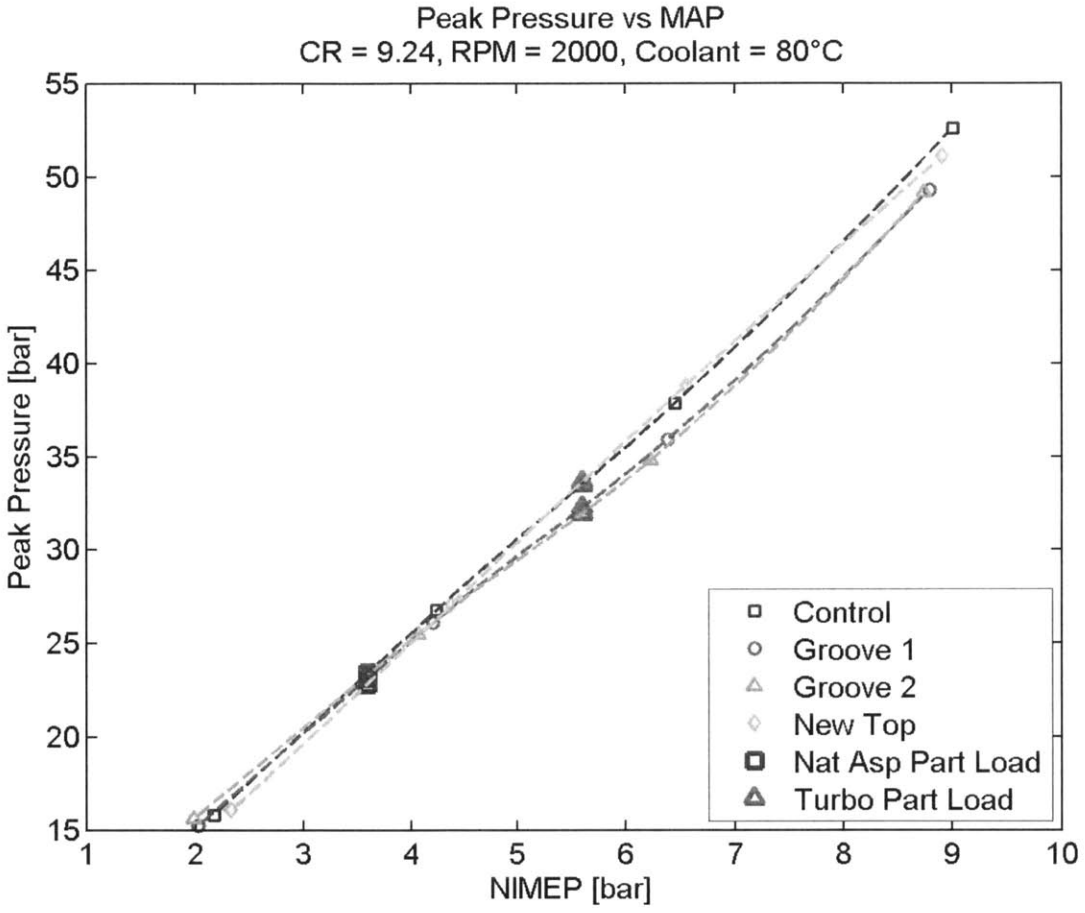

Figure 5-1 Peak pressure versus MAP for the baseline case with control piston crevice modification.

Crevice temperature increases linearly with increasing NIMEP for each of the piston crevice modifications tested. The linear increase is the result of user input approximate component temperatures, and thus the trend is that defined by previously reported experiments. The crevice temperature is very nearly independent of piston crevice modification at this baseline case. There is a slight decrease in crevice temperature at the lower crevice volumes, but this has almost no effect on the total trapped crevice mass.

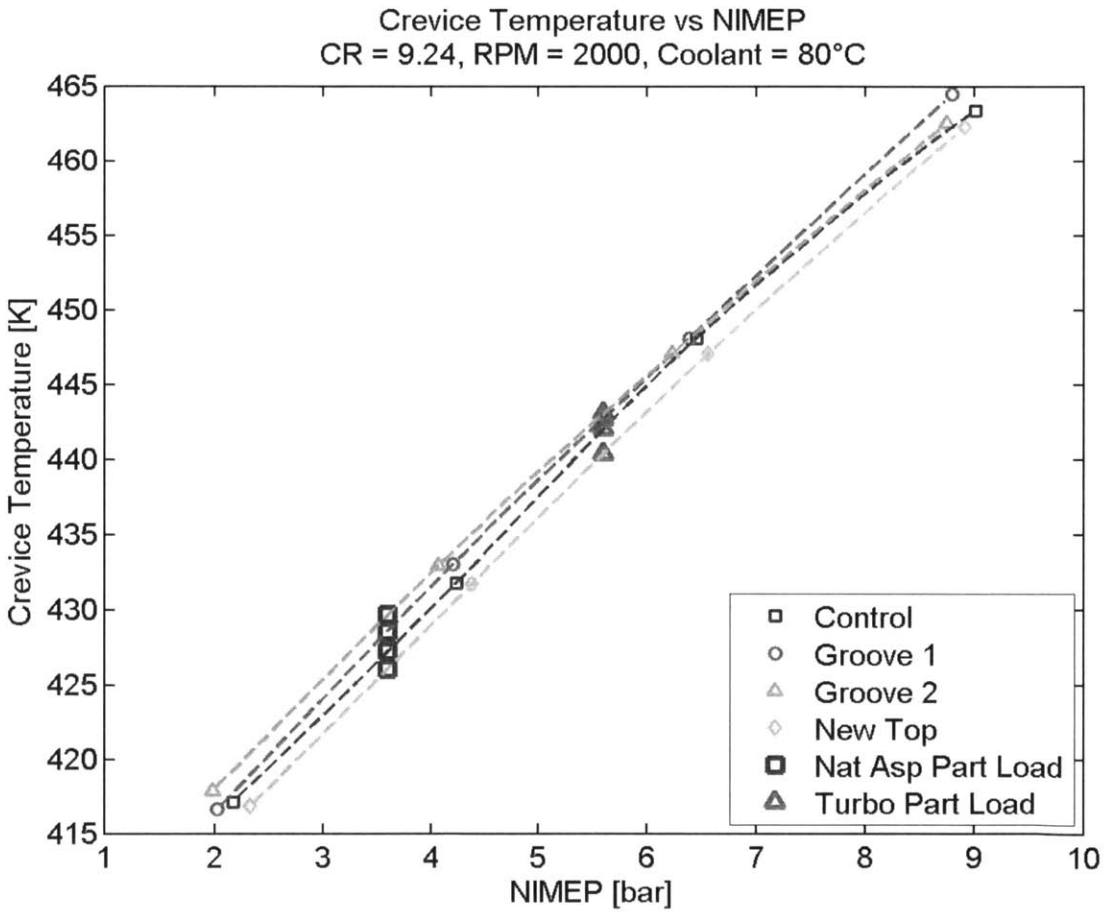

Figure 5-2 Crevice temperature versus NIMEP for the baseline case at various piston crevice modifications.

As NIMEP is increased crevice volume slightly decreases in a linear fashion. This is the result of thermal expansion considerations. Component temperatures increase with NIMEP, resulting in a shrinking crevice gap and ultimately a reduced crevice volume. Across piston crevice modifications crevice volume changes similarly to the planned changes at room temperature. Increases are slightly higher than found at room temperature for increased crevice volumes because thermal expansion does not affect the groove volume much.

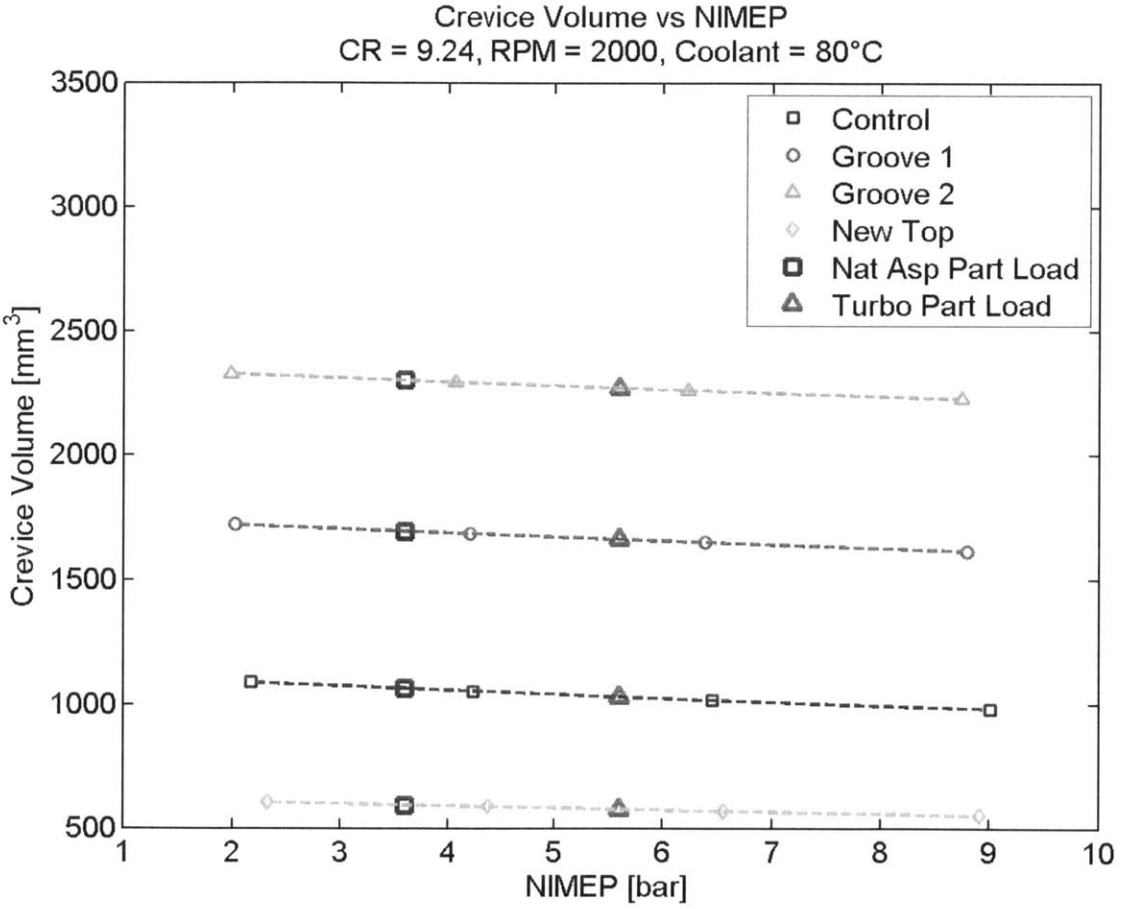

Figure 5-3 Crevice volume versus NIMEP for the baseline case at various piston crevice modifications.

Trapped crevice mass as a fraction of total charge mass decreases with increasing NIMEP. This happens at different rates depending on the piston crevice modification, and the lower the crevice volume the less dramatic the decrease. Interestingly, the higher crevice volumes, groove 1 and groove 2, seem to change slope as NIMEP is increased. This is due to non-linear changes in peak pressure with increasing NIMEP. Across piston crevice modifications, as expected, trapped crevice mass per total charge mass increases with higher crevice volume. It is interesting to note that these numbers are quite high, with the groove 2 piston crevice modification accounting for about 20% of the total mass at the peak pressure point. Even though these volumes are small compared to the combustion chamber volume, the low gas temperatures and high pressures lead to significant mass trapped in the crevice. As an aside, in a diesel engine this large mass of trapped crevice mass consists of air, leading the engine to burn much leaner.

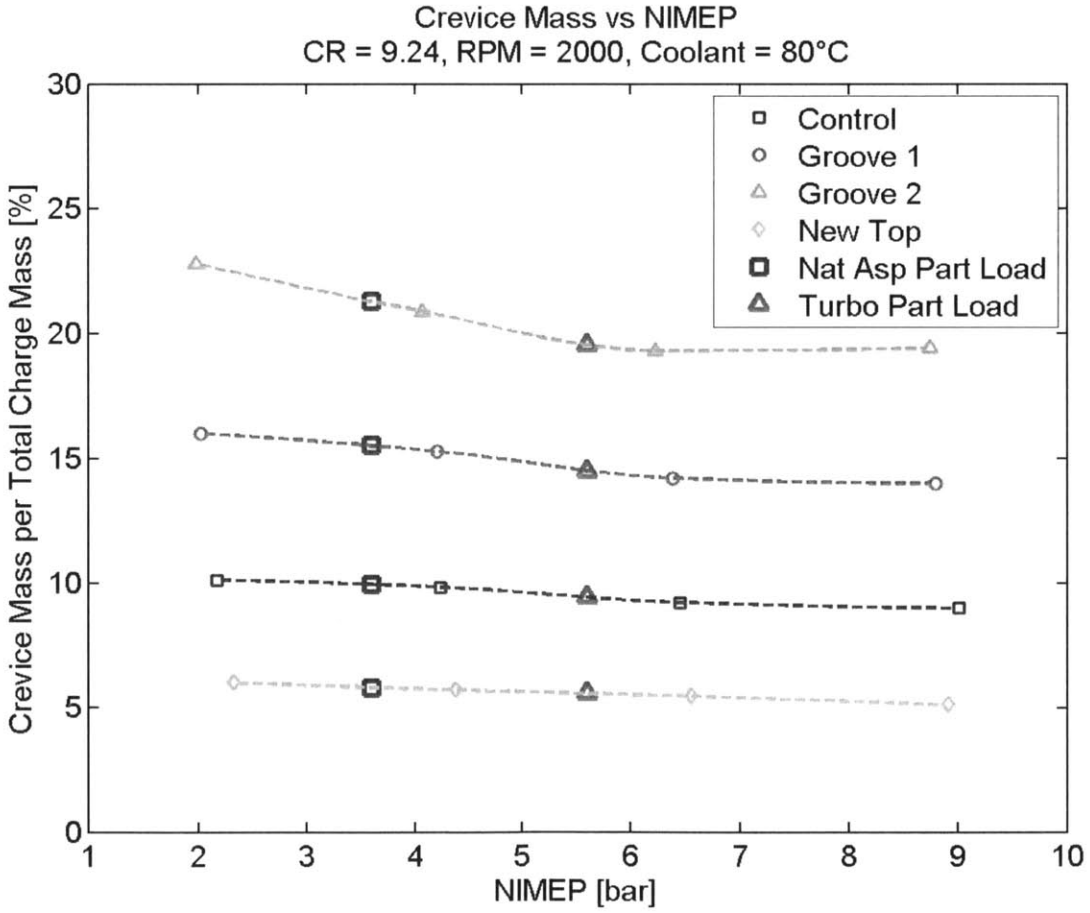

Figure 5-4 Crevice mass versus NIMEP for the baseline case at various piston crevice modifications.

5.2.3 Flame Arrival at Piston Crevice

This experimental engine employs a central spark plug for all conditions tested, which means that flame arrival at the piston crevice should come near the end of primary combustion. There will be various irregularities in the travel of the turbulent flame causing the flame front to reach different sections of the piston crevice at different times. These irregularities include: faster travel towards a warmer exhaust, tumble and swirl in the combustion chamber, and combustion chamber geometry. As an approximate look at where flame arrival occurs the crank angle of 90% mass burned (CA90) is investigated. CA90 values are found by using the one zone heat release code presented in Analysis Tools. These values correspond to the crank angle at which 90% of the primary fuel mass is burned; relative to the total mass burned at the end of primary combustion. The CA90 values for the baseline case (Table 5-2) with the control piston crevice modification are plotted alongside peak pressure locations versus NIMEP in Figure 5-5. If it is assumed that the flame approximately arrives at the crevice when 90% of the fuel mass is burned, then from this plot the approximation of flame arrival at peak pressure is not such a bad estimation. This finding is consistent with assumptions made in the simulation study and hydrocarbon emissions model. This plot and resulting conclusion is representative of nearly all additional test conditions.

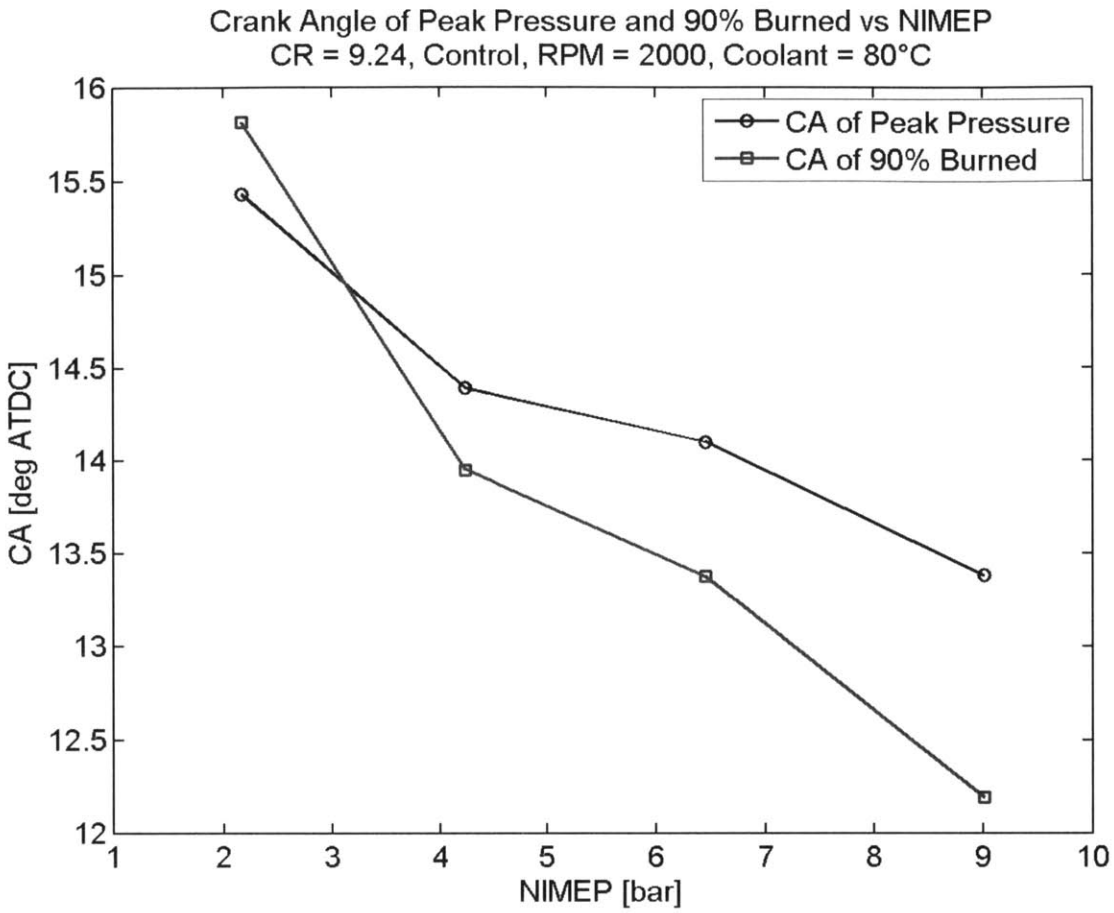

Figure 5-5 Crank angle locations of peak pressure and 90% mass burned versus NIMEP for the baseline case with control piston crevice modification.

Knowing that flame arrival coincides with peak pressure, conditions at peak pressure are used to calculate two-plate quench distances with the method described in Appendix A:. These quench distance calculations are shown along with piston crevice clearances versus NIMEP at each piston crevice modification in Figure 5-6. It is important to note that the piston crevice clearance is the clearance that would be present if the piston and cylinder were perfectly circular and concentric. This is obviously not the case so there is some added complexity involved in comparing two-plate quench distances to piston crevice clearances. The two lower NIMEP values shown (0.4 and 0.6 bar MAP) have two-plate quench distances that are higher or about equal to the simplified piston crevice clearance. This shows that for the naturally aspirated part load case, in a very simple view, most of the entrance to the piston crevice will act to quench the flame. At the two higher NIMEP values shown (0.8 and 1.0 bar MAP) the two-plate quench

distances are slightly lower than the piston crevice clearances, so at the turbocharged part load point less of the piston crevice entrance would quench the flame. Because the actual piston-cylinder clearance is so irregular this analysis can only be approximate, but can still give insight into how the two part load cases differ with changing crevice volume.

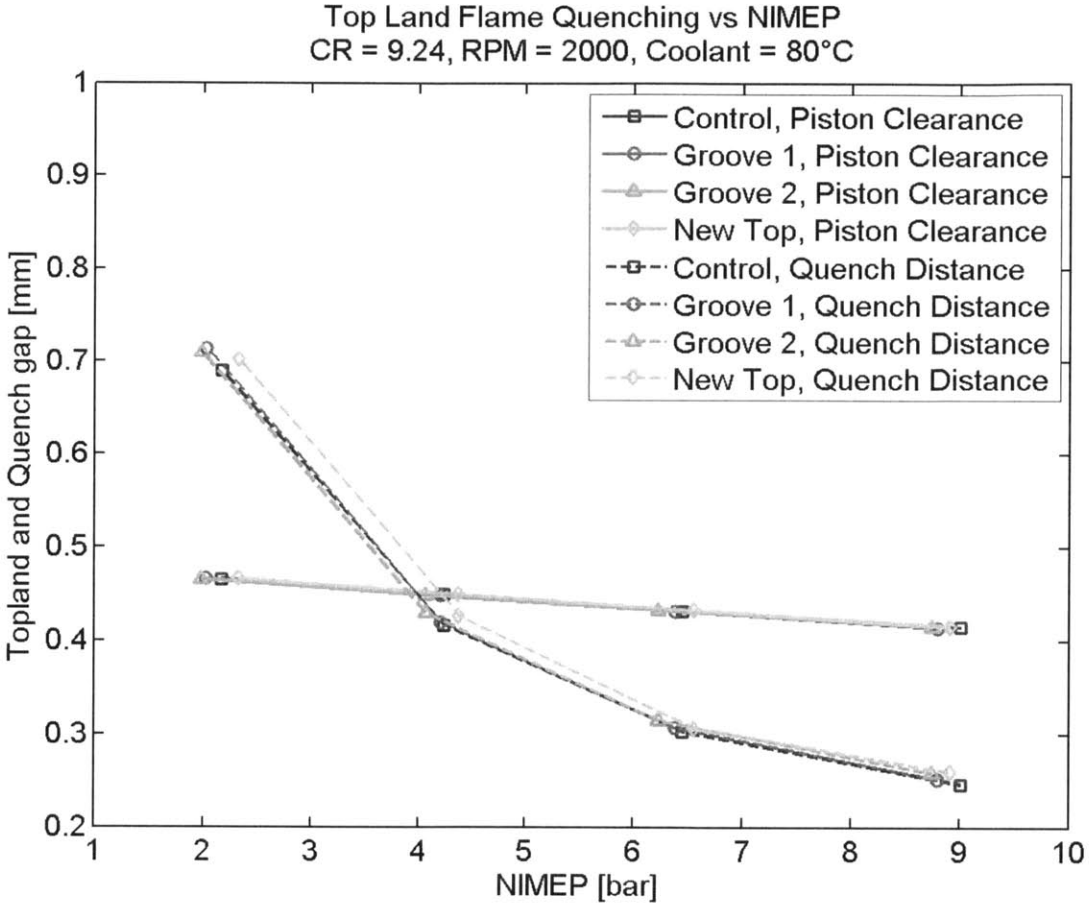

Figure 5-6 Two-plate quench distances and piston crevice clearances versus NIMEP for the baseline case at various piston crevice modifications.

5.2.4 Crevice Volume Effect on Efficiency

For the baseline case, (Table 5-2) four different MAP values are tested at each modified piston geometry, and the indicated efficiency versus NIMEP is displayed in Figure 5-7. Experimental data points are plotted as small markers, with a color-matched dashed line

representing a modified cubic interpolation connecting them. The two part load NIMEP values (Table 5-1) are interpolated and plotted for each piston crevice modification. Piston modifications listed in the legend correspond to the different crevice volume modifications presented in Table 3-4. It can be seen from this baseline case that the engine is well behaved at these conditions with similar curve shapes as crevice volume is changed. As load is increased the individual curves seem to be approaching an asymptote. As such indicated efficiency is found to increase with increasing load at an ever-decreasing rate. Across the piston crevice modifications higher efficiencies result from lower crevice volumes. Something to note is the substantial increase in efficiency with the new top land height.

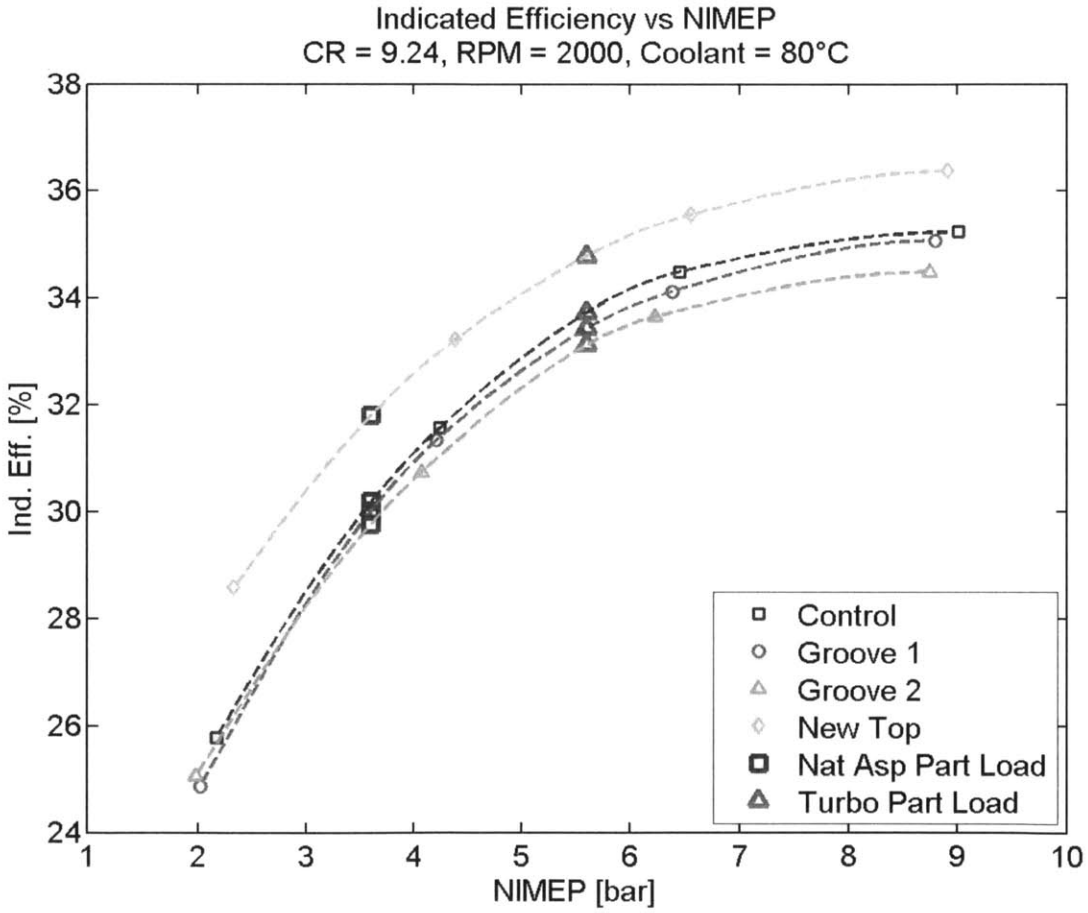

Figure 5-7 Indicated efficiency versus NIMEP for the baseline case at various piston crevice modifications.

The two part load points (Table 5-1) for the baseline case (Table 5-2) have been isolated and are shown with absolute values in Figure 5-8 and with relative values, referenced to control piston crevice modification, in Figure 5-9. In these plots efficiencies are plotted versus crevice volume, which is calculated based on thermal expansion considerations under engine operating conditions. The control piston crevice volume is the case slightly above 1000 mm^3. With the increased crevice volume absolute indicated efficiency falls approximately linearly at a rate of about 0.3-0.5%-points per 1000 mm^3. When the top ring is moved up and crevice volume decreased there is a dramatic increase in absolute efficiency of about 2.3-3.5%-points per 1000 mm^3. The corresponding rates for relative efficiency are 1.4-1.8% for a 120% increase in crevice volume and 3.1-5.3% for a 45% decrease in crevice volume. The changes in absolute and relative efficiency from decreasing crevice volume by shortening the top land height are substantial.

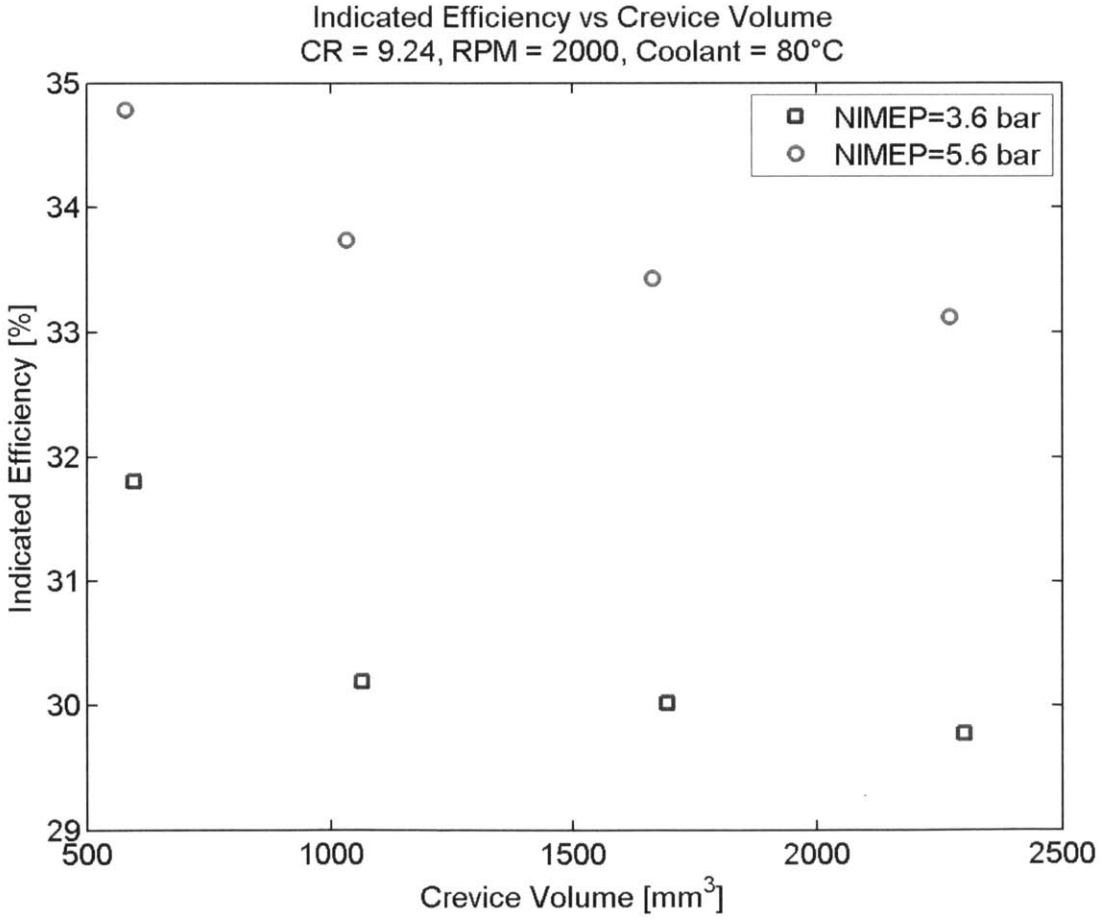

Figure 5-8 Indicated efficiency versus crevice volume for the baseline case at two part load NIMEP values.

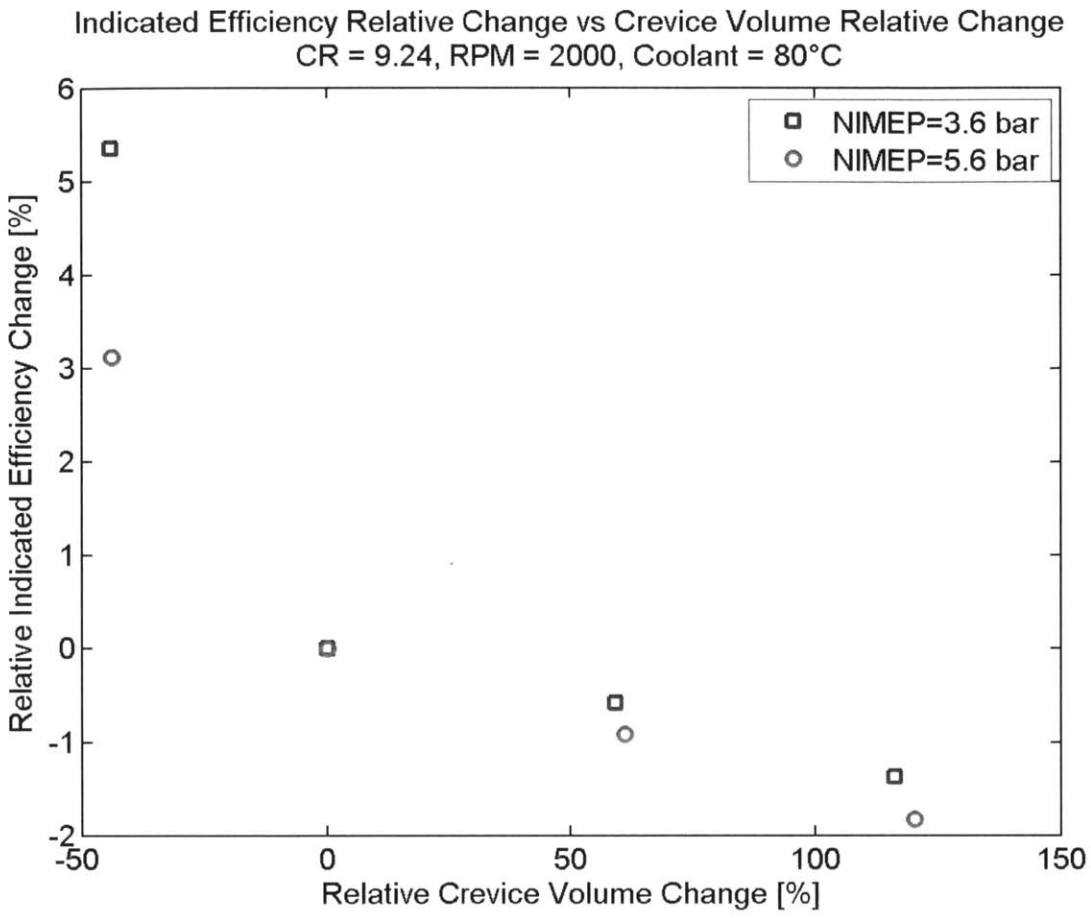

Figure 5-9 Relative indicated efficiency change versus relative crevice volume change for the baseline case at two part load NIMEP values.

To further look into the slope of efficiency versus crevice volume an approximate theoretical cycle analysis is undertaken. The net indicated efficiency accounting for the crevice loss and pumping loss is given by Equation 5.2:

$$\eta_{i,n} = \frac{W_{No\ crev} - W_{Loss,crev} - W_p}{m_f Q_{LHV}} \qquad [5.2]$$

where $\eta_{i,n}$ is the net indicated efficiency, $W_{No\ crev}$ is the gross work per cycle without the crevice, $W_{Loss,crev}$ is the work lost due to the crevice, W_p is the pumping work, m_f is fuel mass, and Q_{LHV} is the lower heating value of the fuel. The work lost due to the crevice is defined in Equation 5.3:

$$W_{Loss,crev} = E_{crv}(\eta^*_{i,g} - \eta'_{i,g}) \quad [5.3]$$

where $W_{Loss,crev}$ is the work lost due to the crevice, E_{crv} is the fuel energy of the trapped fuel in the crevice volume at peak pressure, $\eta^*_{i,g}$ is the gross indicated efficiency without the crevice, and $\eta'_{i,g}$ is the gross indicated efficiency of burning crevice gas. Fuel energy trapped in the crevice is calculated from [2.1] by accounting for A/F, and after some rearranging Equation 5.4 is formed:

$$\frac{W_{Loss,crev}}{m_f Q_{LHV}} = \frac{1}{m_f}\left[\frac{(p_{peak} - MAP)V_{crev}}{(1 + A/F)R_u T_{crev}}\right](\eta^*_{i,g} - \eta'_{i,g}) \quad [5.4]$$

where $W_{Loss,crev}$ is the work lost due to the crevice presence, m_f is fuel mass, Q_{LHV} is the lower heating value of the fuel, p_{peak} is peak pressure, MAP is manifold absolute pressure, V_{crev} is crevice volume, A/F is the air-fuel ratio, R_u is the unburned gas constant, T_{crev} is crevice temperature, $\eta^*_{i,g}$ is the gross indicated efficiency without the crevice, and $\eta'_{i,g}$ is the gross indicated efficiency of burning crevice gas. Equation 5.4 can then be inserted into Equation 5.2 and the derivative of efficiency taken with respect to crevice volume. The gross work without the crevice and pumping work are both constant with changing crevice volume and so drop out of the derivative. The unburned gas constant and burned gas constant are assumed approximately equal and the MAP is neglected because it is much smaller than peak pressure. The resulting derivative is given in Equation 5.5:

$$\frac{d\eta_{i,n}}{dV_{crev}} = -\frac{1}{V_{peak}}\frac{T_{peak}}{T_{crev}}(\eta^*_{i,g} - \eta'_{i,g}) \quad [5.5]$$

where $\eta_{i,n}$ is the net indicated efficiency, V_{crev} is crevice volume, T_{peak} is temperature at peak pressure, V_{peak} is volume at peak pressure, T_{crev} is crevice temperature, $\eta^*_{i,g}$ is the gross indicated efficiency without the crevice, and $\eta'_{i,g}$ is the gross indicated efficiency of burning crevice gas. Due to data availability, $\eta^*_{i,g}$ is approximated as the gross indicated efficiency from experiments with the crevice included. This is good to second order for small changes in

efficiency resulting from the crevice. Based on the analysis is Section 2.2.2, $\eta'_{i,g}$ is set to $0.6*\eta^*_{i,g}$. Looking at Equation 5.5 it is interesting to note that all variables are largely constant with load and speed, and thus the equation is independent of both load and speed. Experimental data for the baseline case at a MAP value of 0.6 bar and control piston crevice modification is input into [5.5] to give a slope of about -1.2 %-point per 1000 mm^3; displayed in Equation 5.6.

$$\frac{d\eta_{i,n}}{dV_{crev}} = -1.2\ \%\text{-}points\ per\ 1000\ mm^3 \qquad [5.6]$$

This value is an approximate basis for the change in net indicated efficiency brought about by varying crevice volume. It only slightly under predicts values seen in the experiments, and is clearly on the same order of magnitude as the experimental changes seen. That this theoretical slope is lower than experimental results could say that there is some flame penetration, thus changing the actual crevice volume that is escaping primary combustion. This would slide the points in Figure 5-8 to the left varying amounts, possibly matching the slopes to this theoretical value.

5.2.5 Burning Characteristics

Using the one zone heat release analysis presented in Analysis Tools, mass fraction burned curves are found for the baseline case at a MAP value of 0.6 bar for different piston crevice volume modifications. The burn curves are presented in Figure 5-10 through Figure 5-13. These figures break down the mass fraction burned into its components: sensible energy change between reactants and products, work done on piston, heat transfer, and crevice effect. The sensible energy change and piston work are combined as they are not individually of interest. From the differences between the lines information about heat transfer and crevice effect can be extracted, and from the total burn curve, comparisons can be made between different piston geometries.

The burn curves shown in Figure 5-10 to Figure 5-13 share a number of similarities with slight magnitude changes for different components. The sensible energy change plus piston work rises dramatically during combustion, reaches a peak at the end of combustion, and then steadily

decreases during expansion. Heat transfer remains small until charge temperature rises due to combustion, and then steadily increases until exhaust valve opening. The crevice effect on heat release has little impact until late in combustion and then remains relatively constant from end of combustion to exhaust valve opening. This is consistent with prior research and how the heat release code is setup to deal with the crevice effect. From the burn curve for the control piston it can be seen that a substantial portion of the in-cylinder fuel mass is pushed into the crevice.

Information regarding cumulative heat transfer loss, cumulative crevice enthalpy loss, and 10-90 burn duration is taken from burn curves similar to those in Figure 5-10 to Figure 5-13. This detailed information allows for comparisons across crevice volume and load for the baseline case.

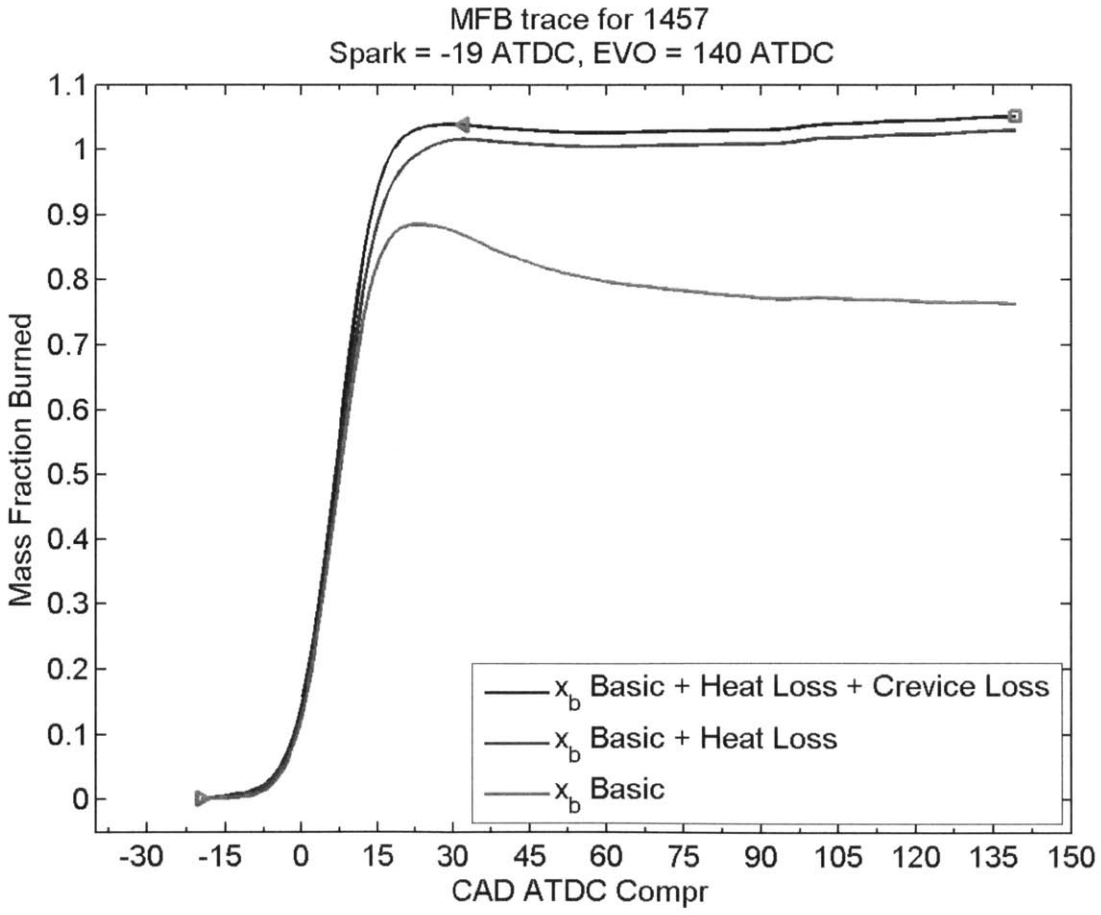

Figure 5-10 Mass fraction burn curve for the baseline case with control piston breaking down different components of heat release.

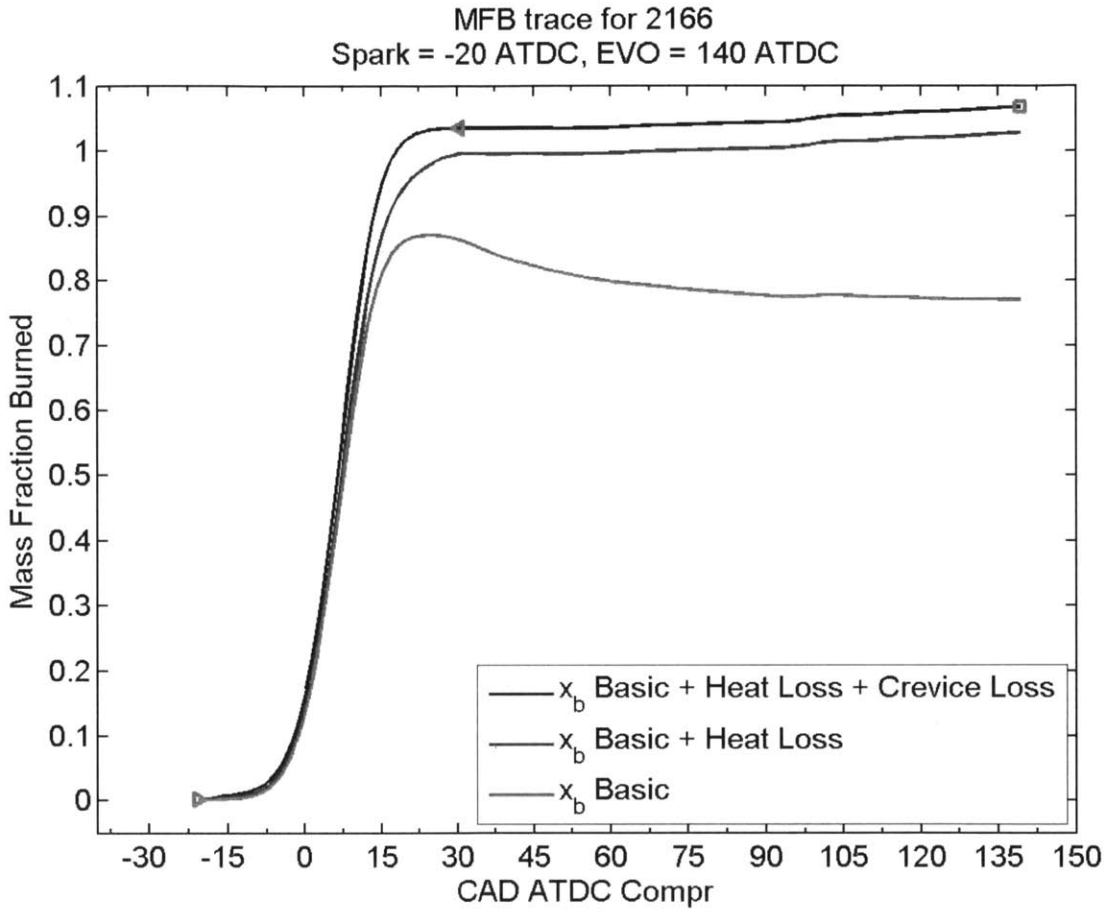

Figure 5-11 Mass fraction burn curve for the baseline case with groove 1 piston modification breaking down different components of heat release.

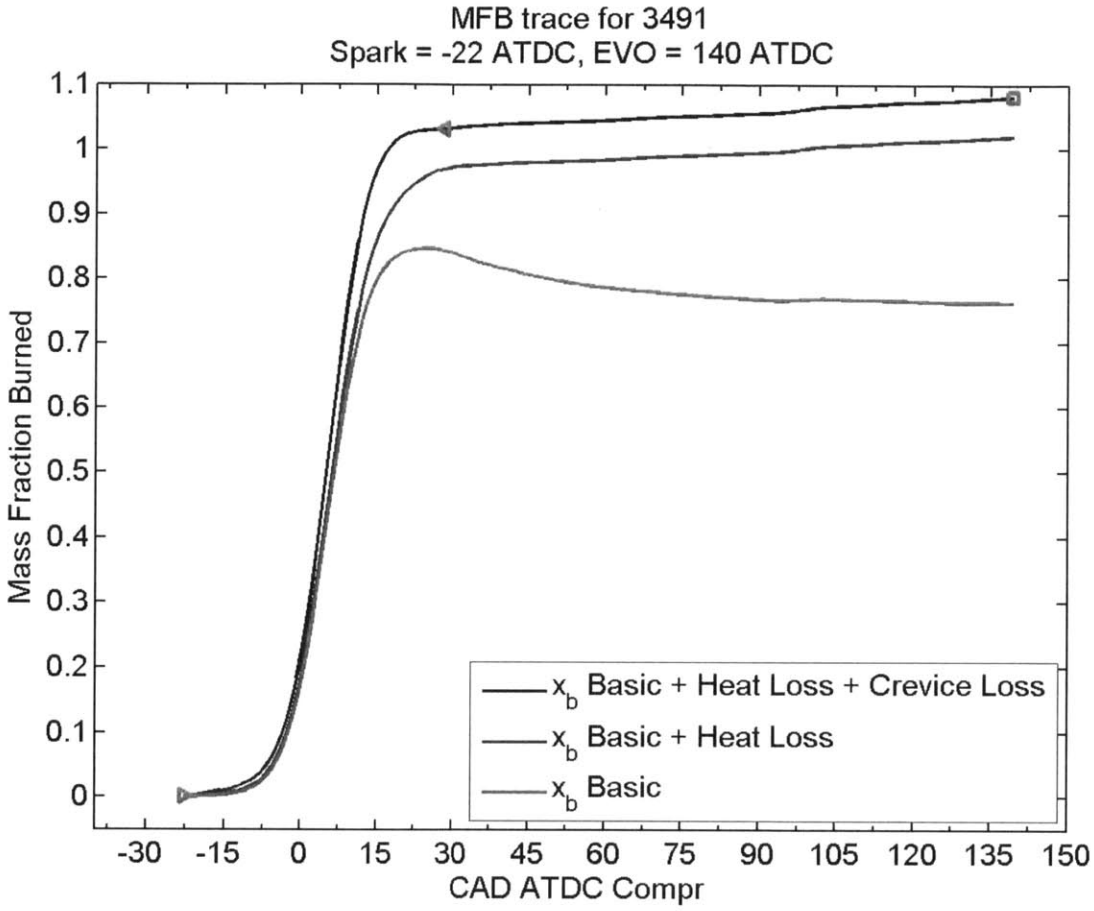

Figure 5-12 Mass fraction burn curve for the baseline case with groove 2 piston modification breaking down different components of heat release.

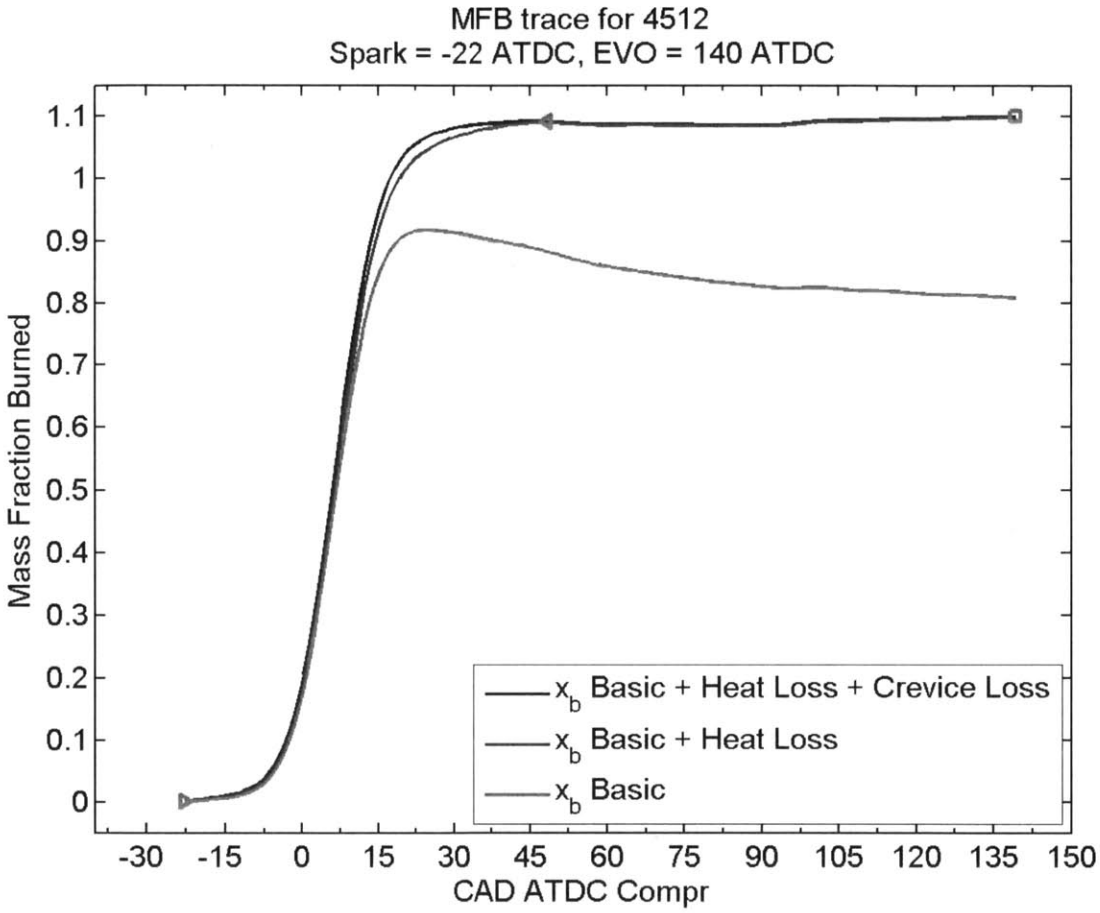

Figure 5-13 Mass fraction burn curve for the baseline case with new top land piston modification breaking down different components of heat release.

The cumulative heat transfer values at EVO per fuel energy at different piston crevice modifications have been extracted from their respective burn curves, and are plotted against NIMEP in Figure 5-14. Experimental data points are connected with a modified cubic interpolation and the two part load NIMEP values from Table 5-1 are calculated. These curves give an overview of the heat transfer loss per cycle at different loads for different piston crevice modifications. Heat transfer losses as a fraction of total fuel energy decrease with increasing NIMEP values for a given piston crevice modification. This is because in-cylinder temperatures increase at a slower rate than total fuel energy as NIMEP is increased; higher NIMEP values require significantly larger amounts of fuel but heat transfer from higher in-cylinder temperatures only increases modestly.

For all but the lowest loads larger crevice volume results in lower heat transfer loss as a fraction of fuel energy. For a given load, speed, coolant temperature, and compression ratio, increasing crevice volume lowers in-cylinder temperatures and increases total fuel energy, thus lowering the heat transfer loss per fuel energy. Lower in-cylinder temperatures result from less fuel burning during primary combustion, and higher total fuel energies result from lower engine efficiency at larger crevice volumes. There is a large jump from the control piston crevice modification to the new top land modification due to the decrease in total fuel energy from running more efficiently, and the higher combustion temperature because of less leakage to crevice. At the lowest NIMEP values tested there are some unexpected values for a couple of the piston crevice modifications, which could be due to less stable operation.

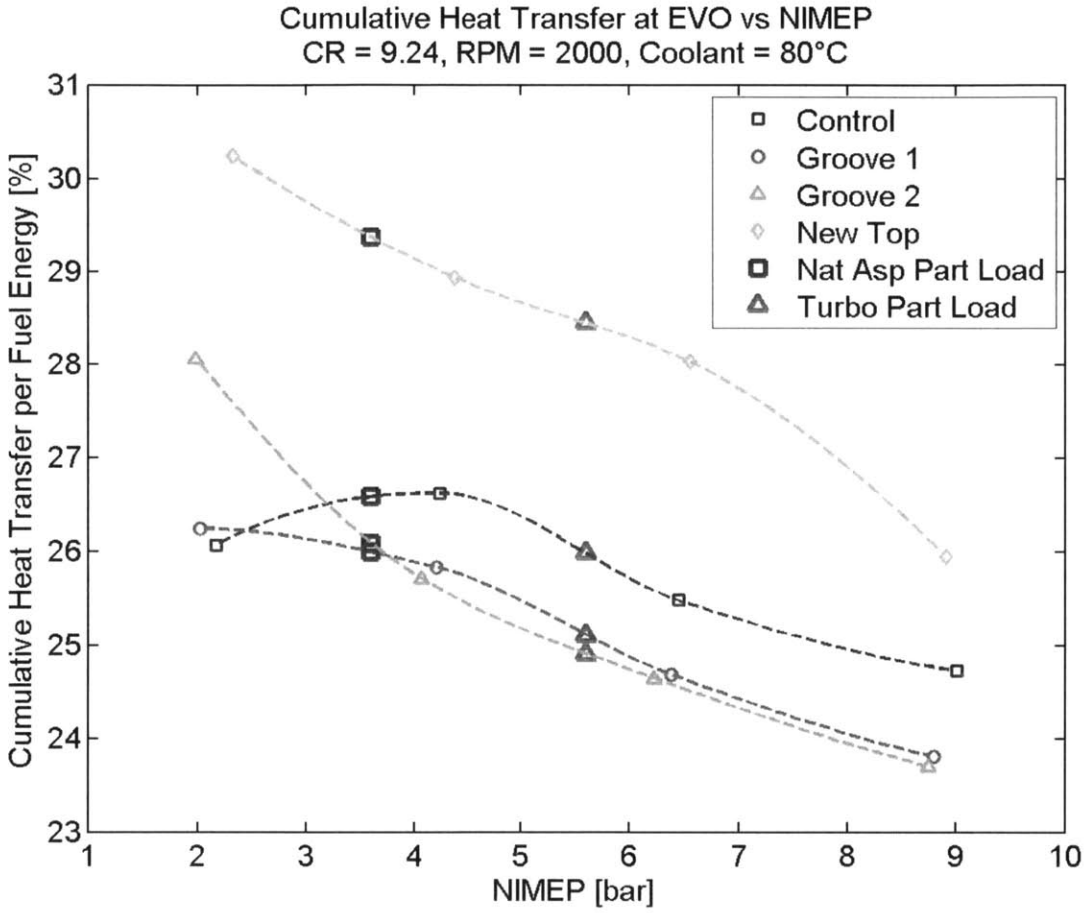

Figure 5-14 Cumulative heat transfer at EVO per fuel energy versus NIMEP for the baseline case at various piston crevice modifications.

The cumulative crevice enthalpy change values at EVO per fuel energy at different crevice volumes have been extracted from their respective burn curves, and are plotted against NIMEP in Figure 5-15. Experimental data points are connected with a modified cubic interpolation and the two part load NIMEP values from Table 5-1 are calculated. The cumulative crevice enthalpy change here is defined as the net enthalpy flow into the crevice; total enthalpy into crevice minus total enthalpy out of the crevice. This value does not account for the secondary burning of the crevice gas and simply provides a correction for traditional chemical heat release analysis. Curves for individual piston crevice modifications are essentially constant with load because trapped crevice fuel mass as a fraction of total fuel mass very nearly remains constant as load is increased. This result agrees with a conclusion from the simulation study; trapped crevice fuel mass as a fraction of total mass is independent of load.

Looking across different piston crevice modifications, larger crevice volumes lead to higher cumulative crevice enthalpy changes per fuel energy. This is intuitive since larger crevice volume allows more fuel mass to be trapped in the crevice. Looking at the approximately equal spacing between the various curves, and knowing that crevice volume modifications are very nearly linear, it can be concluded that the crevice enthalpy loss due to the crevice is linear.

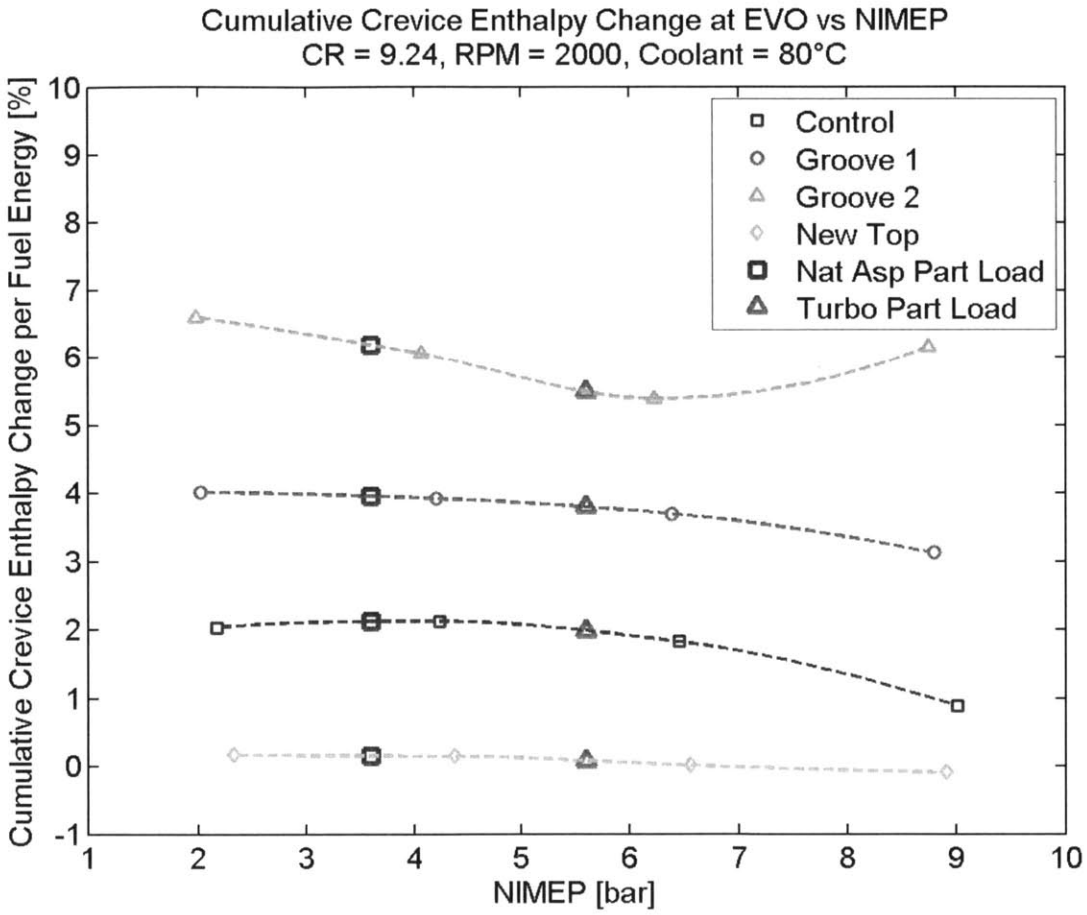

Figure 5-15 Cumulative crevice enthalpy change at EVO per fuel energy versus NIMEP for the baseline case at various piston crevice modifications.

The 10-90 burn durations at different crevice volumes have been extracted from their respective burn curves, and are plotted against NIMEP in Figure 5-16. Experimental data points are connected with a modified cubic interpolation and the two part load NIMEP values from Table 5-1 are calculated. These burn durations give information about the speed of primary combustion; given a constant speed a lower 10-90 burn duration value equates to a faster primary combustion event. The curves for individual piston crevice modifications decrease with increasing NIMEP values, meaning that primary combustion is faster with higher load. This is due to increased charge motion and a denser charge increasing flame propagation speeds. The curves are nearly linear with NIMEP except for slightly higher burn durations at the lowest NIMEP values. At the lowest NIMEP values combustion instability, especially poor charge motion, and a much dispersed charge act to increase burn durations above the expected linear trend.

Comparing across piston crevice modifications, the new top land modification seems to be fundamentally different from the other cases. Burn durations seem to be independent of piston crevice volume for the control, groove 1, and groove 2 piston crevice modifications, but the top land modification has higher 10-90 burn durations for all NIMEP values tested. This burning duration depends mainly on stoichiometry (which remains at $\lambda = 1$) and MAP (which affects residual fraction and charge motion). For the new top land modification higher efficiency leads to lower MAP values (and thus higher residual fraction and lower charge motion) for a given NIMEP value, thus extending burn duration.

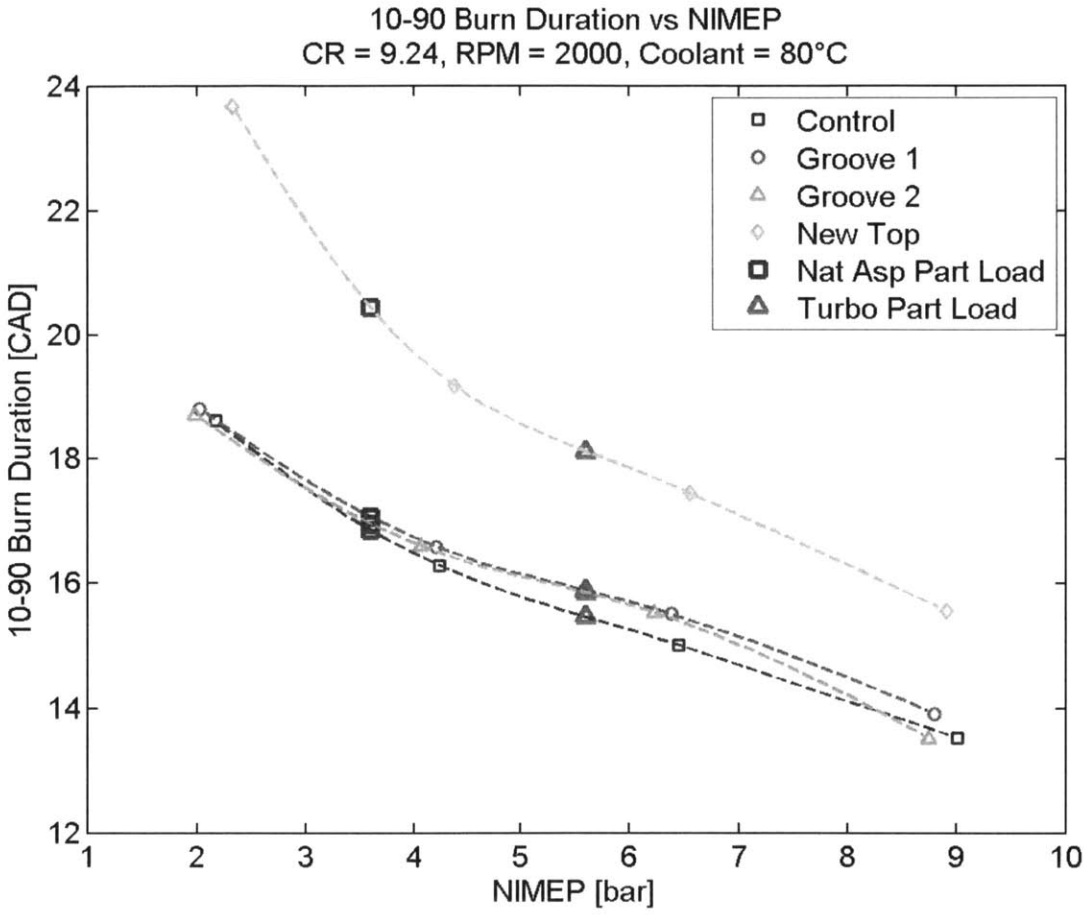

Figure 5-16 10-90 burn durations versus NIMEP for the baseline case at various piston crevice modifications.

5.2.6 Emissions

Hydrocarbon emissions results verify previous studies while simultaneously providing valuable insight on the oxidation of trapped crevice gas. For the baseline case at the control piston crevice modification, hydrocarbon emission indices are plotted along with the three hydrocarbon emission models against NIMEP in Figure 5-17. Here it can be seen that the FFID results fall between the flowchart model and complete oxidation model. This is expected as engines have progressed to limit hydrocarbon emissions since the basis for the flow chart model was created. That the values fall between these two models reinforces reliability of the hydrocarbon emission measurements, and shows that at least some of the fuel mass trapped in the piston crevice is escaping primary combustion.

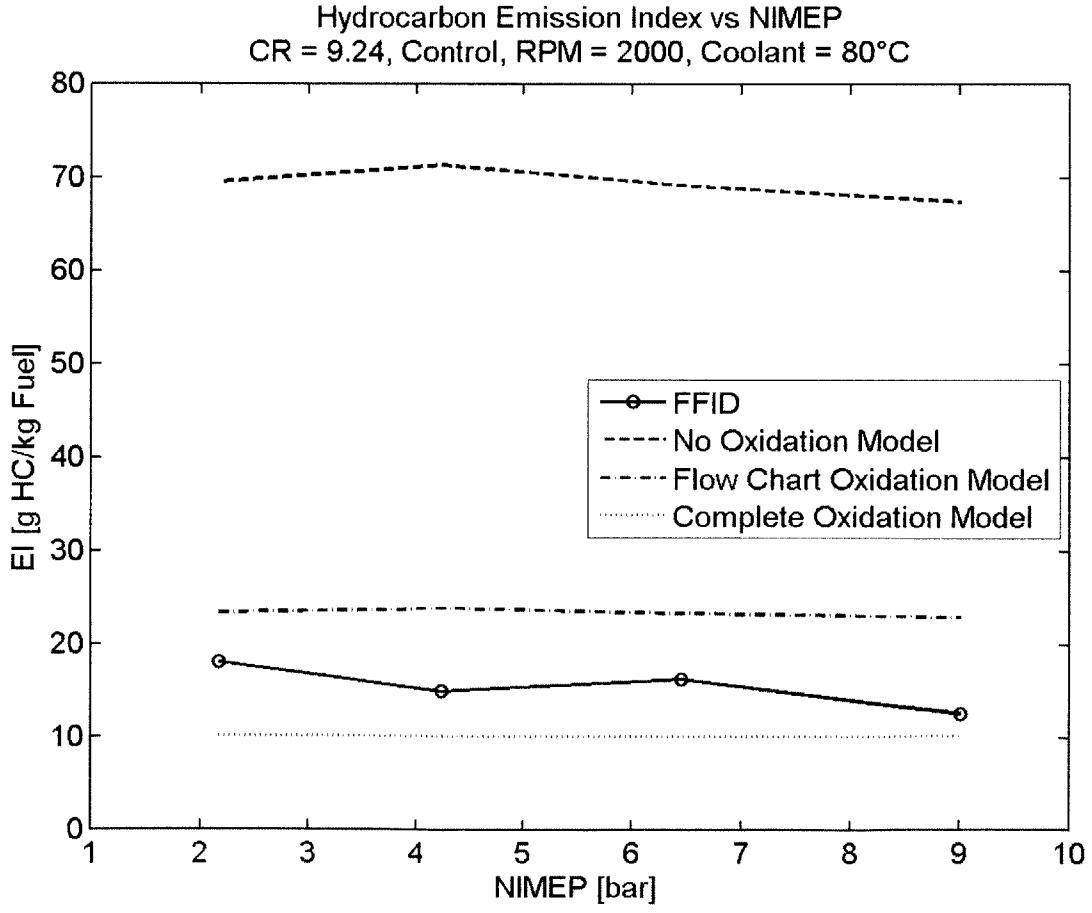

Figure 5-17 Hydrocarbon emission index versus NIMEP showing crevice models and FFID measurements for compression ratio of 9.24, control, 2000 rpm, 80°C coolant.

Results for the baseline case at various piston crevice modifications are displayed as emissions indices versus NIMEP in Figure 5-18. Experimental data points are connected with a modified cubic interpolation and the two part load NIMEP values from Table 5-1 are calculated. The hydrocarbon emission index in these experiments is defined as the steady state mass flow rate of HC emissions in grams divided by the steady state mass flow rate of fuel in kilograms. The curves tend to decrease with increased load, with the exception of the MAP = 0.8 bar (NIMEP ~6.5 bar) test point for the control and groove 1 piston modifications, which both increase slightly. Looking across piston crevice modifications, modifications with the highest crevice volumes tend to have the highest hydrocarbon emission values. Results for hydrocarbon emission indices have also been obtained from the piston-ring pack model and match experimental results in both magnitude and trend.

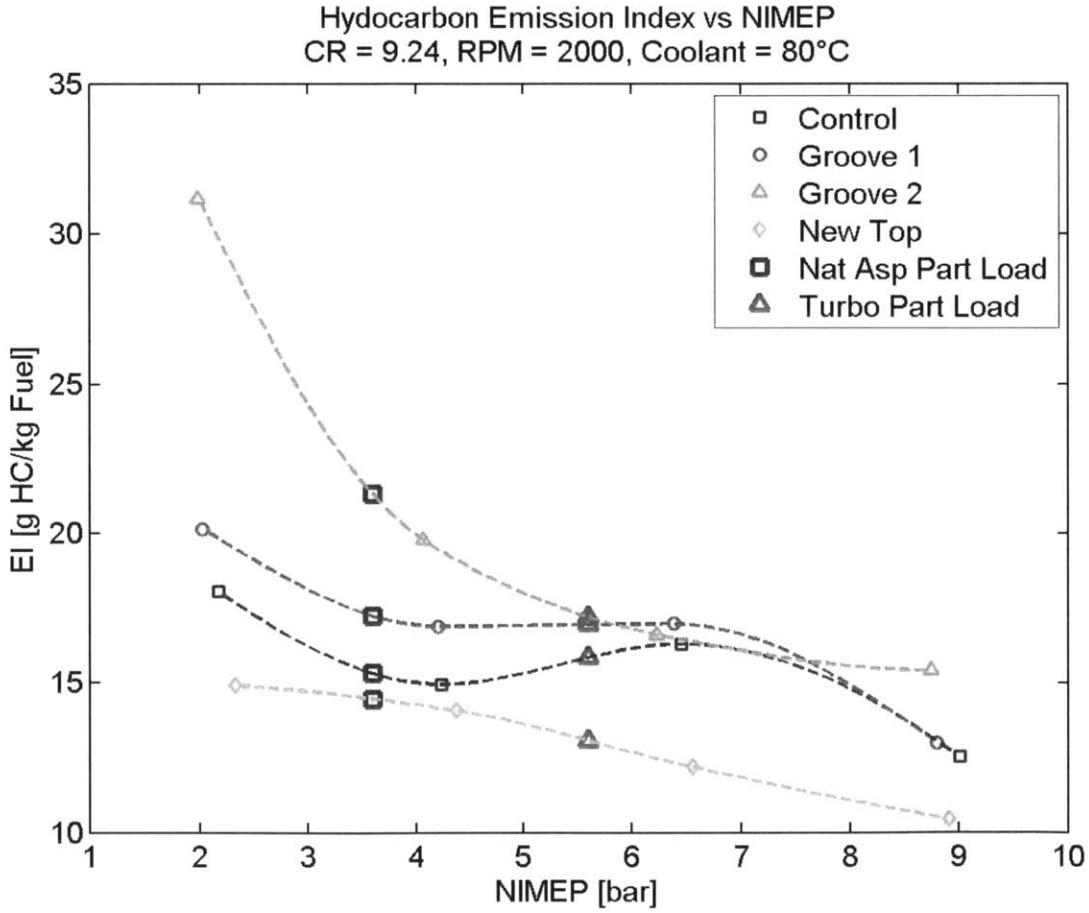

Figure 5-18 Hydrocarbon emission index (g HC/kg fuel) versus NIMEP for the baseline case at various piston crevice modifications.

The two part load points (Table 5-1) for the baseline case (Table 5-2) have been isolated and are shown with absolute values in Figure 5-19 and with relative values, referenced to control piston crevice modification, in Figure 5-20. At both of the load points hydrocarbon emission indices rise with increased crevice volume, but do so with different concavities. The absolute values for the lower load case tend to be above those for the higher load. This is especially prevalent in the largest crevice volume case. This could be caused by higher component and in-cylinder temperatures allowing for oxidation of crevice gas further into the expansion stroke. Focusing on the relative changes it can be concluded that, for this experimental setup, lowering the crevice volume from the control case provides more benefit at high load, and increasing the crevice volume from control causes more hydrocarbon emissions at low load.

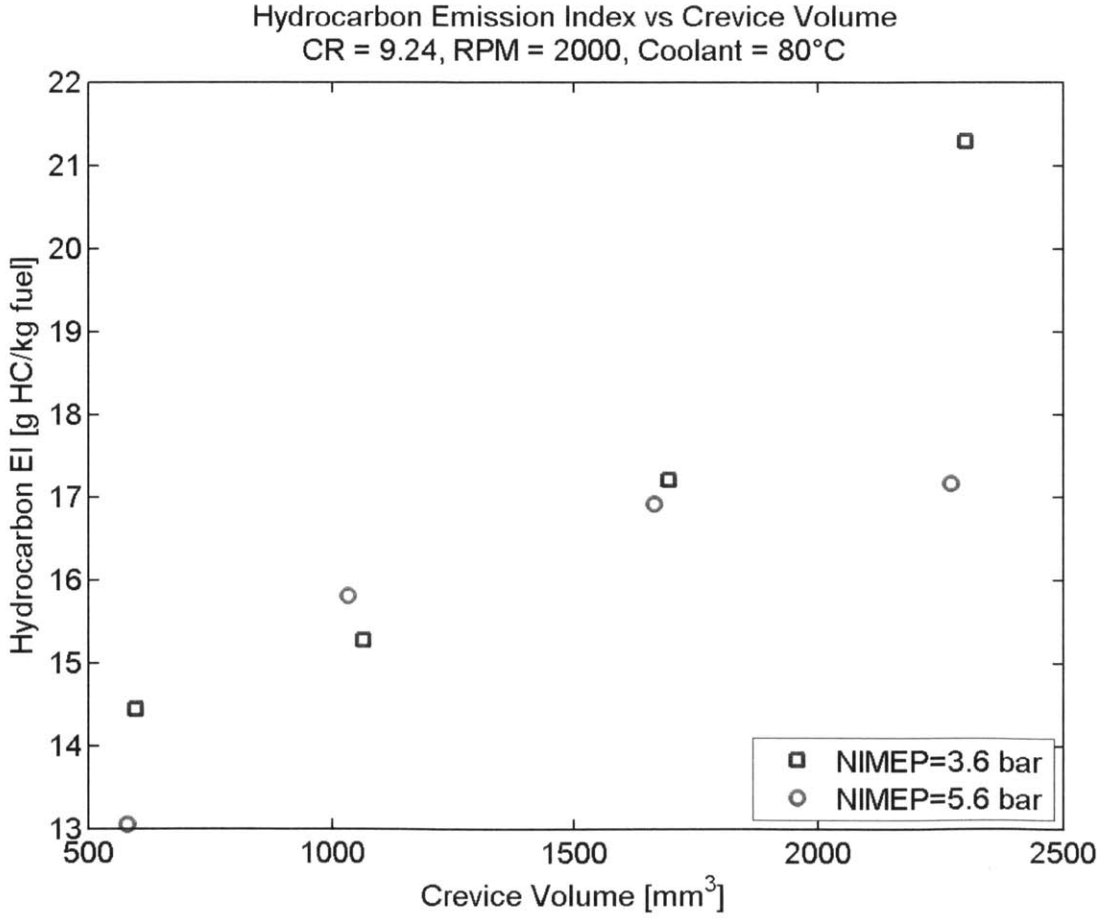

Figure 5-19 Hydrocarbon emission index (g HC/kg fuel) versus crevice volume for the baseline case at two part load NIMEP values.

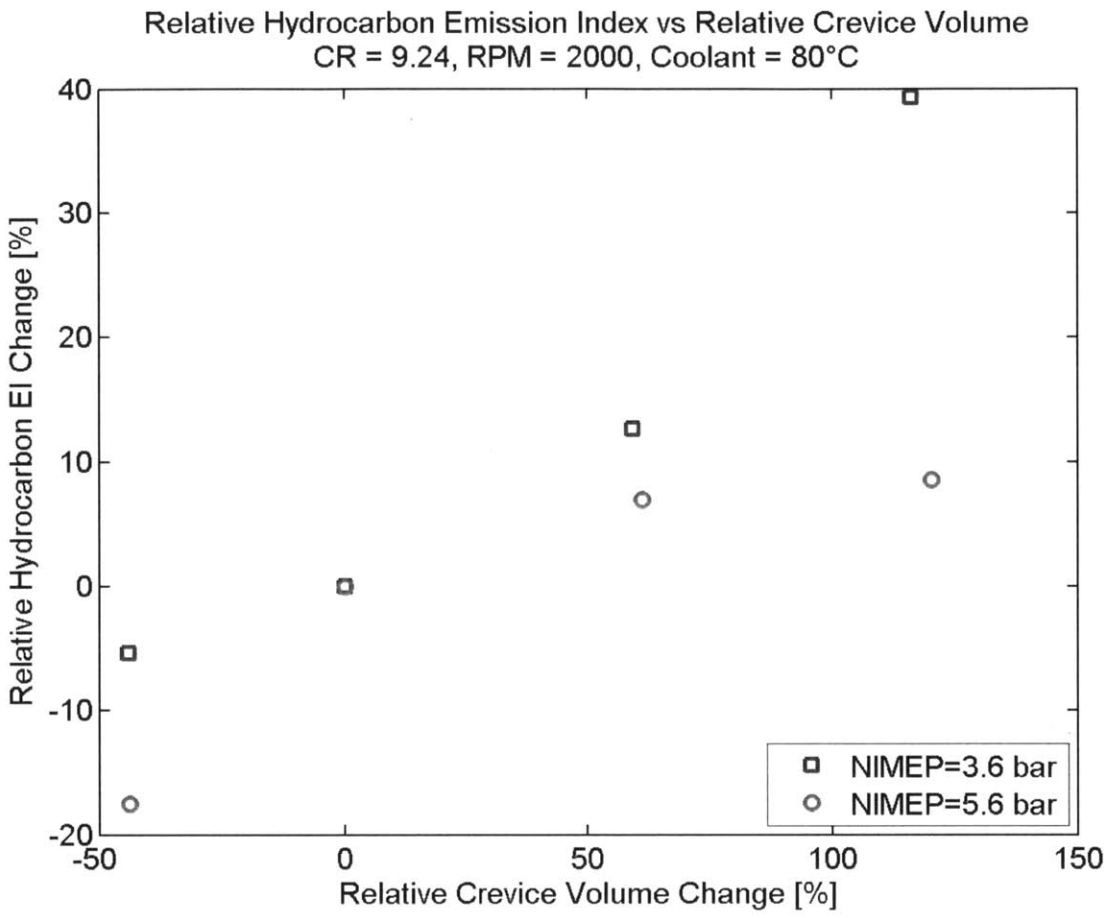

Figure 5-20 Relative hydrocarbon emission index change versus relative crevice volume change for the baseline case at two part load NIMEP values.

Combustion inefficiency is calculated from CO, H_2, and HC values. CO values are measured directly from a NDIR, H2 values are calculated based on the CO measurements and the water-gas shift, and HC values are measured using the FFID. These emissions values are then plugged into Equation 5.7:

$$1 - \eta_c = \frac{\sum_i \dot{m}_i Q_{LHV_i}}{\dot{m}_f Q_{LHV_f}} \qquad [5.7]$$

where $1 - \eta_c$ is combustion inefficiency, $\dot{m}_i$ is mass flow rate of each emission component, Q_{LHV_i} is the lower heating value of each emission component, $\dot{m}_f$ is fuel mass flow rate, Q_{LHV_f} is the lower heating value of the fuel. Results for the baseline case at various piston crevice modifications are displayed as combustion inefficiencies versus NIMEP in Figure 5-21. Experimental data points are connected with a modified cubic interpolation and the two part load NIMEP values from Table 5-1 are calculated. Curves for each piston crevice modification do not follow any consistent trend. At low NIMEP values the trend across piston crevice modification matches that for the hydrocarbon emissions in that as crevice volume is increased combustion inefficiency increases.

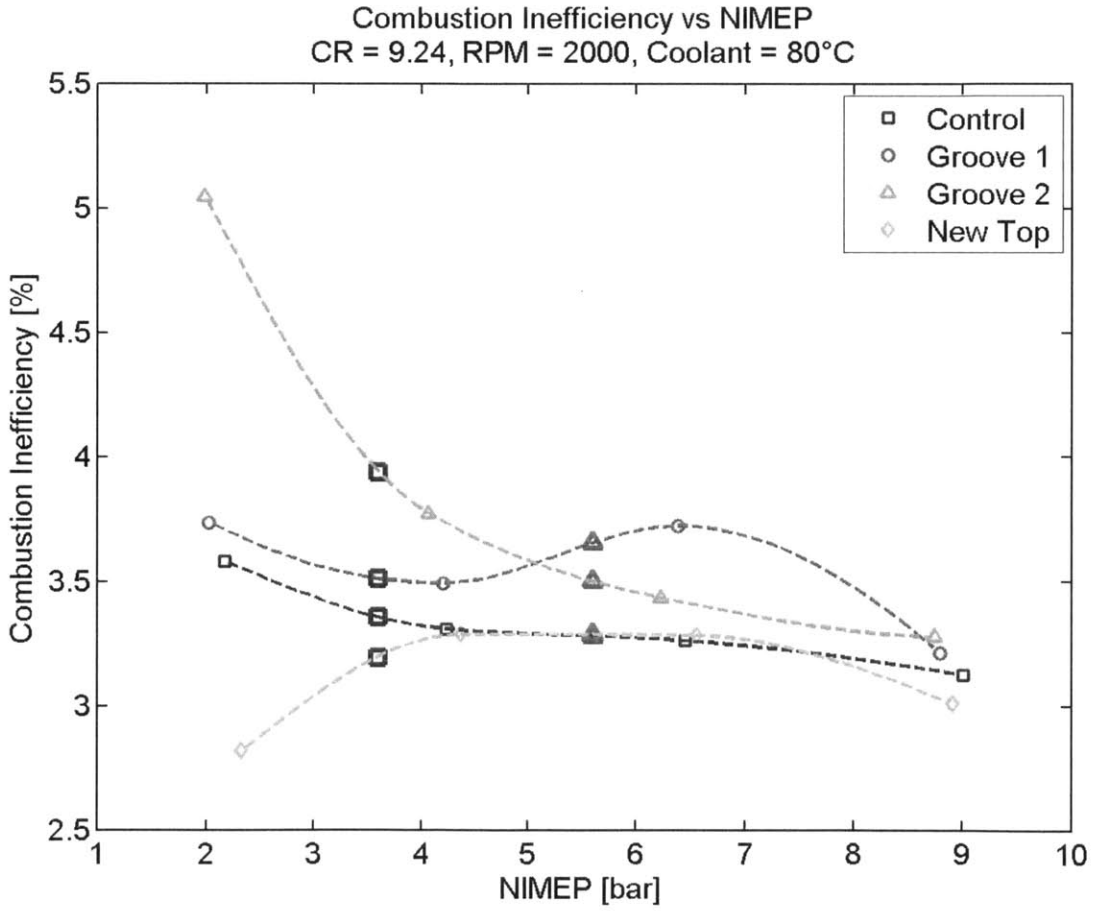

Figure 5-21 Combustion inefficiency versus NIMEP for the baseline case at various piston crevice modifications.

5.2.7 Blowby

At the baseline case (Table 5-2) blowby has been calculated from a piston-ring dynamic simulation for the various crevice volumes and MAP values summarized in Table 4-1. Blowby is found to be 6.04e-5 kg/s or about 1.54% of the total flow for the baseline case at a MAP value of 0.6 bar. This blowby flow causes an efficiency loss based on the amount of fuel mass trapped in the blowby gas. An approximate estimate of this fraction would be that about 50% of the blowby mass is unburned mixture, meaning that about half of the percentages of total flow reported will apply to escaping fuel mass. Since blowby is not recycled in this engine any changes in blowby with varied engine parameters will contribute to slight efficiency differences.

Increasing the MAP to 0.8 bar increases the blowby value to 9.69e-5 kg/s; about 1.75% of the total flow. The increased percentage of total flow slightly degrades measured efficiency, but this is largely covered up by the larger increases associated with operating at higher loads.

The most important look at blowby for the baseline case is across the different piston crevice modifications. At the largest piston crevice modification (groove 2) the blowby value is found to be 5.97-5 kg/s; about 1.56% of the total flow. At the smallest piston crevice modification (new top) the blowby value is found to be 6.24-5 kg/s; about 1.62% of the total flow. These numbers are essentially identical and thus blowby does not play a role in efficiency values across crevice modifications for the baseline case.

5.3 Effect of Compression Ratio

5.3.1 Compression Ratio Effect on Efficiency

The effect of compression ratio change on engine indicated efficiency is examined using experimental data for the control piston modification at 2000 rpm and 80°C coolant temperature. The indicated efficiency values for different compression ratios are plotted versus NIMEP in Figure 5-22. Experimental data points are connected with a modified cubic interpolation and the two part load NIMEP values from Table 5-1 are calculated. From the experimental results is can be seen that the efficiency curves are roughly parallel and are shifted up at higher compression

ratio. From the limited number of compression ratios tested a diminishing return can be seen as compression ratio is increased.

The two part load points (Table 5-1) have been isolated and are plotted against compression ratio in Figure 5-23. Efficiency values are plotted as relative changes, referenced to a standard compression ratio of 10. Here the diminishing return with compression ratio increase is further emphasized. Increasing the compression ratio from 10 to 12.57 results in approximately a 2% relative increase in indicated efficiency for both of the NIMEP values tested.

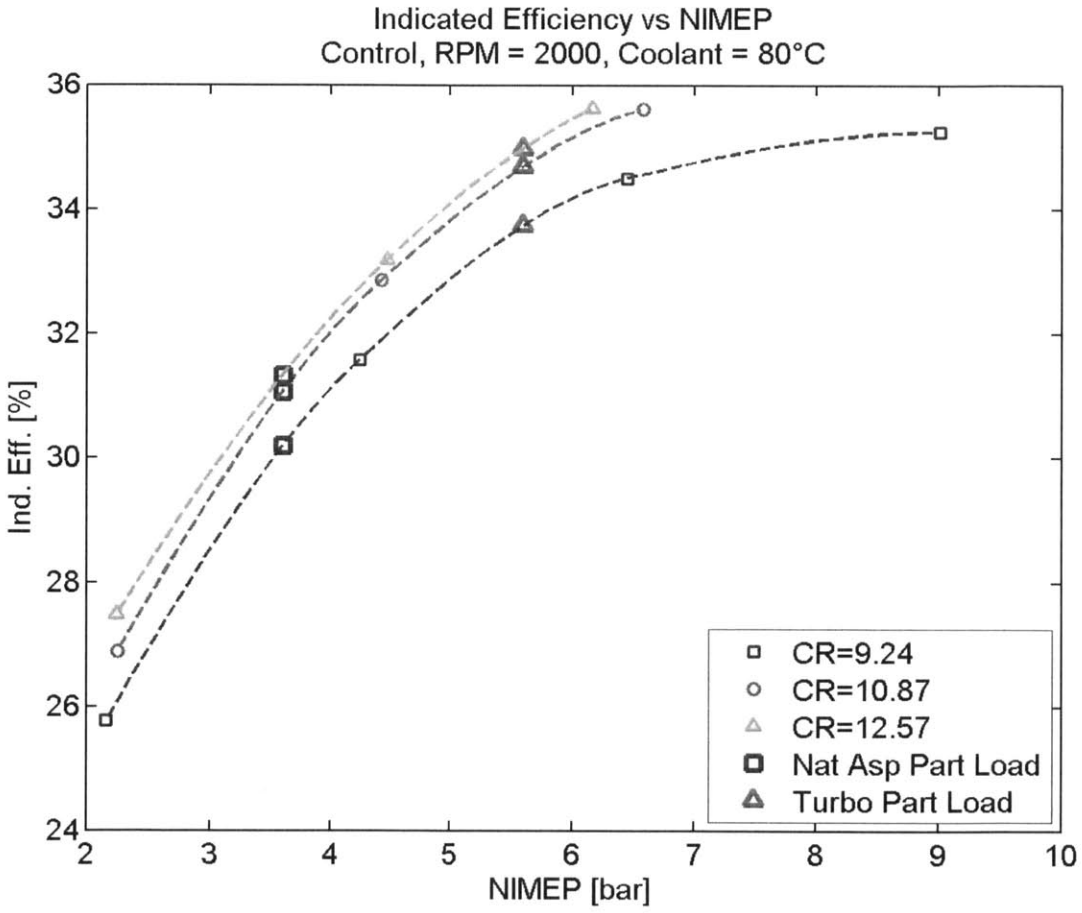

Figure 5-22 Indicated efficiency versus NIMEP for the control piston modification, speed of 2000 rpm, and 80°C coolant temperature at various compression ratios.

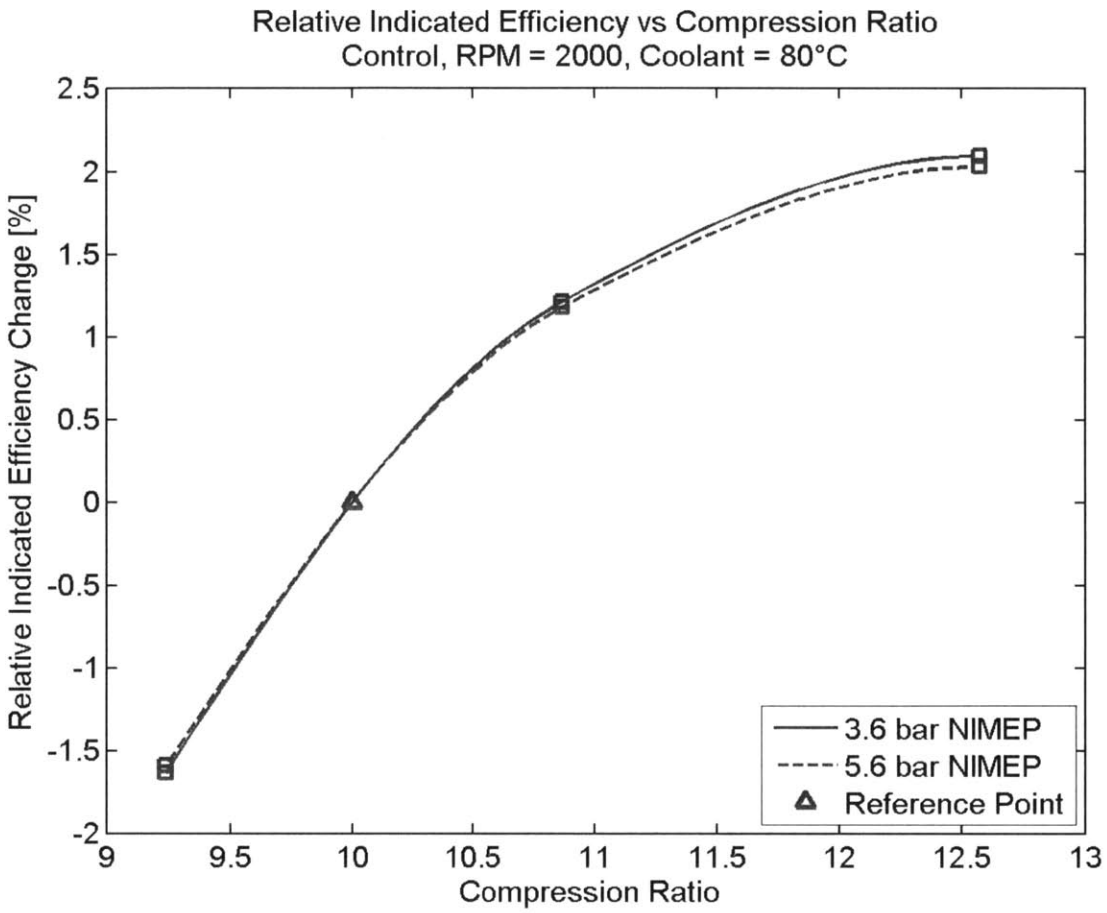

Figure 5-23 Relative indicated efficiency change versus compression ratio for the control piston modification, speed of 2000 rpm, and 80°C coolant temperature at two part load NIMEP values; referenced to a compression ratio of 10.

5.3.2 Baseline Case with Compression Ratio Effect

The efficiency effects of changing compression ratio for the control piston modification at 2000 rpm and 80°C coolant temperature are used to approximate the efficiency effects of slight changes in compression ratio resulting from crevice volume change. Specifically, efficiency values at the three different compression ratios for the control piston crevice modification at 2000 rpm, 80°C coolant temperature, and corresponding load are taken as the basis for interpolation. When crevice volume is changed in these experiments clearance volume is altered slightly, thus changing compression ratio. These slight changes in compression ratio are then plugged into the interpolation to find the degree to which efficiency change from crevice

modification is due to altered compression ratio. Results of this analysis are shown in Figure 5-24 and Figure 5-25. Figure 5-24 plots absolute values while Figure 5-25 plots relative changes. Looking at the absolute values the changes from compression ratio are almost nonexistent for all but the biggest crevice volume. These effects are slightly more noticeable in the relative plot and slightly counteract the changes seen from changing compression ratio. As crevice volume is increased compression ratio decreases slightly, thus decreasing efficiency. The opposite is true with decreased crevice volume. Overall these effects are very small and can be neglected in analyzing the effect of crevice volume on engine efficiency.

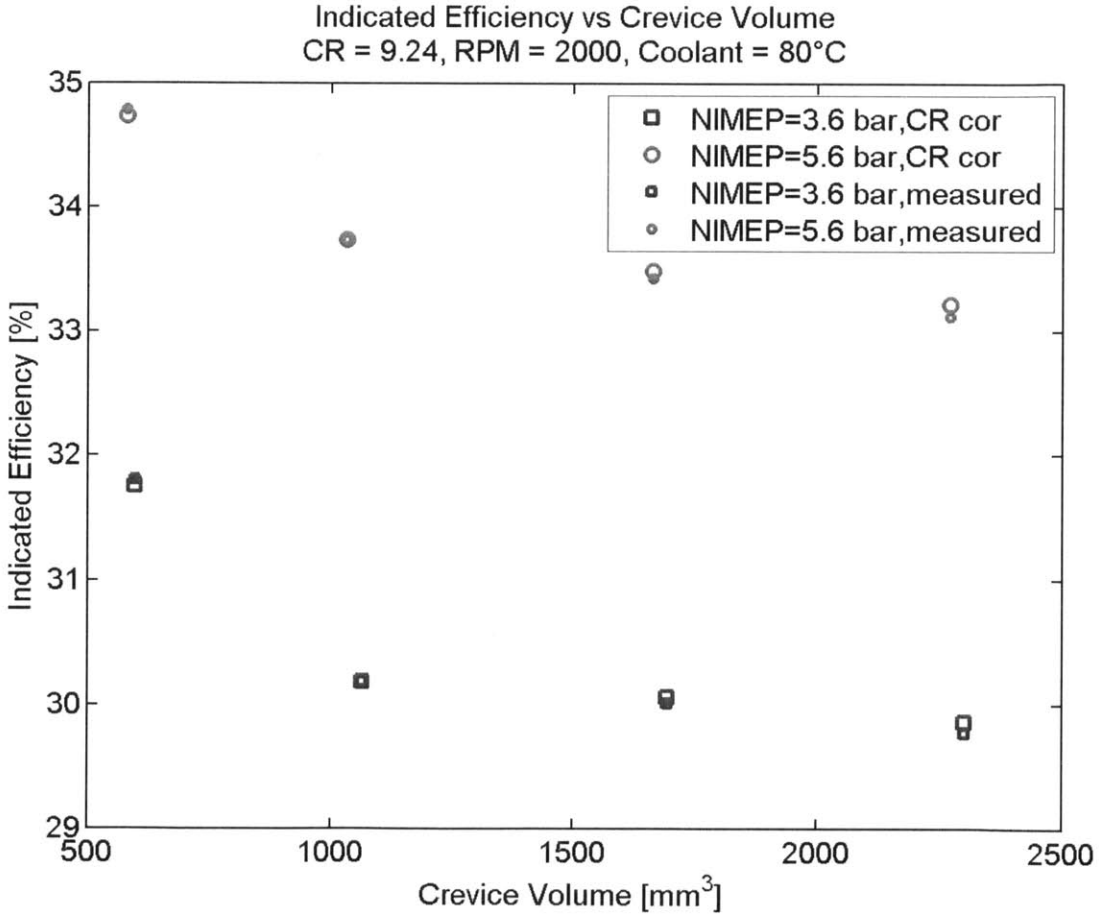

Figure 5-24 Indicated efficiency versus crevice volume for the baseline case at two part load NIMEP values; corrected for compression ratio change resulting from crevice volume change.

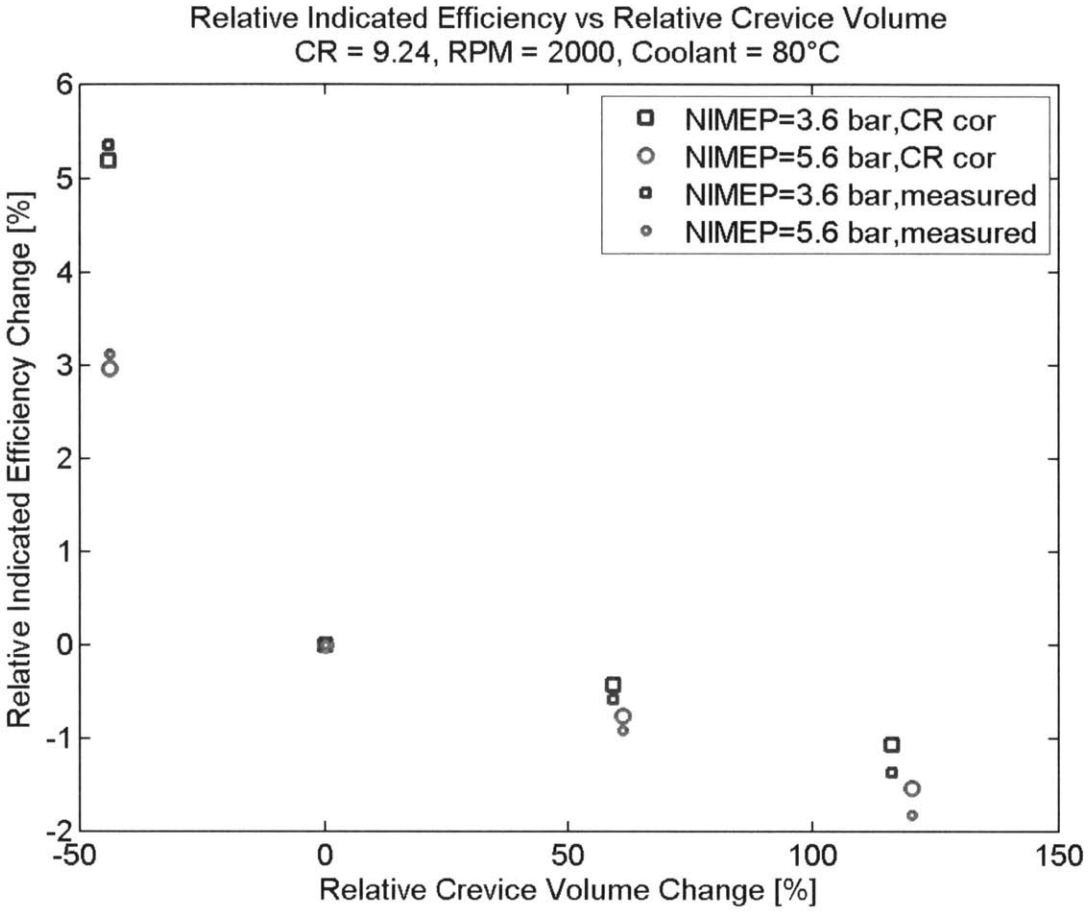

Figure 5-25 Relative indicated efficiency change versus relative crevice volume change for the baseline case at two part load NIMEP values; corrected for compression ratio change resulting from crevice volume change.

5.3.3 Crevice Volume Effect on Efficiency

For all three compression ratios efficiencies are measured for each modified piston geometry at 2000 rpm and 80°C coolant temperature. The two part load points (Table 5-1) have been isolated in Figure 5-26 through Figure 5-29. In Figure 5-26 indicated efficiencies are plotted against crevice volume for an NIMEP value of 3.6 bar at the different compression ratios. In Figure 5-27 the relative changes in indicated efficiency are plotted against relative changes in crevice volume; both referenced to the control piston crevice modification. There is one obvious outlier in the data, (CR=12.57, highest crevice volume) which is most likely due to some error in

the experimental setup during this test day. Neglecting this point, the different compression ratios respond very similarly to changing crevice volume. The relative changes in efficiency collapse nicely, meaning that for this experimental setup, NIMEP value, and range of compression ratios the crevice effect on engine efficiency is roughly independent of compression ratio.

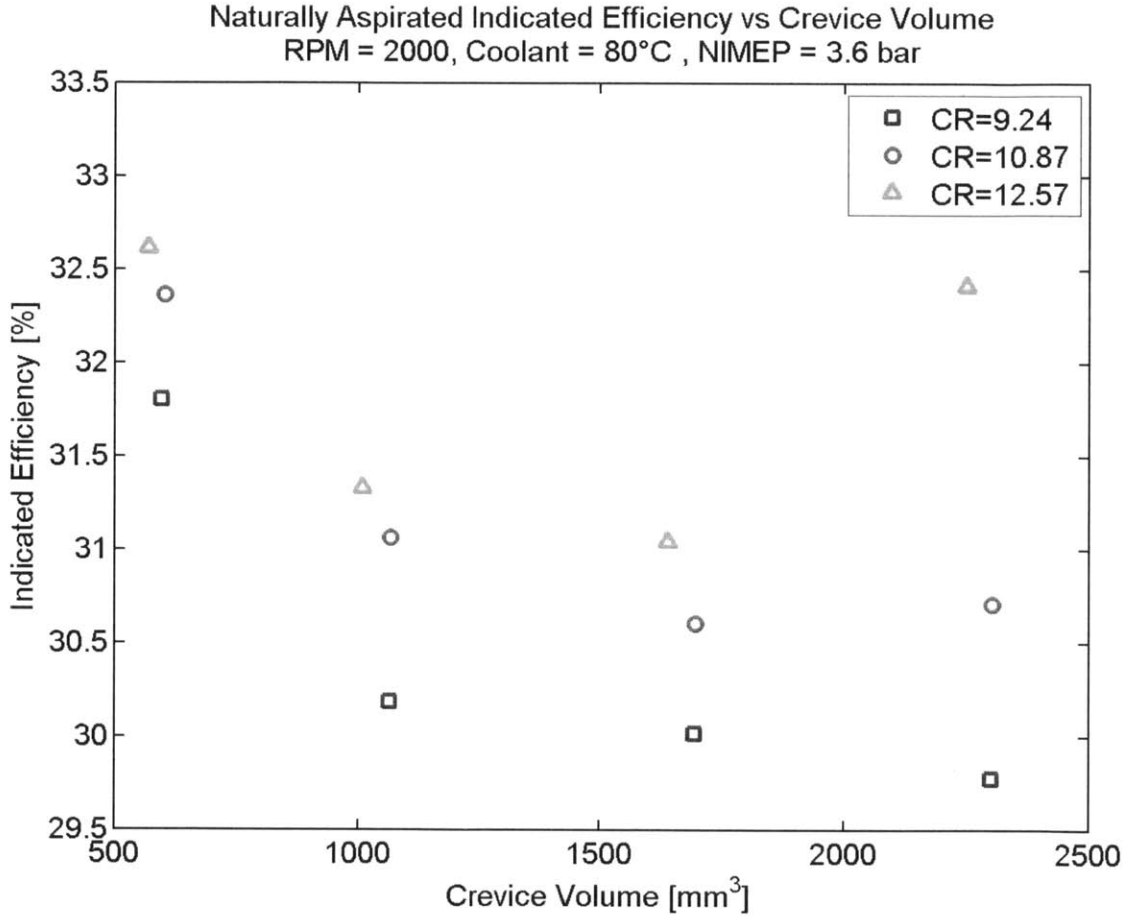

Figure 5-26 Indicated efficiency versus crevice volume for a speed of 2000 rpm, 80°C coolant temperature, and an NIMEP value of 3.6 bar at various compression ratios.

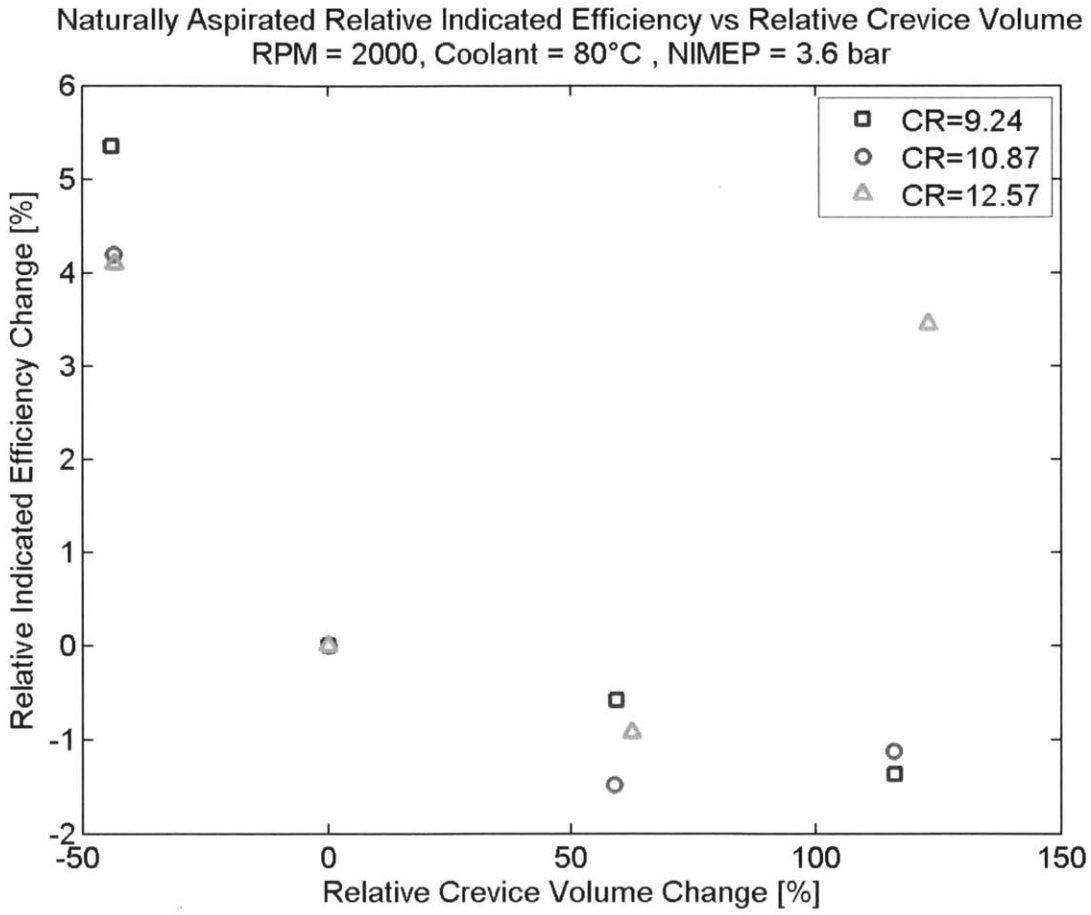

Figure 5-27 Relative indicated efficiency change versus relative crevice volume change for a speed of 2000 rpm, 80°C coolant temperature, and an NIMEP value of 3.6 bar at various compression ratios.

Figure 5-28 and Figure 5-29 focus on efficiencies at the turbo-downsized load point. In Figure 5-28 indicated efficiencies are plotted against crevice volume for an NIMEP value of 5.6 bar at different compression ratios, and in Figure 5-29 these efficiencies and crevice volumes are shown as relative changes from the control piston crevice modification. At this higher load point efficiencies for all compression ratios have increased. Trends are similar across compression ratio, and except for the one outlier point mentioned earlier, the relative efficiencies collapse. For this engine speed, coolant temperature, and NIMEP value the crevice effect on engine efficiency is independent of compression ratio.

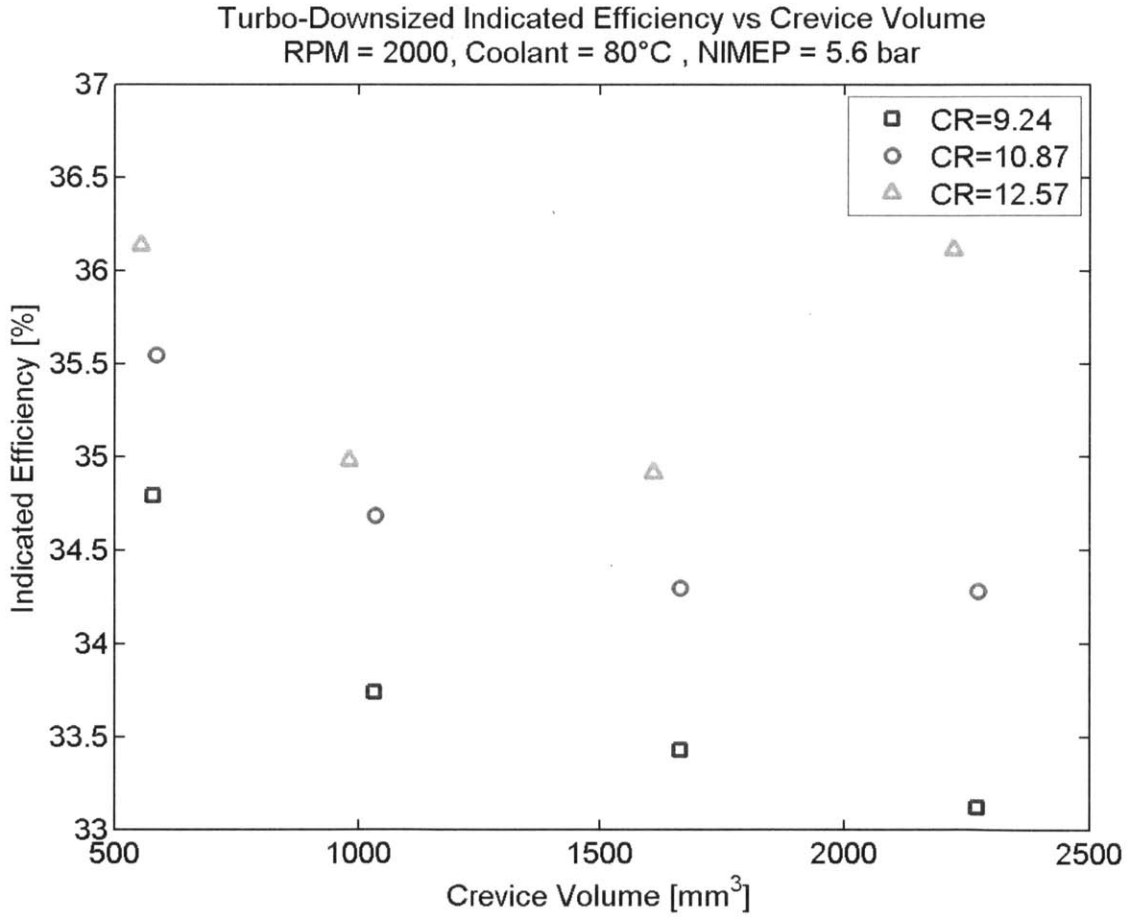

Figure 5-28 Indicated efficiency versus crevice volume for a speed of 2000 rpm, 80°C coolant temperature, and an NIMEP value of 5.6 bar at various compression ratios.

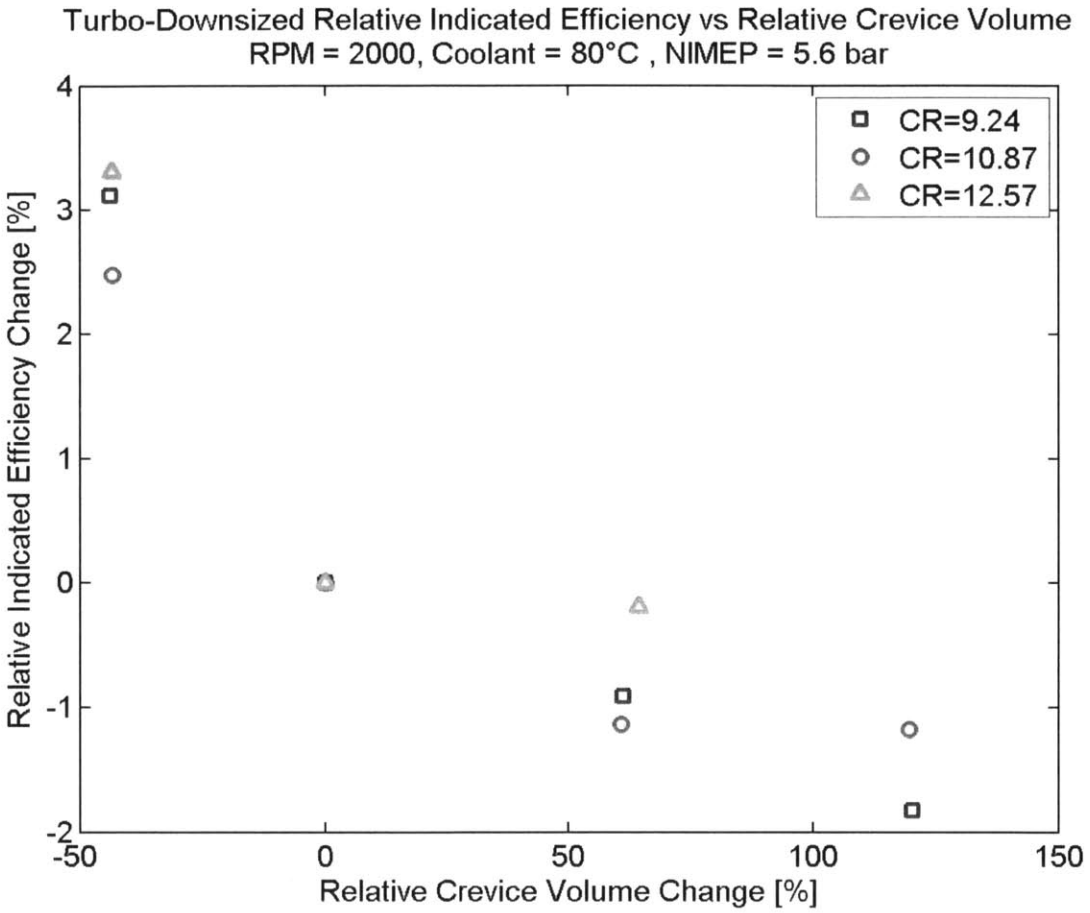

Figure 5-29 Relative indicated efficiency change versus relative crevice volume change for a speed of 2000 rpm, 80°C coolant temperature, and an NIMEP value of 5.6 bar at various compression ratios.

5.3.4 Blowby

Blowby differs with changing pressure time histories as compression ratio is varied in the engine setup. For the control piston modification at 2000 rpm, 80°C coolant temperature, and a MAP value of 0.6 bar blowby values are simulated with the piston-ring pack model for the three compression ratios studied. At a compression ratio of 9.24 the blowby value is found to be 6.04-5 kg/s; about 1.54% of the total flow. At a compression ratio of 10.87 the blowby value is found to be 6.94-5 kg/s; about 1.76% of the total flow. At a compression ratio of 12.57 the blowby value is found to be 7.62-5 kg/s; about 1.94% of the total flow. As compression ratio is increased pressures are increased, causing a larger fraction of total mass to escape the combustion chamber through blowby. This effect tends to reduce the efficiency increases seen from increasing compression ratio. In a real engine this blowby would be recycled and a slightly higher efficiency gain would be seen for a given compression ratio increase.

5.4 Effect of Engine Speed

5.4.1 Crevice Volume Effect on Efficiency

Three different speeds, 1500, 2000, and 2500 rpm, are investigated at each compression ratio. For a compression ratio of 9.24, 80°C coolant temperature, and an NIMEP value of 3.6 bar absolute efficiencies and crevice volumes are shown in Figure 5-30 and relative values are shown in Figure 5-31. At this compression ratio indicated efficiency values for the control, groove 1, and groove 2 piston crevice modifications for different engine speeds are all very close to each other. There is a little more spread when crevice volume is decreased to its lowest value, but this is still small compared to the magnitude of the relative changes shown in Figure 5-31. For this compression ratio, coolant temperature, and NIMEP value it can be said that the crevice effect on indicated efficiency is essentially independent of engine speed.

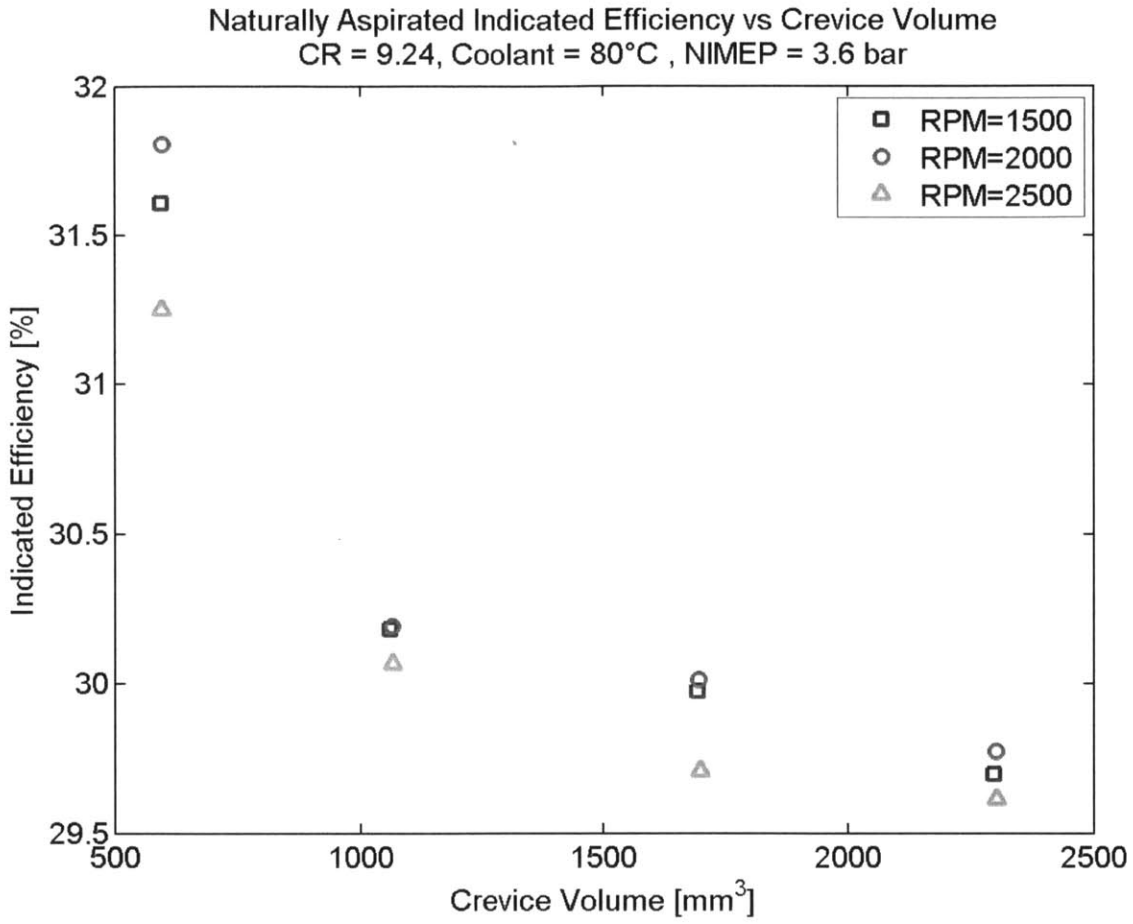

Figure 5-30 Indicated efficiency versus crevice volume for a compression ratio of 9.24, 80°C coolant temperature, and an NIMEP value of 3.6 bar at various speeds.

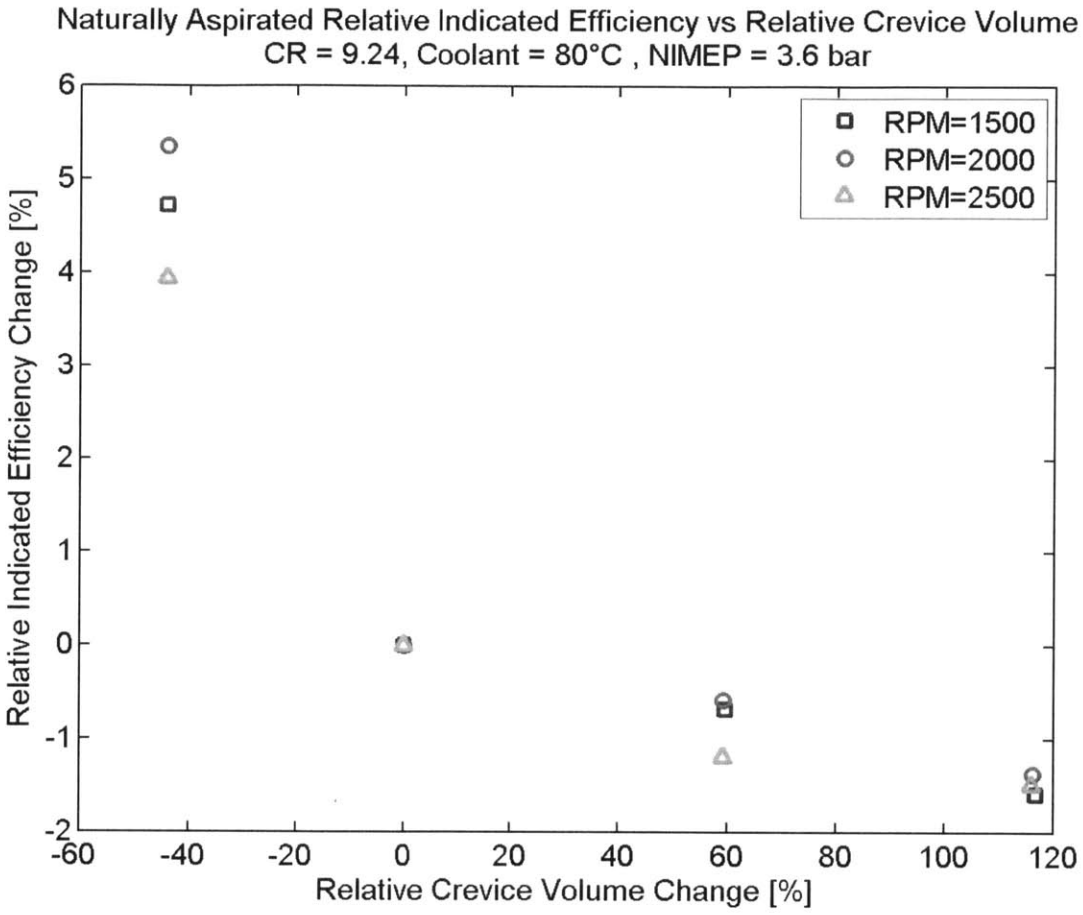

Figure 5-31 Relative indicated efficiency change versus relative crevice volume change for a compression ratio of 9.24, 80°C coolant temperature, and an NIMEP value of 3.6 bar at various speeds.

For a compression ratio of 10.87, 80°C coolant temperature, and an NIMEP value of 3.6 bar absolute efficiencies and crevice volumes are shown in Figure 5-32 and relative values are shown in Figure 5-33. Similar to the results for a compression ratio of 9.24 there is some spread in the values at the lowest crevice volume, but very little at all other crevice volumes. The relative changes in Figure 5-33 mostly collapse and so for this compression ratio, coolant temperature, and NIMEP value the crevice effect on indicated efficiency is essentially independent of engine speed.

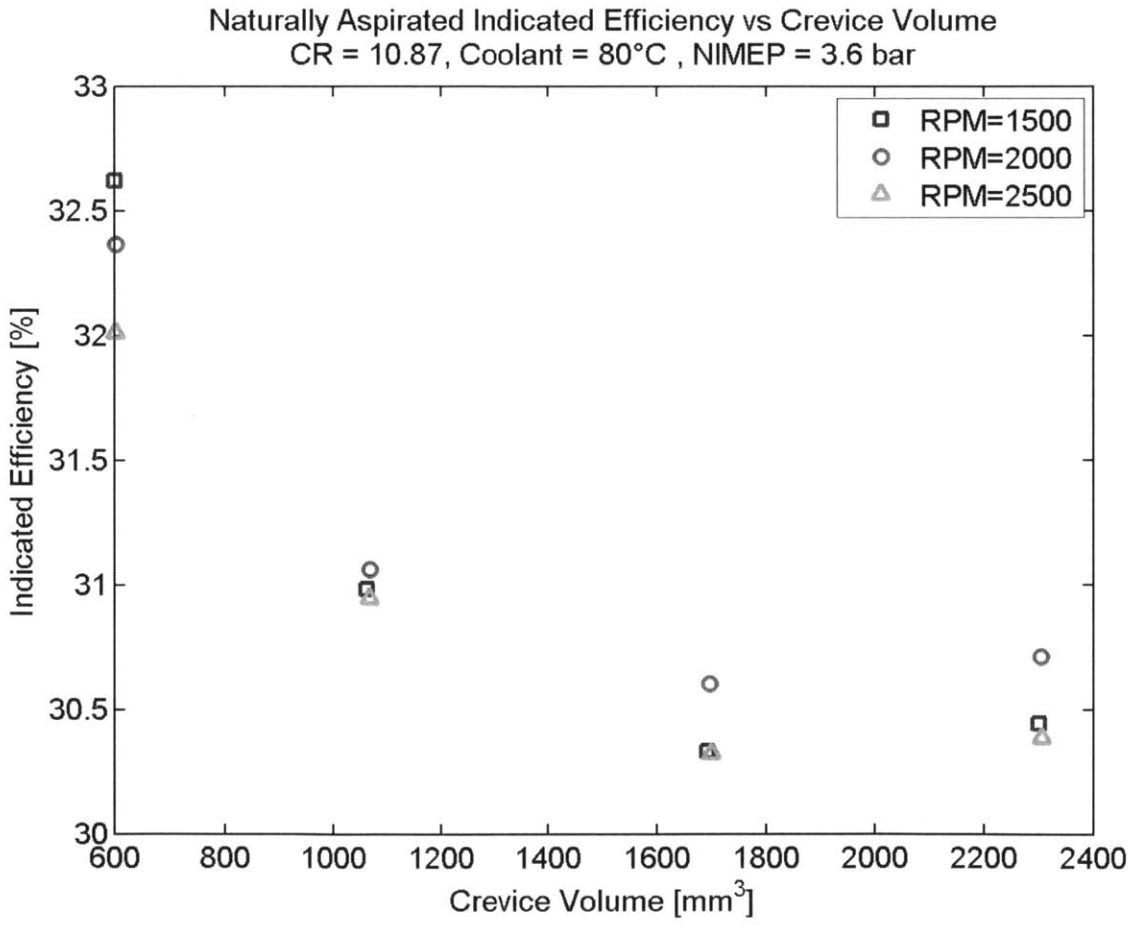

Figure 5-32 Indicated efficiency versus crevice volume for a compression ratio of 10.87, 80°C coolant temperature, and an NIMEP value of 3.6 bar at various speeds.

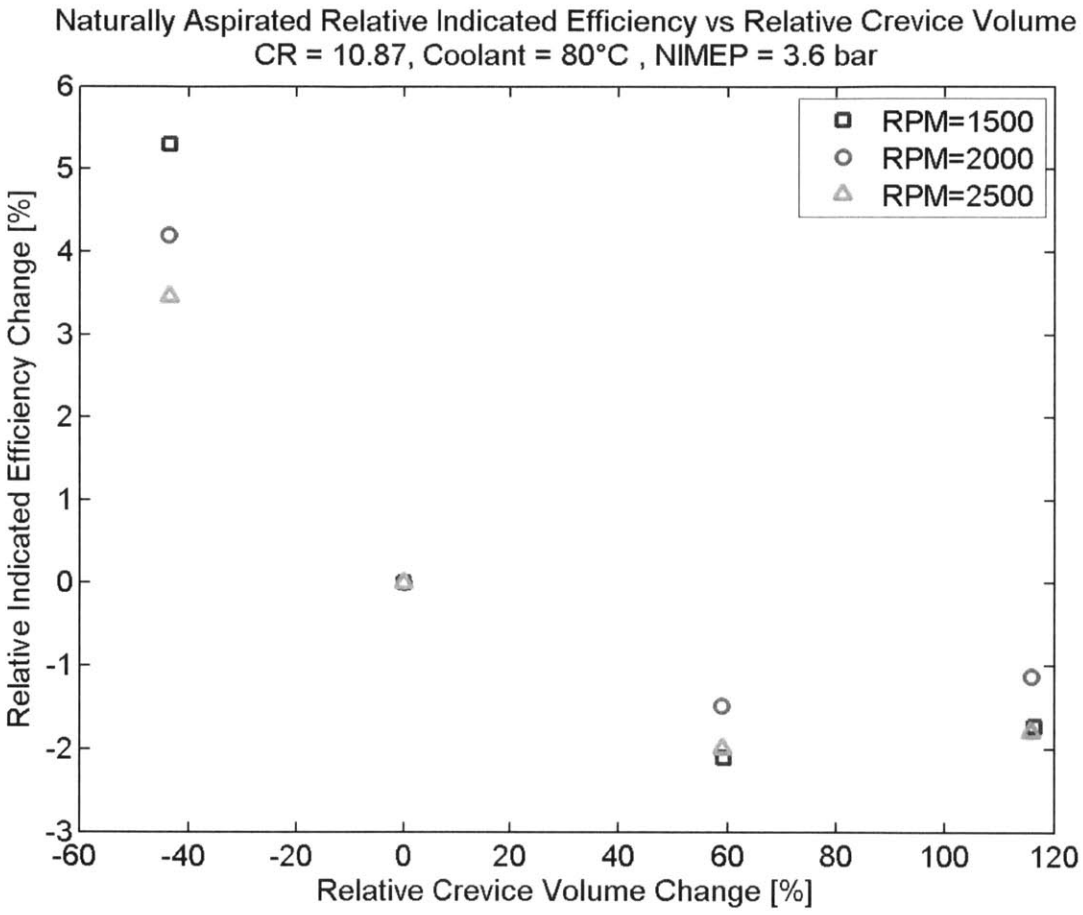

Figure 5-33 Relative indicated efficiency change versus relative crevice volume change for a compression ratio of 10.87, 80°C coolant temperature, and an NIMEP value of 3.6 bar at various speeds.

For a compression ratio of 12.57, 80°C coolant temperature, and an NIMEP value of 3.6 bar absolute efficiencies and crevice volumes are shown in Figure 5-34 and relative values are shown in Figure 5-35. Unlike the previous two compression ratios there is significant spread in the absolute efficiencies across engine speed at all of the crevice volumes. Interestingly, the relative changes shown in Figure 5-35 collapse across compression ratio. These two observations combine to show that for this compression ratio, coolant temperature, and NIMEP value the indicated efficiency is not independent of engine speed, but the crevice effect on indicated efficiency is independent of engine speed.

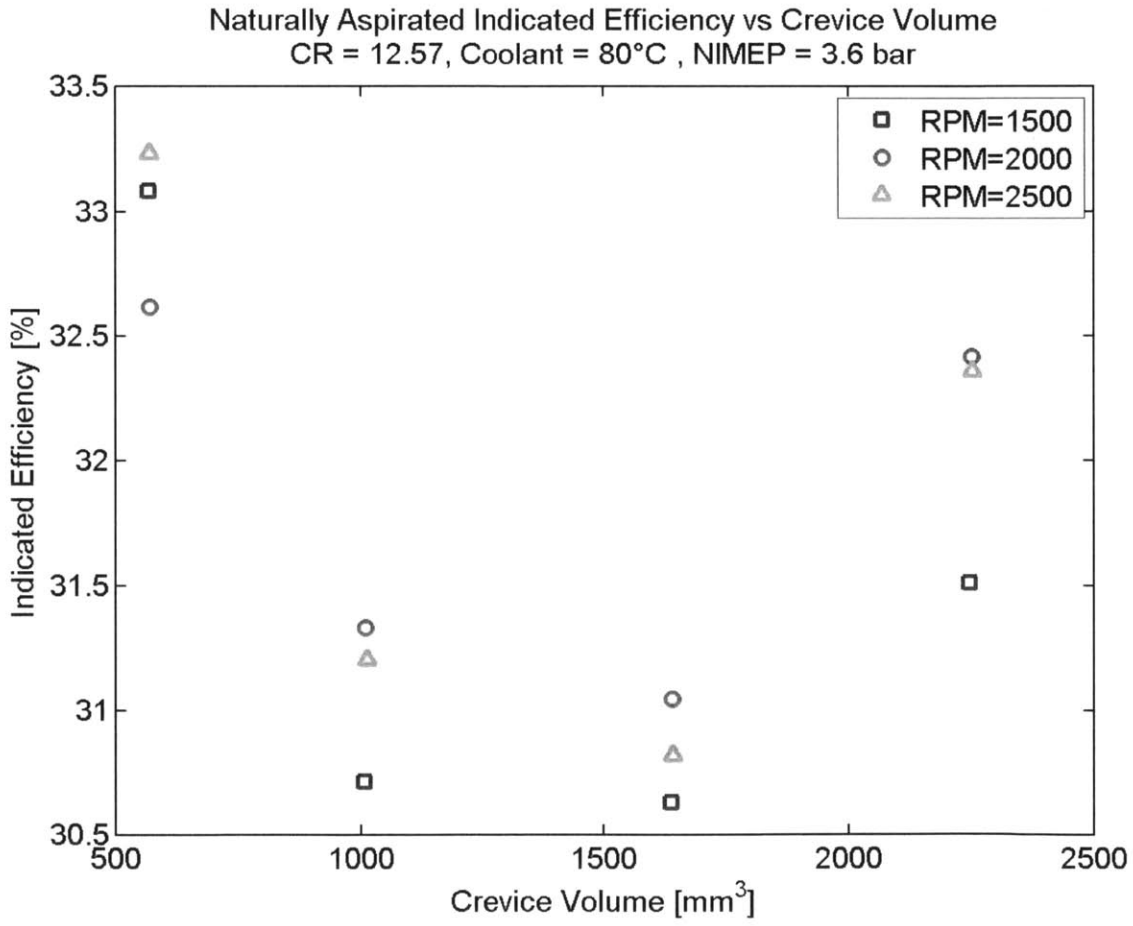

Figure 5-34 Indicated efficiency versus crevice volume for a compression ratio of 12.57, 80°C coolant temperature, and an NIMEP value of 3.6 bar at various speeds.

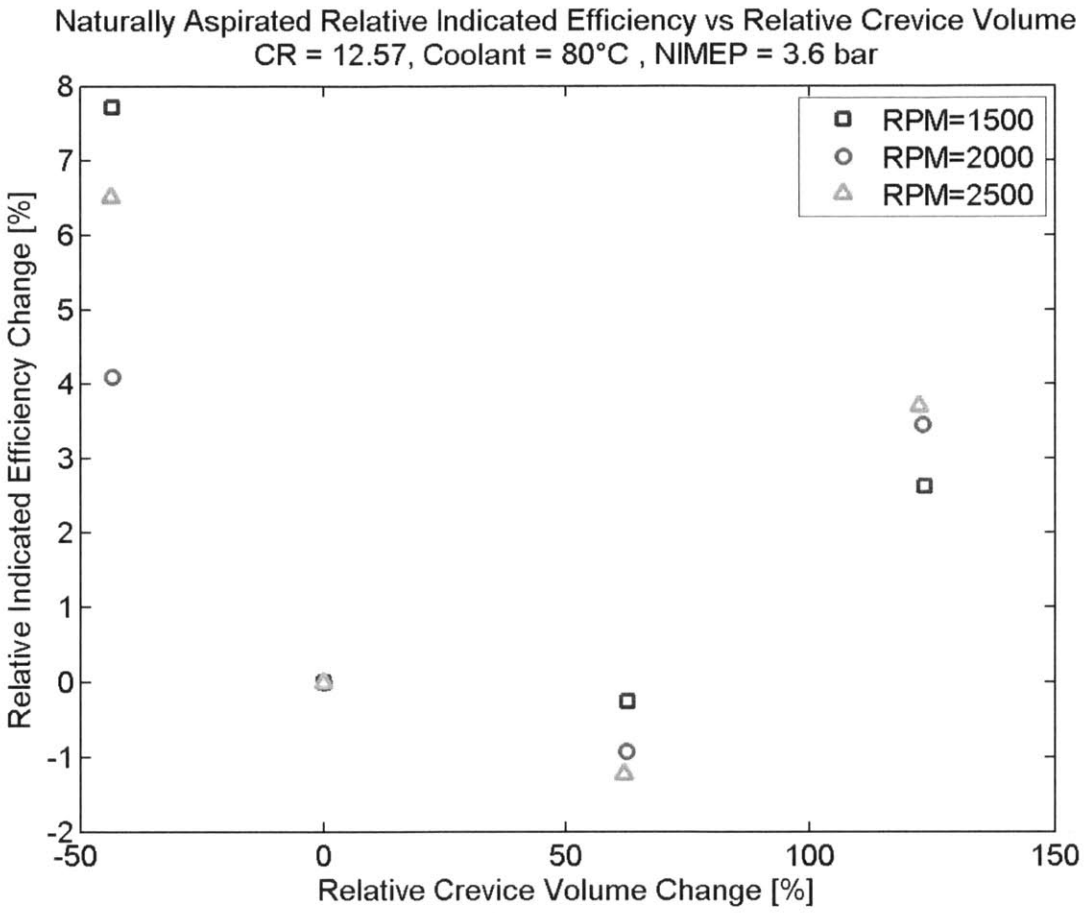

Figure 5-35 Relative indicated efficiency change versus relative crevice volume change for a compression ratio of 12.57, 80°C coolant temperature, and an NIMEP value of 3.6 bar at various speeds.

5.4.2 Blowby

Blowby changes across different engine speeds as engine cycle absolute time varies. For a compression ratio of 9.24 at the control piston modification, 80°C coolant temperature, and a MAP value of 0.6 bar blowby values are simulated with the piston-ring pack model for the three engine speeds investigated. At an engine speed of 1500 rpm the blowby value is found to be 6.03-5 kg/s; about 2.13% of the total flow. At an engine speed of 2000 rpm the blowby value is found to be 6.04-5 kg/s; about 1.54% of the total flow. At an engine speed of 2500 rpm the blowby value is found to be 6.55-5 kg/s; about 1.29% of the total flow. As engine speed is increased the blowby flow as a fraction of total flow decreases. This is because at higher speeds there is less time for gas to flow through the piston-ring pack. These changes are small and lead to changes in efficiency that are clouded by various other changes to efficiency from running at different engine speeds.

5.5 Effect of Coolant Temperature

5.5.1 Crevice Volume Effect on Efficiency

Two different coolant temperatures, 50°C and 80°C, are investigated at each compression ratio. For a compression ratio of 9.24, a speed of 2000 rpm, and an NIMEP value of 3.6 bar absolute efficiencies and crevice volumes are shown in Figure 5-36 and relative values are shown in Figure 5-37. For this case the two efficiency values for different coolant temperatures at the control, groove1, and groove 2 piston crevice modifications are close together. This is caused by similar quenching characteristics at the entrances to the piston crevice. Interestingly, for the new top land piston crevice modification the indicated efficiency at the reduced coolant temperature is much higher. This could be the result of the increased mass trapped in the crevice under cooler conditions, but this is very loosely concluded.

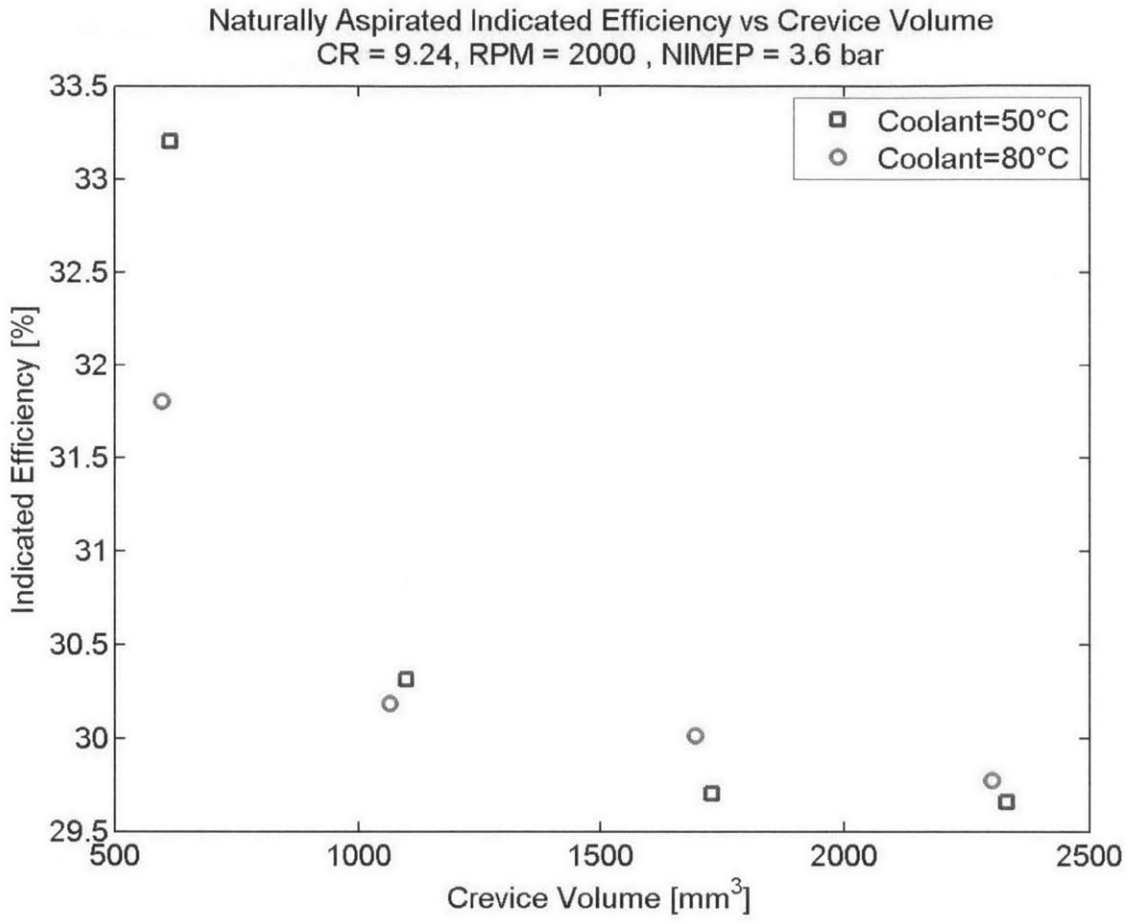

Figure 5-36 Indicated efficiency versus crevice volume for a compression ratio of 9.24, speed of 2000 rpm, and an NIMEP value of 3.6 bar at two coolant temperatures.

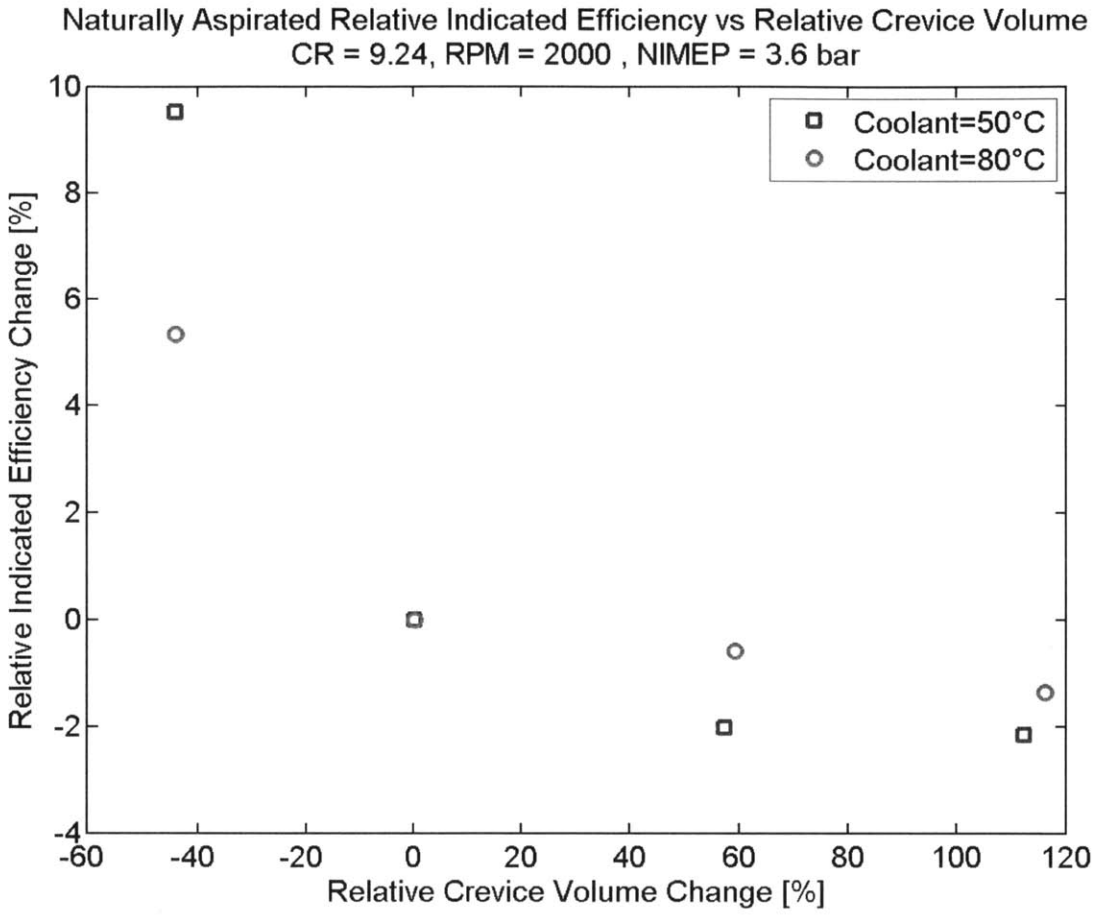

Figure 5-37 Relative indicated efficiency change versus relative crevice volume change for a compression ratio of 9.24, speed of 2000 rpm, and an NIMEP value of 3.6 bar at two coolant temperatures.

For a compression ratio of 12.57, a speed of 2000 rpm, and an NIMEP value of 3.6 bar absolute efficiencies and crevice volumes are shown in Figure 5-38 and relative values are shown in Figure 5-39. Again the two efficiency values at different coolant temperatures for the control, groove1, and groove 2 piston crevice modifications are close together, whereas the efficiency value at the new top land modification is much higher for the reduced coolant temperature.

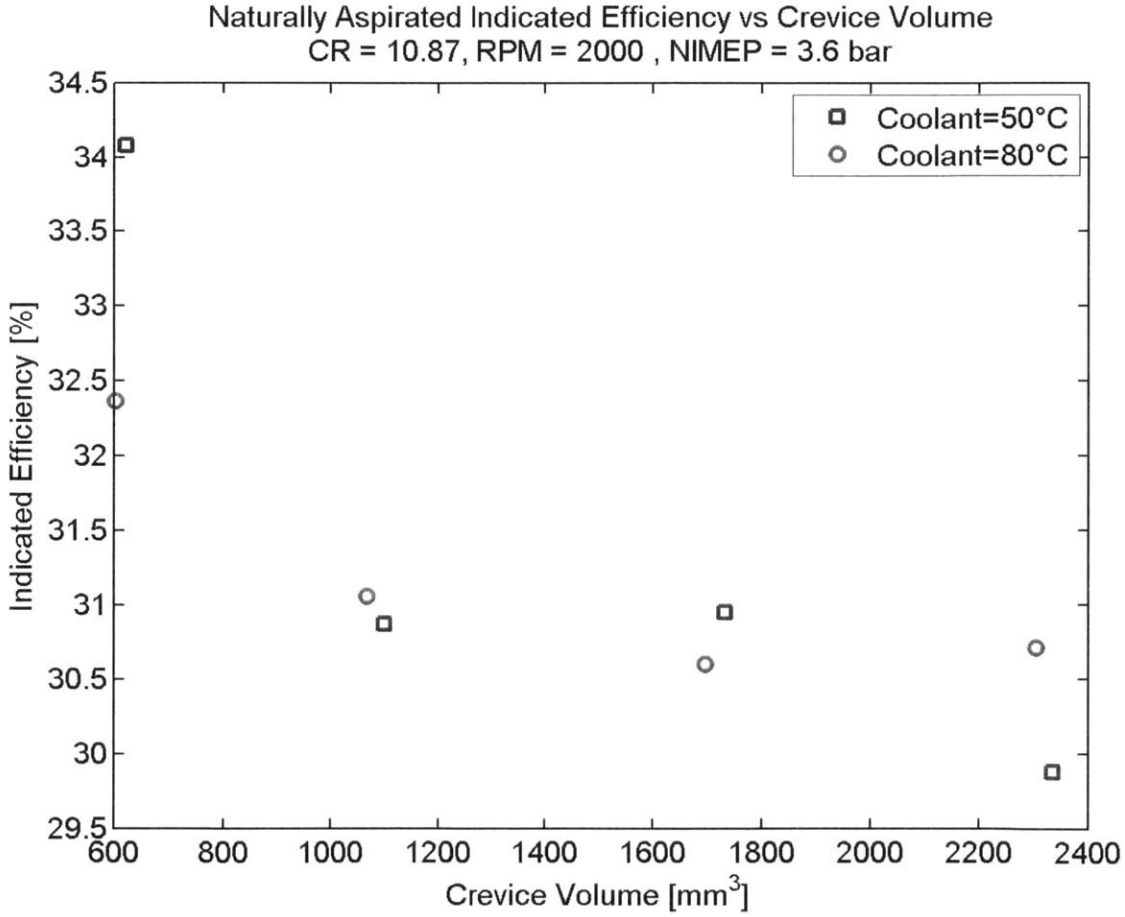

Figure 5-38 Indicated efficiency versus crevice volume for a compression ratio of 10.87, speed of 2000 rpm, and an NIMEP value of 3.6 bar at two coolant temperatures.

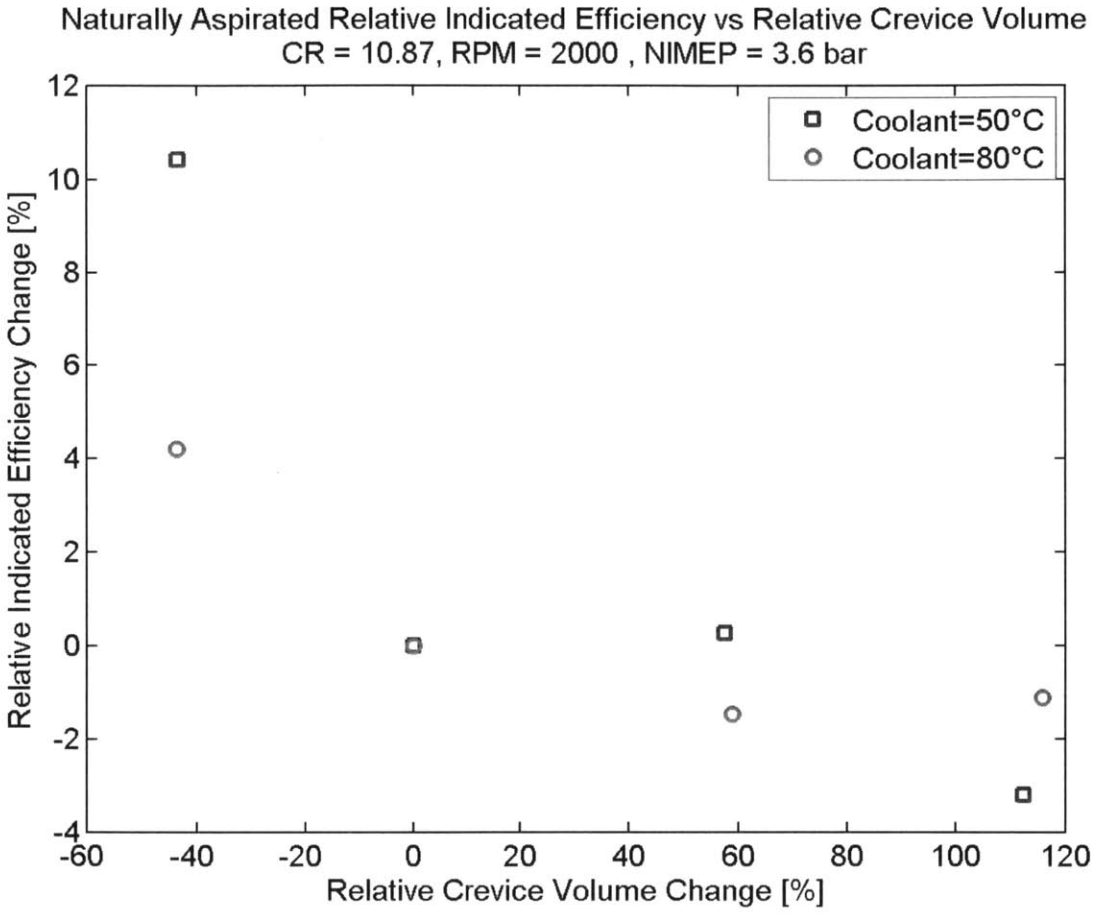

Figure 5-39 Relative indicated efficiency change versus relative crevice volume change for a compression ratio of 10.87, speed of 2000 rpm, and an NIMEP value of 3.6 bar at two coolant temperatures.

For a compression ratio of 12.57, a speed of 2000 rpm, and an NIMEP value of 3.6 bar absolute efficiencies and crevice volumes are shown in Figure 5-40 and relative values are shown in Figure 5-41. At this compression ratio the efficiencies are all over the place when comparing across coolant temperature. No explanation is readily available for this compression ratio case.

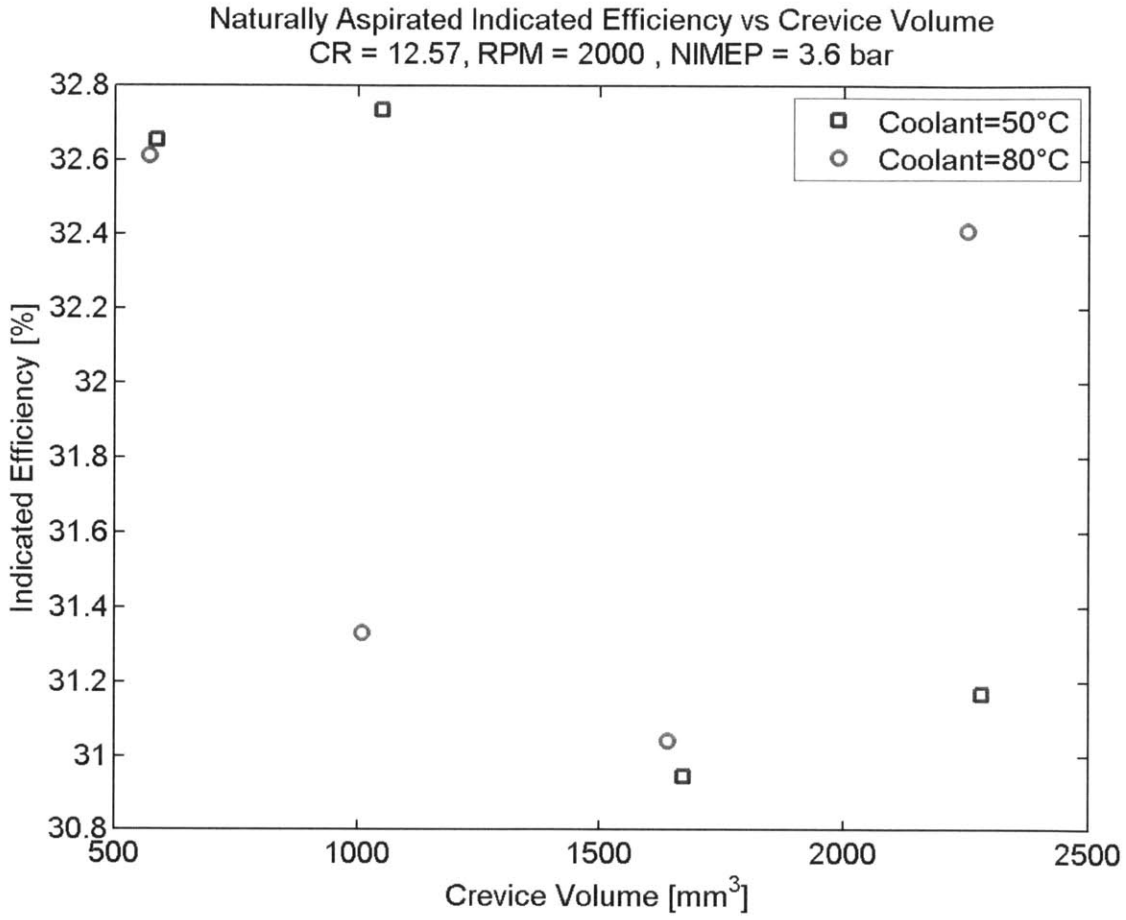

Figure 5-40 Indicated efficiency versus crevice volume for a compression ratio of 12.57, speed of 2000 rpm, and an NIMEP value of 3.6 bar at two coolant temperatures.

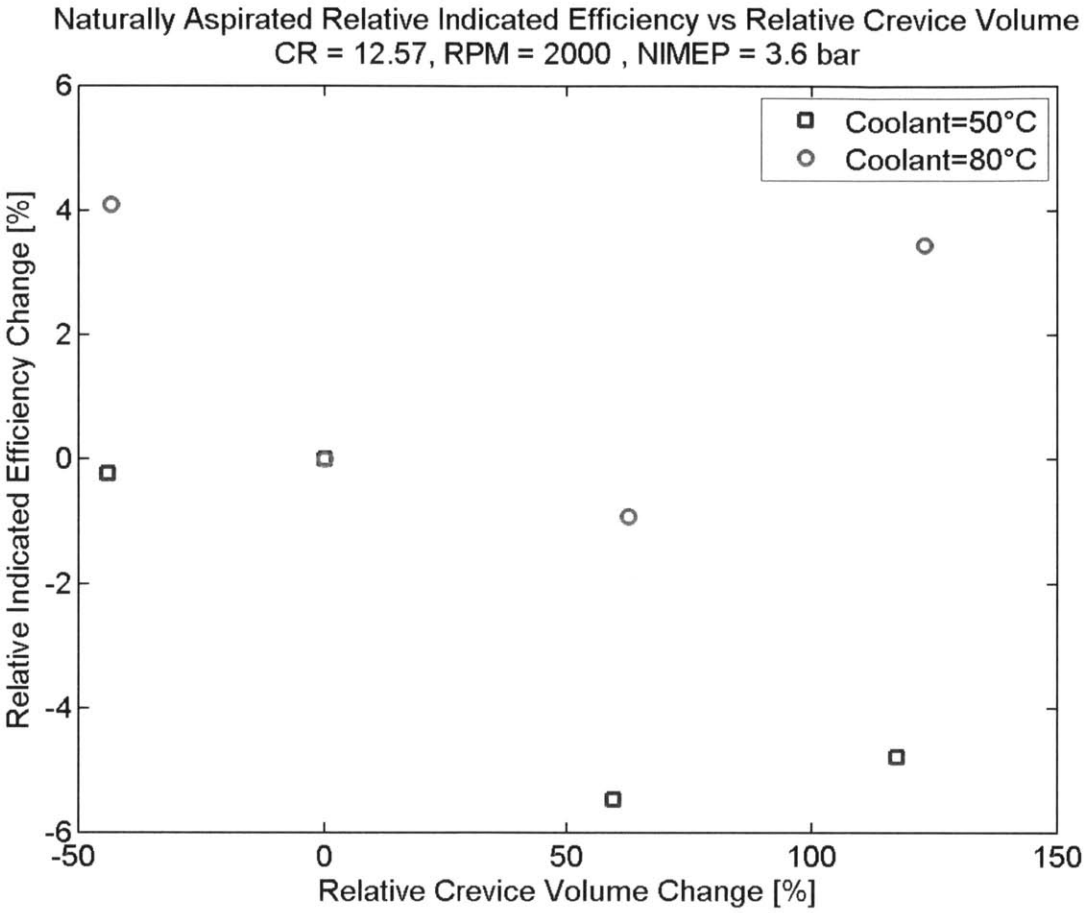

Figure 5-41 Relative indicated efficiency change versus relative crevice volume change for a compression ratio of 12.57, speed of 2000 rpm, and an NIMEP value of 3.6 bar at two coolant temperatures.

6 Conclusions

This experimental and simulation based study looks at the effects of altering piston crevice volume and compression ratio on indicated efficiency. These effects on efficiency are quantified on a broad basis using simulations, and with a more narrow focus using experiments on a single cylinder test engine.

6.1 Crevice Volume Effect on Efficiency

6.1.1 Simulation Study

Results from the simulation study compute crevice loss as a fraction of fuel energy for various displacement volumes and compression ratios. At the part load case, crevice losses range from 0.6 – 2.5% of the fuel energy. At the full load case, crevice losses range from 0.5 – 2.4% of the fuel energy. Crevice loss increases as displacement volume decreases and compression ratio increases. Losses are very similar across load because fuel mass trapped in the piston crevice as a fraction of total fuel mass is nearly constant. With engine downsizing crevice loss as a fraction of fuel energy drops by an absolute 0.5% per 100 cc reduction in displacement volume, and these changes are independent of compression ratio.

6.1.2 Baseline Case

Experimental results for the baseline case (compression ratio = 9.24, speed = 2000 rpm, coolant temperature = 80°C, MBT Timing) measure indicated efficiency changes across different piston crevice modifications and loads. Piston crevice volume is increased by cutting out a groove in the top land. For increased crevice volumes absolute indicated efficiency at the baseline conditions decreases by 0.3-0.5%-points per 1000 mm^3. These efficiency degradations correspond to 1.2-1.5% relative decreases for a 100% increase in crevice volume; referenced to the control piston crevice modification. Piston crevice volume is decreased by sliding the top ring closer to the piston crown. For decreased crevice volumes absolute indicated efficiency at the baseline conditions increases by 2.3-3.5%-points per 1000 mm^3. These efficiency improvements correspond to 6.9-11.8% relative increases for a 100% decrease in crevice

volume; referenced to the control piston crevice modification. An approximate theoretical analysis is completed to assess validity of experimental changes, which finds an expected absolute change in indicated efficiency of 1.2%-points per 1000 mm^3. Some degree of flame entrance into the piston crevice would act to shift the effective crevice volume to lower values. This could cause the difference between the theoretical and experimental slopes.

Due to high peak pressures and low crevice temperatures, there is significant mass trapped in the piston crevice at the various piston crevice volumes tested; 5-20% of total charge mass. The approximation of flame arrival at the piston crevice coinciding with peak pressure is shown to be a reasonable assumption based on 90% mass burned fractions.

6.1.3 Across Compression Ratio

Based on simulation study results the crevice effect on absolute efficiency is expected to change by about 0.1%-points of fuel energy per 1 unit of compression ratio increase. At experimental conditions and uncertainties this is far too small of a change to notice. Experimental results show that the crevice volume effect on efficiency is essentially independent of compression ratio for the conditions tested.

6.1.4 Across Engine Speed

At three different engine speeds (1500, 2000, and 2500 rpm) relative changes in indicated efficiency collapse for all piston crevice modifications at each compression ratio. This shows that the crevice effect on efficiency is roughly independent of engine speed at the conditions tested.

6.1.5 Across Coolant Temperature

For the lower compression ratios most indicated efficiency values are close together across coolant temperatures. At these cases piston quenching remains similar even though piston and liner expansion change. These changes, along with changes in quenching behavior of the bulk gas, cancel out most efficiency changes of the crevice effect from altering coolant temperature. At the new top modification efficiency gains from reducing the crevice volume are significantly higher at the lower coolant temperature. This could be the result of the increased mass trapped in the crevice under cooler conditions, but the full reason for this change is not currently clear.

6.2 Compression Ratio Effect on Efficiency

6.2.1 Simulation Study

Simulation study results for brake efficiencies are available for compression ratios ranging from 8 to 20 at part and full load. Diminishing returns are seen as compression ratio is increased from 8 to 20, with about a 2%-point absolute increase from 8 to 12 and a 0.5%-point absolute increase from 16 to 20, at the part load condition. Larger changes are seen at the full load condition; about a 3.5%-point absolute increase from 8 to 12 and a 1.5%-point absolute increase from 16 to 20. For both of the load conditions this gain with increased compression ratio is nearly independent of displacement volume.

6.2.2 Experimental Results

Experimental results for indicated efficiencies are measured at three compression ratios (9.24, 10.87, and 12.57) for the control piston crevice modification at a speed of 2000 rpm and coolant temperature of 80°C. Two load points (NIMEP = 3.6, 5.6 bar) are isolated and show nearly identical absolute and relative efficiency trends with changing compression ratio. There is again a diminishing return as compression ratio is increased, with a 1% absolute gain in indicated efficiency when going from 9.24 to 10.87, and only a 0.3% absolute gain in indicated efficiency when going from 10.87 to 12.57.

6.3 Application to Engine Design

These results have strong implications in future piston design focusing on maximum efficiency, while maintaining piston performance and durability.

6.3.1 New Top Land Height

When designing new pistons to take advantage of the efficiency increase from decreased piston crevice volume, it is important to note which geometric parameters are most readily altered. Piston-liner clearances in modern engines are very tightly controlled based on thermal expansion considerations, and are currently set to minimum safe values. This leaves the top land

height as the preferred parameter to change in order to realize smaller piston crevice volumes. Reducing the top land height brings the top ring closer to the combustion chamber, and reduces the axial strength of the piston crown near the edges. These effects must be quantified in deciding a new piston top land height for improved efficiency.

6.3.2 Piston and Top Ring Concerns

Piston durability is arguably the most important consideration in piston design. Piston crowns are exposed to the highest pressures and temperatures, and thus must be strong enough to resist fracture and thermal degradation. New materials and cooling concepts will have to be investigated to ensure piston durability, while allowing for this increase in efficiency from a reduced top land height.

Another challenge in reducing top land height is that of the top ring temperature. When the top ring is moved closer to the combustion chamber it will increase in temperature, and possibly degrade lubrication performance. This effect must be quantified and mitigated if efficiency gains are to be realized.

6.3.3 Increased Importance in Future Engines

Results of the simulation study in particular show the greater importance piston crevice loss will play as modern engines shift to turbo-downsized concepts. The crevice volume effect on efficiency increases in magnitude as displacement volume decreases. Larger engines will continue to be replaced by smaller turbocharged counterparts to meet efficiency standards, leading to higher piston crevice losses.

Experimental results are unable to discern any differences in the crevice volume effect on efficiency across compression ratios, but the simulation study shows that there will be higher losses due to the crevice at higher compression ratios. Better knock resistant engine concepts and fuels will lead to higher compression ratios being used in the future. This will only lead to greater importance of the piston crevice in regards to efficiency.

Appendix A: Two-Plate Quench Distance

Two-plate quench distance is the minimum gap between two large parallel plates that allows a flame to travel. In engines this value can be directly applied to quenching at the entrance to the piston crevice by using in-cylinder conditions and geometry. Two plate quench distances are analyzed by relating heat release in the flame to heat losses to the walls, unburned mixture, and burned mixture. This analysis leads to the Peclet number, which can then be used in Equation A.1 to find quench distances:

$$d_{q,2} = \frac{Pe_2 k_f}{\rho_u S_L c_{p,f}} \qquad [A.1]$$

where $d_{q,2}$ is the two-plate quench distance, Pe_2 is the Peclet number, k_f is the thermal conductivity at flame conditions, ρ_u is the unburned gas density, S_L is the laminar flame speed, and $c_{p,f}$ is the specific heat at constant pressure at flame conditions. Lavoie has run experiments using propane to suggest the correlation for Peclet numbers shown in Equation A.2 [19]:

$$Pe_2 = \frac{9.5}{\varphi}\left(\frac{p}{3}\right)^{.26*\min(1,1/\varphi^2)} \qquad [A.2]$$

where φ is the fuel/air equivalence ratio, and p is the in-cylinder pressure in atmosphere. To find quench distances at engine operating conditions additional information needs to be attained about unburned gas and flame properties.

A.1 Gas Properties

To find the unburned gas density the ideal gas law is used in Equation A.3:

$$\rho_u = \frac{p * M_u}{\bar{R} * T_u} \qquad [A.3]$$

where p is the in-cylinder pressure, M_u is the molecular weight of unburned gas, $\bar{R}$ is the universal gas constant, and T_u is unburned gas temperature. Pressure can be obtained directly from experiments, unburned temperature can be found from component temperature estimates, and the unburned gas molecular weight can be found by balancing chemical equations resulting in Equation A.4 to A.7:

$$M_u = \frac{m_{RP}}{n_u} \quad [A.4]$$

$$m_{RP} = 32 + 4\varphi(1 + 2\varepsilon) + 28.16\psi \quad [A.5]$$

$$n_u = (1 - x_r)\left[\frac{4(1 + 2\varepsilon)\varphi}{M_f} + 1 + \psi\right] + \tilde{x}_r n_b \quad [A.6]$$

$$n_b = (1 - \varepsilon)\varphi + 1 + \psi \quad [A.7]$$

where m_{RP} is total mass of mixture, n_u is moles of unburned mixture, n_b is moles of burned mixture, φ is fuel/air equivalence ratio, $\varepsilon = 4/(4 + molar\ H/C\ ratio\ of\ fuel)$, ψ is the molar N/O ratio, and $\tilde{x}_r$ is the molar residual fraction.

The ratio of thermal conductivity to specific heat at constant pressure for the flame condition can be found using Equation A.8:

$$\frac{k_f}{c_{p,f}} = \frac{\mu_f}{Pr_f} \quad [A.8]$$

where k_f is the thermal conductivity, $c_{p,f}$ is the specific heat at constant pressure, μ_f is the absolute viscosity, and Pr_f is the Prandtl number, all at flame conditions. Absolute viscosity has been correlated for engines based on equivalence ratio and temperature, as shown in Equation A.9 and A.10 [22,23]:

$$\mu_f = \frac{\mu_{air}}{1 + 0.027\varphi} \quad [A.9]$$

$$\mu_{air} = 3.3x10^{-7} * T^{0.7} \quad [A.10]$$

where μ_f is absolute viscosity at flame conditions, μ_{air} is absolute viscosity for air, and T is in-cylinder temperature. Prandtl number at flame conditions can be calculated based on the ratio of specific heats shown in Equation A.11 [22,23]:

$$Pr_f = 0.05 + 4.2(\gamma - 1) - 6.7(\gamma - 1)^2 \quad [A.11]$$

where Pr_f is the Prandtl number at flame conditions and γ is the ratio of specific heats. Specific heat ratios have previously been calculated and are reproduced in Figure A-1 for different equivalence ratios and temperatures [22,23].

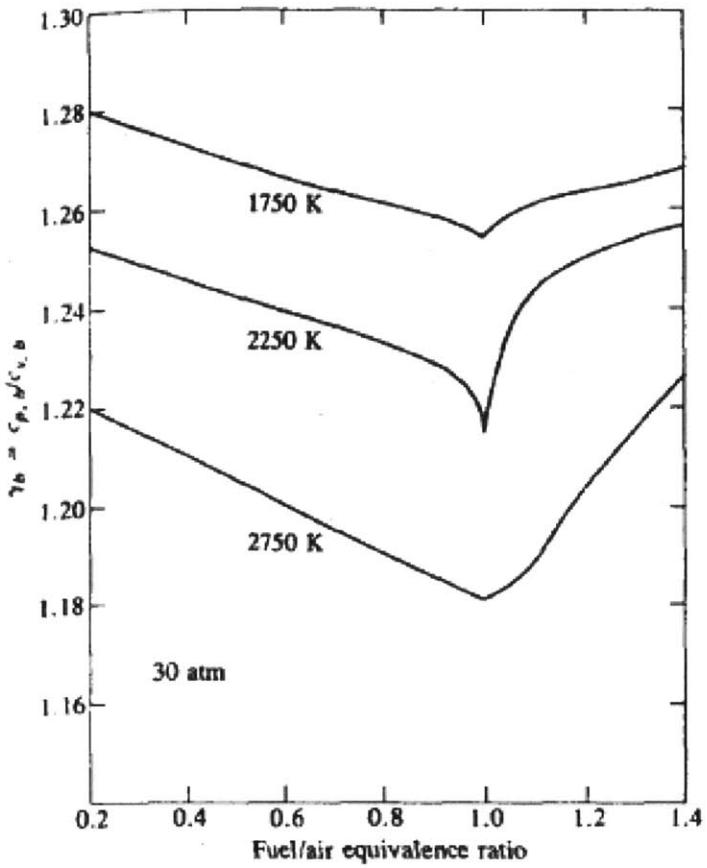

Figure A-1 Burned gas ratio of specific heats versus fuel/air equivalence ratio for various temperatures [22,23].

A.2 Laminar Flame Speed

Laminar flame speed is an important parameter in combustion research and has thusly been studied extensively. With regard to engine research, data at high pressures and temperatures fit well to the power law displayed in Equation A.12:

$$S_L = S_{L,0}\left(\frac{T_u}{T_0}\right)^{\alpha}\left(\frac{p}{p_0}\right)^{\beta} \qquad [A.12]$$

where $S_{L,0}$ is laminar flame speed at standard conditions, T_u is unburned gas temperature, p is in-cylinder pressure, T_0 is the standard temperature, p_0 is the standard pressure, and α and β are

constants. Experiments have been conducted on gasoline to correlate values for $S_{L,0}$ [21], α and β [20]; these correlations are shown in Equation A.13 to A.15.

$$S_{L,0} = B_m + B_\varphi(\varphi - \varphi_m)^2 \quad [A.13]$$

$$\alpha_g = 2.4 - 0.27\varphi^{3.51} \quad [A.14]$$

$$\beta_g = -0.357 + 0.14\varphi^{2.77} \quad [A.15]$$

where $S_{L,0}$ is laminar flame speed at standard conditions, φ is fuel/air equivalence ratio, and B_m, B_φ, and φ_m are constants. B_m, B_φ, and φ_m are found through experimental correlations to be $B_m = 0.305\ m/s$, $B_\varphi = -0.549\ m/s$, and $\varphi_m = 1.21$ [21].

Residual gas can have a large effect on laminar burning velocity, which is captured by the correlation shown in Equation A.16 [20]:

$$S_L(\tilde{x}_b) = S_L(\tilde{x}_b = 0)\left(1 - 2.06\tilde{x}_b{}^{0.77}\right) \quad [A.16]$$

where $S_L(\tilde{x}_b)$ is the laminar flame speed at a given burned gas fraction, $S_L(\tilde{x}_b = 0)$ is the laminar flame speed without burned gas, and $\tilde{x}_b$ is the molar burned gas fraction.

This page intentionally left blank

Appendix B: Orifice Flow

Fluid flow through a restriction occurs often in engines and can be related to ideal flow situations. This is normally done through experimentation to find a discharge coefficient, C_D. Liquids and gases flow differently through a restriction and both are presented here.

B.1 Liquid Flow

Combining Bernoulli's equation with the mass continuity equation for an incompressible substance Equation B.1 is formulated for an ideal liquid flow through an orifice:

$$\dot{m}_{ideal} = A_2 \left[\frac{2\rho(p_1 - p_2)}{1 - (A_2/A_1)^2} \right]^{1/2} \quad [B.1]$$

where $\dot{m}_{ideal}$ is the ideal mass flow rate, A_1 is the cross sectional area immediately upstream of the orifice, A_2 is the cross sectional area immediately downstream of the orifice, ρ is density, p_1 is pressure immediately upstream of the orifice, and p_2 is pressure immediately downstream of the orifice. The real mass flow rate is calculated by introducing the discharge coefficient, C_D, creating Equation B.2:

$$\dot{m}_{real} = C_D A_2 \left[\frac{2\rho(p_1 - p_2)}{1 - (A_2/A_1)^2} \right]^{1/2} \quad [B.2]$$

where $\dot{m}_{real}$ is the real mass flow rate and C_D is the discharge coefficient. This equation can then be rearranged to isolate components associated with a particular orifice geometry and fluid combination. These variables are contained in the first set of brackets in Equation B.3 and can be experimentally determined. It is important to note that the discharge coefficient can change slightly with mass flow rate and fluid properties.

$$\dot{m}_{real} = \left[\frac{2(C_D A_2)^2}{1 - (A_2/A_1)^2} \right]^{1/2} * [\rho(p_1 - p_2)]^{1/2} \quad [B.3]$$

B.2 Gas Flow

Gas flow through an orifice can be ideally represented as an isentropic flow with constant stagnation temperature and pressure. The steady flow energy equation and isentropic relation for temperature and pressure changes can then be combined to find the relations for pressure and temperature shown in Equation B.4 and B.5:

$$\frac{T_0}{T} = 1 + \frac{\gamma - 1}{2} M^2 \qquad [B.4]$$

$$\frac{p_0}{p} = \left(1 + \frac{\gamma - 1}{2} M^2\right)^{\gamma/(\gamma-1)} \qquad [B.5]$$

where T_0 is stagnation temperature, T is static temperature, p_0 is stagnation pressure, p is static pressure, γ is the ratio of specific heats, and M is Mach number. These relations can then be combined with the mass flow rate ($\dot{m} = \rho A V$), ideal gas law ($p = \rho R T$), and Mach number definition ($M = V/a \ , \ a = \sqrt{\gamma R T}$) to find Equation B.6 for the ideal mass flow rate:

$$\dot{m}_{ideal} = \frac{A_T p_0}{(R T_0)^{1/2}} \left(\frac{p_T}{p_0}\right)^{1/\gamma} \left\{\frac{2\gamma}{\gamma - 1}\left[1 - \left(\frac{p_T}{p_0}\right)^{(\gamma-1)/\gamma}\right]\right\}^{1/2} \qquad [B.6]$$

where $\dot{m}_{ideal}$ is the ideal mass flow rate, A_T is throat area, p_0 is stagnation pressure, R is the specific gas constant, T_0 is stagnation temperature, p_T is throat pressure, and γ is the ratio of specific heats. When the flow velocity at the throat equals the speed of sound the flow is said to be choked. For this condition only raising the stagnation pressure or temperature upstream can increase the flow rate. A flow will be in this choked condition if the ratio of throat pressure to upstream stagnation pressure satisfies Equation B.7:

$$\frac{p_T}{p_0} \leq [2/(\gamma + 1)]^{\gamma/(\gamma-1)} \qquad [B.7]$$

where p_T is throat pressure, p_0 is stagnation pressure, and γ is the ratio of specific heats.

When the flow is choked the ideal mass flow rate reduces to Equation B.8:

$$\dot{m}_{ideal} = \frac{A_T p_0}{(RT_0)^{1/2}} \gamma^{1/2} \left(\frac{2}{\gamma+1}\right)^{(\gamma+1)/2(\gamma-1)} \quad [B.8]$$

where $\dot{m}_{ideal}$ is the ideal mass flow rate, A_T is throat area, p_0 is stagnation pressure, R is the specific gas constant, T_0 is stagnation temperature, and γ is the ratio of specific heats. To convert to real flow rates a discharge coefficient is introduced. For a sub-critical, non-choked flow the real mass flow rate of a gas through an orifice is given by Equation B.9, and for a choked flow by Equation B.10:

$$\dot{m}_{real} = \frac{C_D A_T p_0}{(RT_0)^{1/2}} \left(\frac{p_T}{p_0}\right)^{1/\gamma} \left\{\frac{2\gamma}{\gamma-1}\left[1 - \left(\frac{p_T}{p_0}\right)^{(\gamma-1)/\gamma}\right]\right\}^{1/2} \quad [B.9]$$

$$\dot{m}_{real} = \frac{C_D A_R p_0}{(RT_0)^{1/2}} \gamma^{1/2} \left(\frac{2}{\gamma+1}\right)^{(\gamma+1)/2(\gamma-1)} \quad [B.10]$$

where $\dot{m}_{real}$ is the ideal mass flow rate, A_T is throat area, p_0 is stagnation pressure, R is the specific gas constant, T_0 is stagnation temperature, p_T is throat pressure, and γ is the ratio of specific heats.

This page intentionally left blank

Appendix C: Additional Plots across Speed

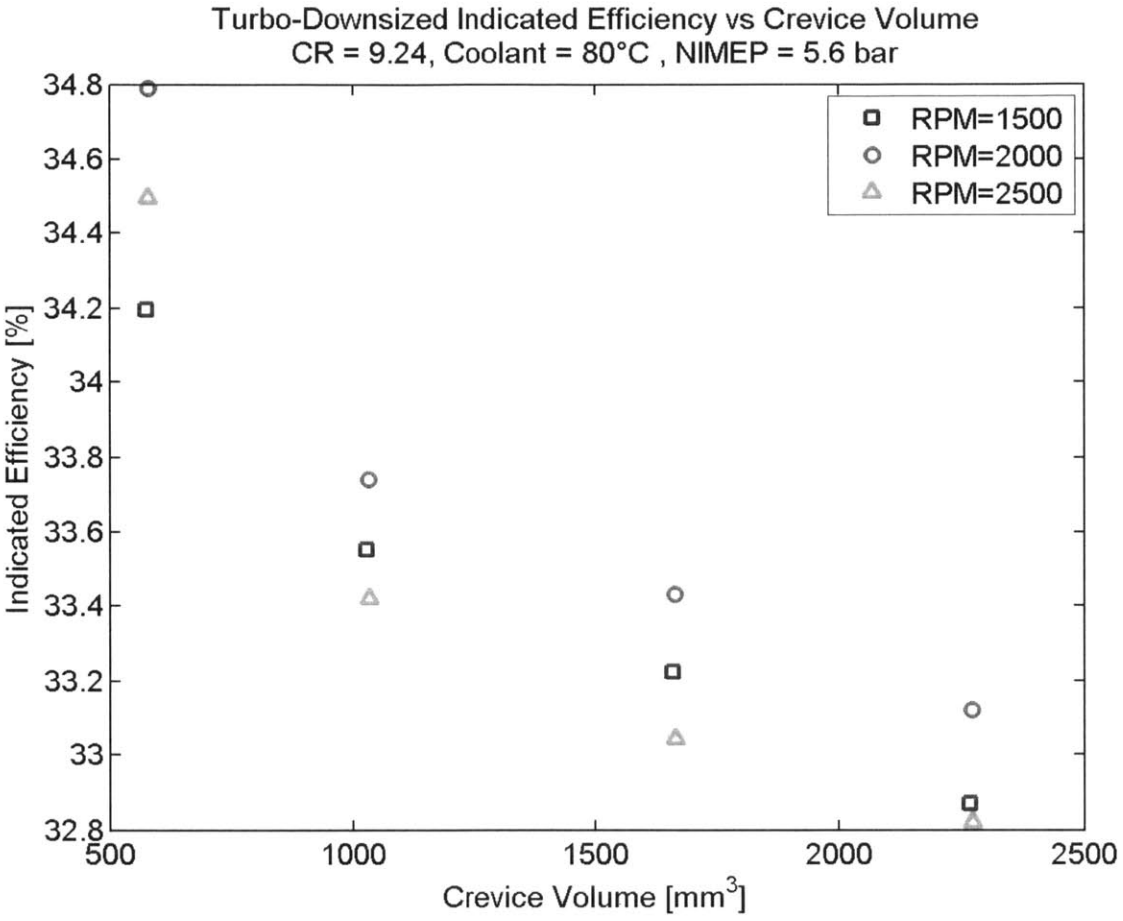

Figure C-1 Indicated efficiency versus crevice volume for a compression ratio of 9.24, 80°C coolant temperature, and an NIMEP value of 5.6 bar at various speeds.

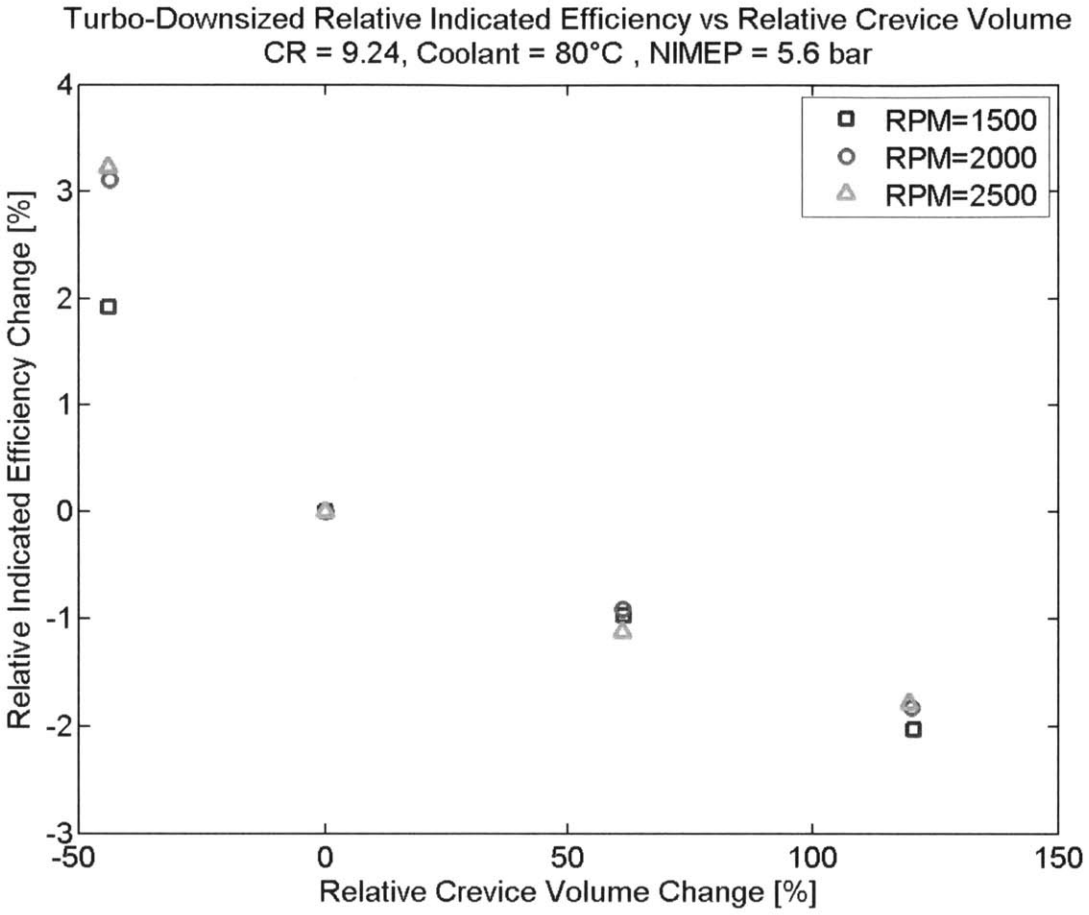

Figure C-2 Relative indicated efficiency change versus relative crevice volume change for a compression ratio of 9.24, 80°C coolant temperature, and an NIMEP value of 5.6 bar at various speeds.

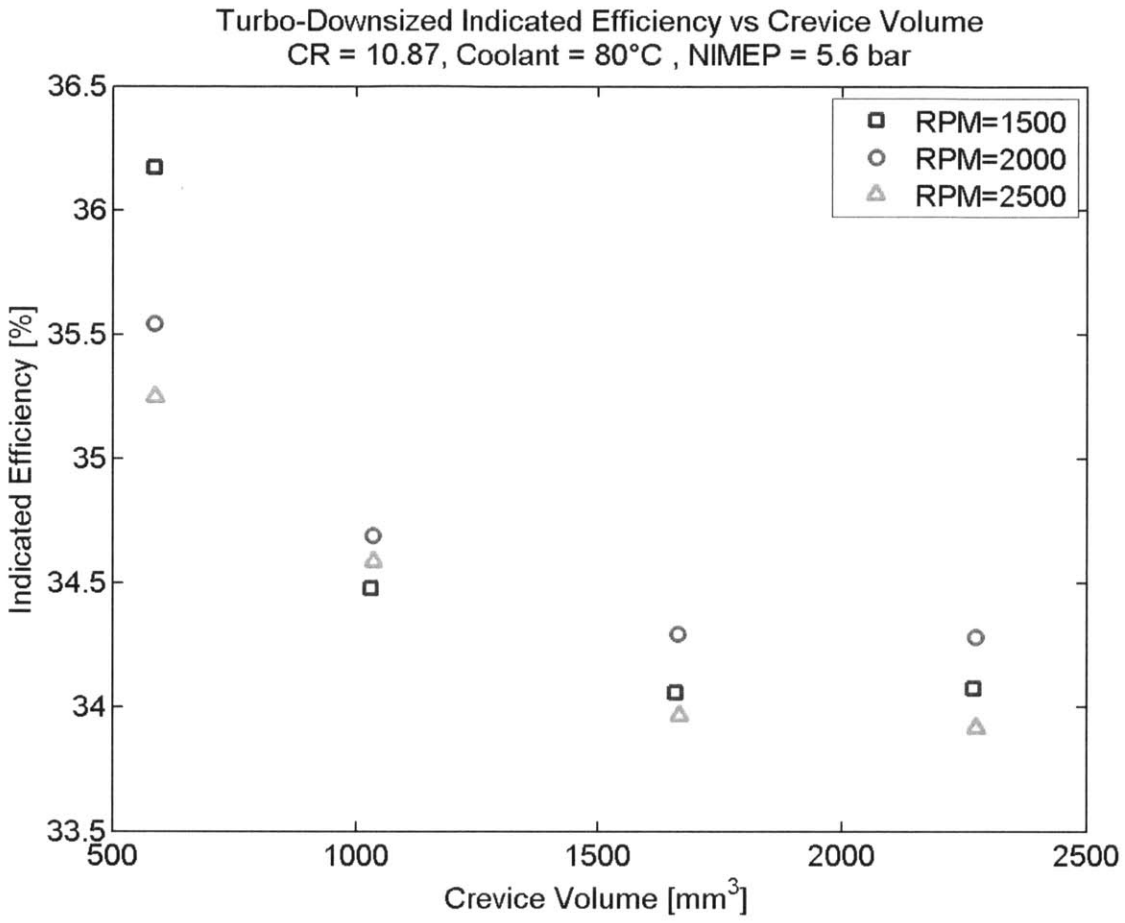

Figure C-3 Indicated efficiency versus crevice volume for a compression ratio of 10.87, 80°C coolant temperature, and an NIMEP value of 5.6 bar at various speeds.

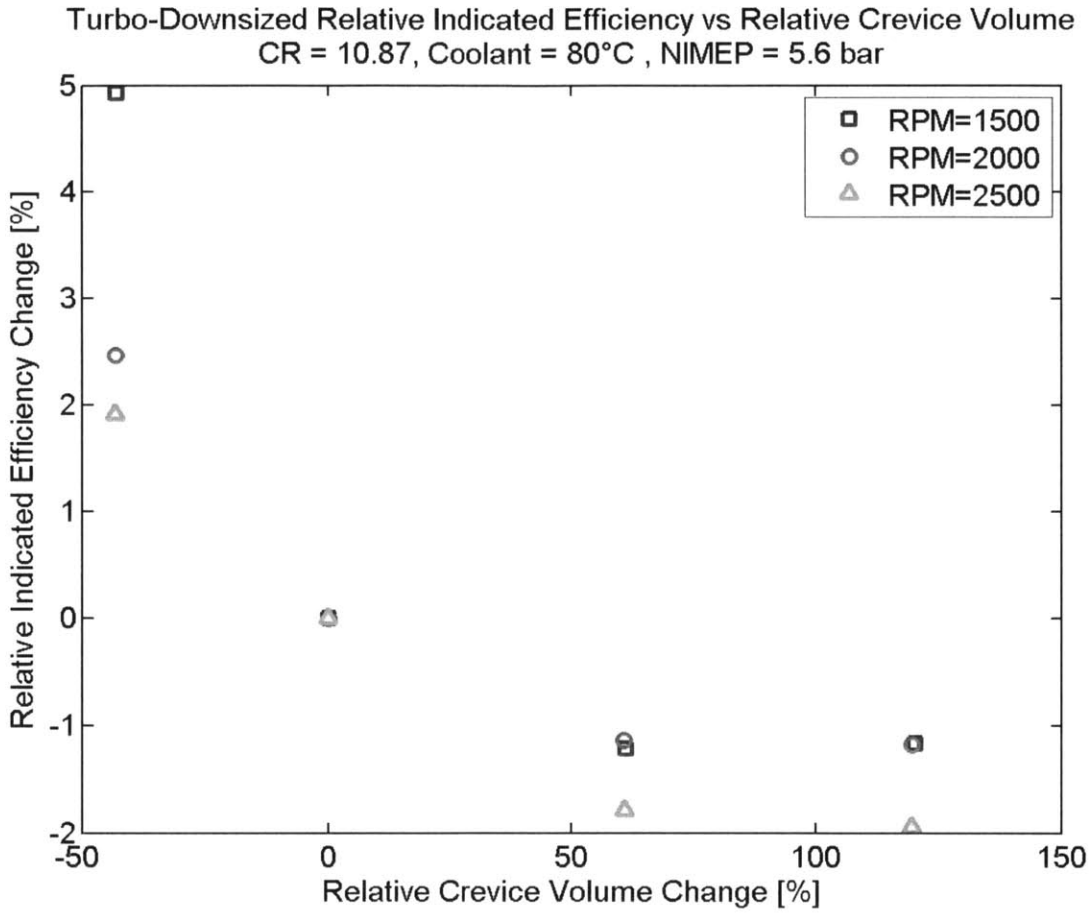

Figure C-4 Relative indicated efficiency change versus relative crevice volume change for a compression ratio of 10.87, 80°C coolant temperature, and an NIMEP value of 5.6 bar at various speeds.

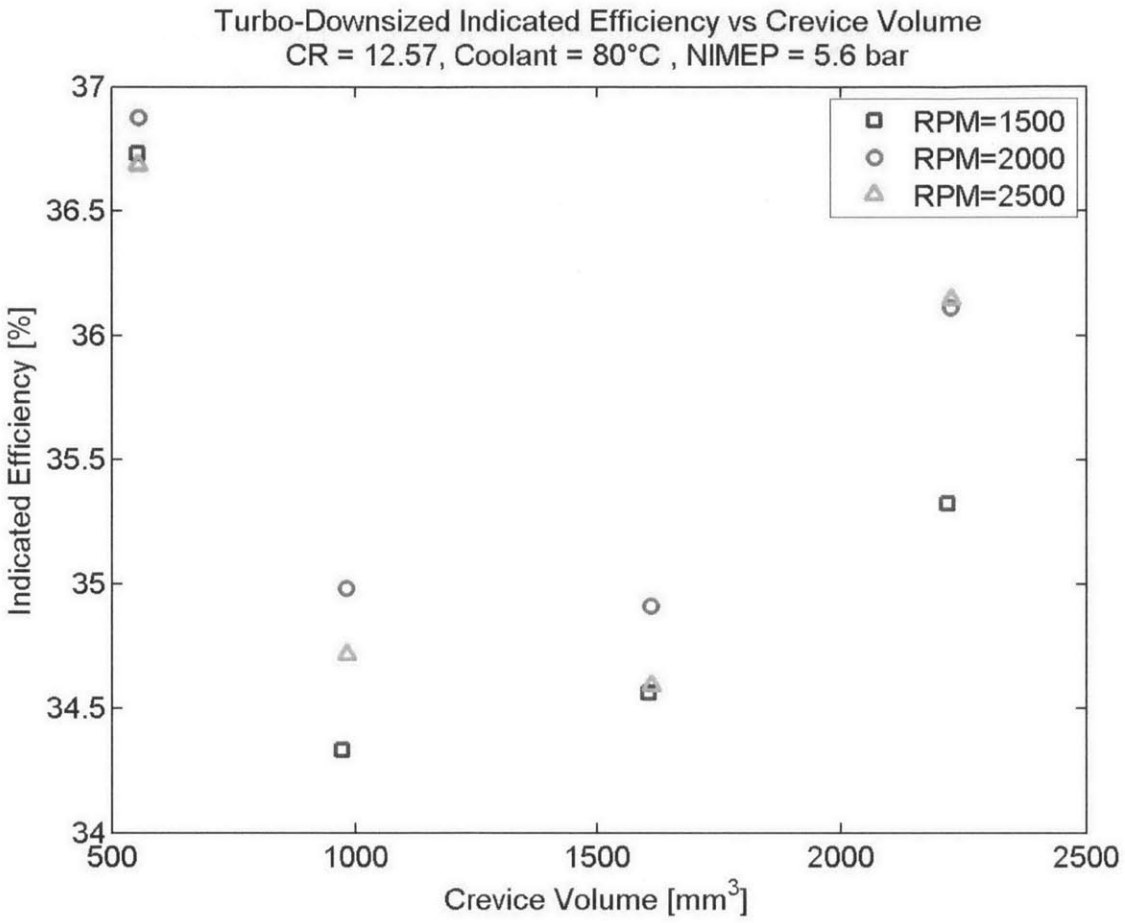

Figure C-5 Indicated efficiency versus crevice volume for a compression ratio of 12.57, 80°C coolant temperature, and an NIMEP value of 5.6 bar at various speeds.

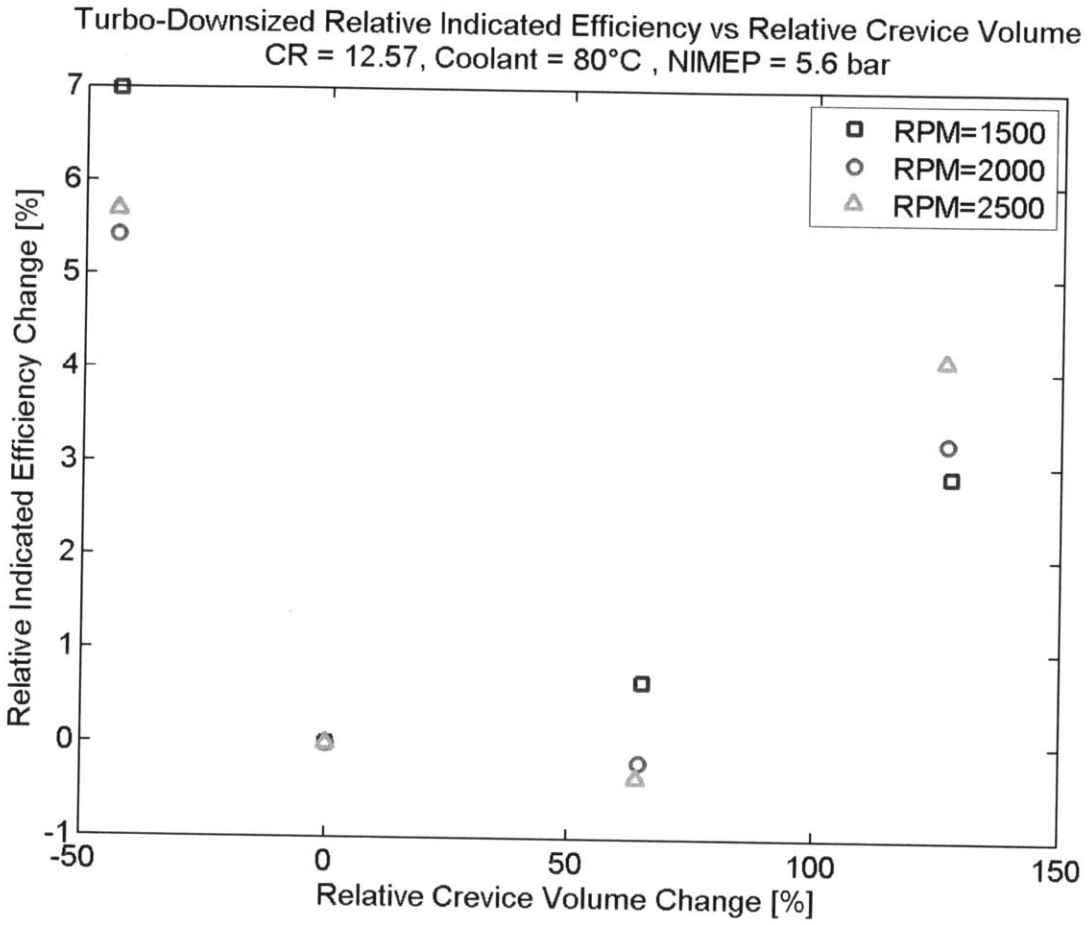

Figure C-6 Relative indicated efficiency change versus relative crevice volume change for a compression ratio of 12.57, 80°C coolant temperature, and an NIMEP value of 5.6 bar at various speeds.

Appendix D: Additional Plots across Coolant Temp

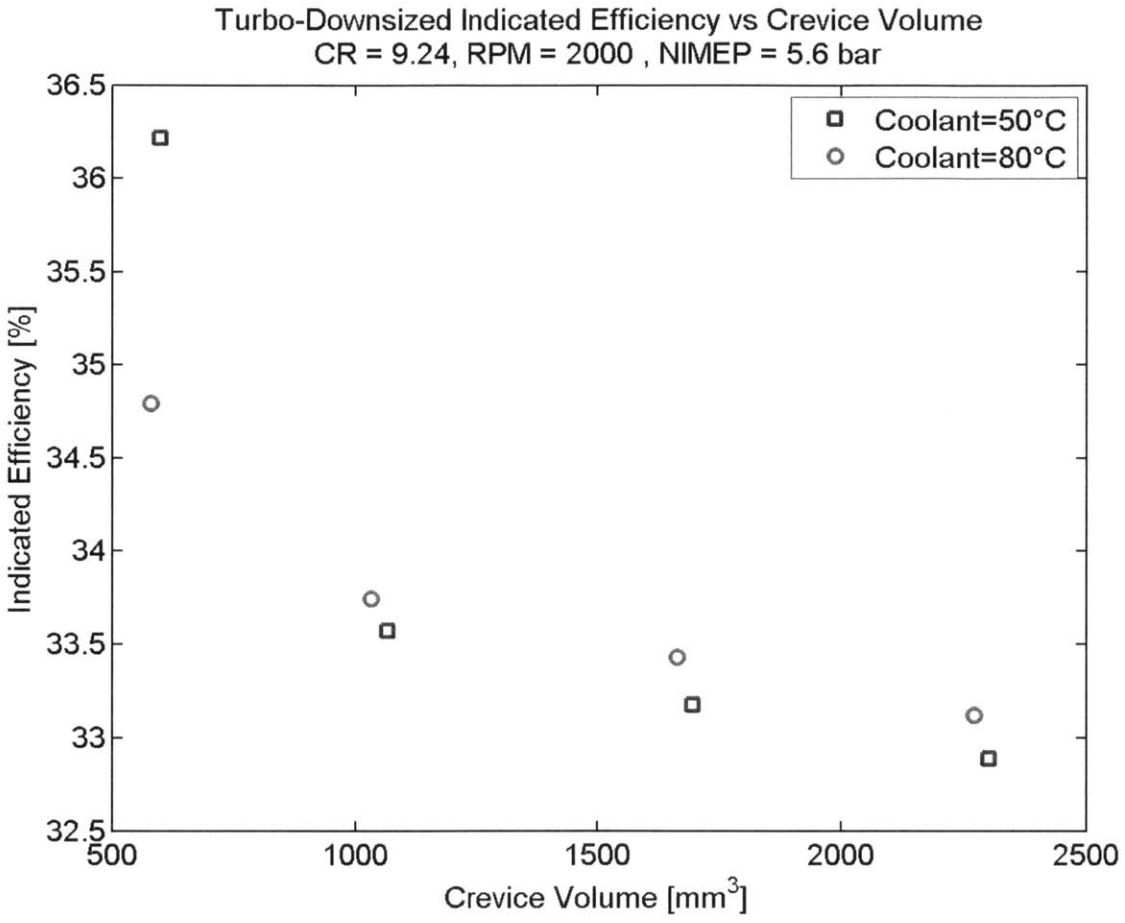

Figure D-1 Indicated efficiency versus crevice volume for a compression ratio of 9.24, speed of 2000 rpm, and an NIMEP value of 5.6 bar at two coolant temperatures.

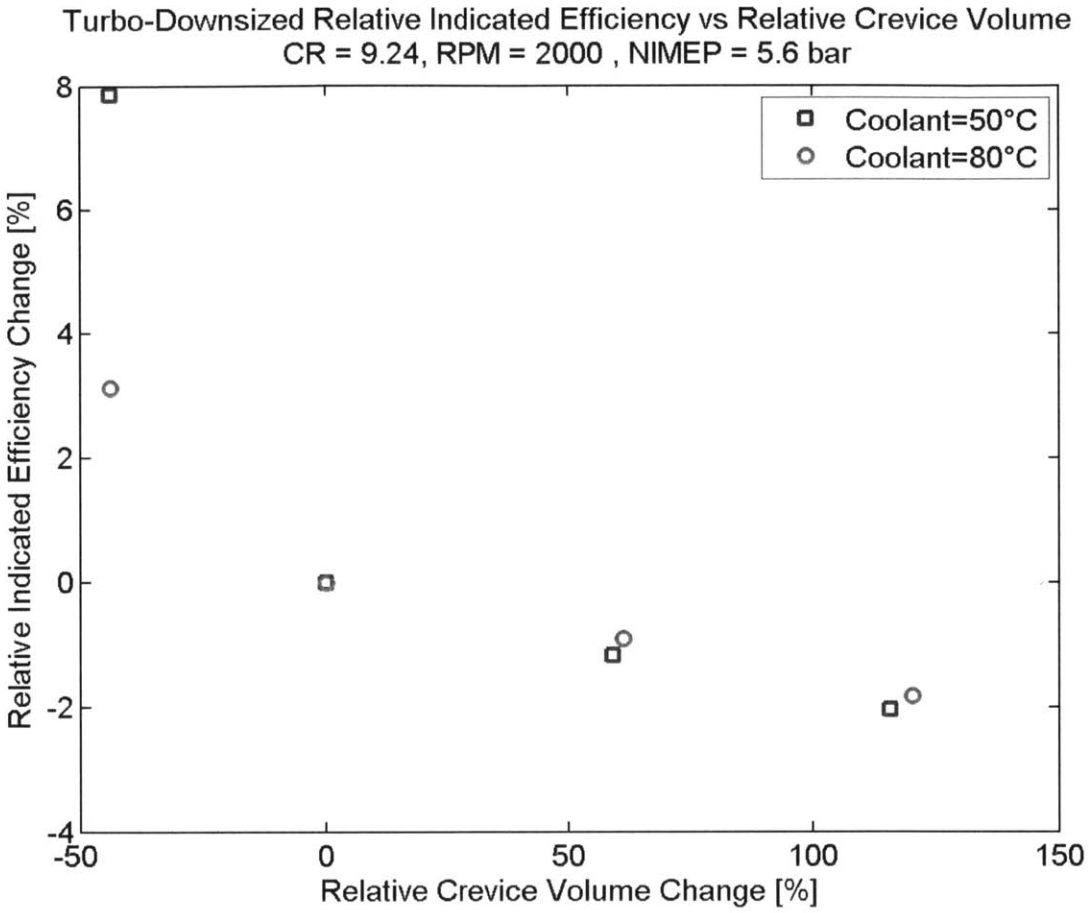

Figure D-2 Relative indicated efficiency change versus relative crevice volume change for a compression ratio of 9.24, speed of 2000 rpm, and an NIMEP value of 5.6 bar at two coolant temperatures.

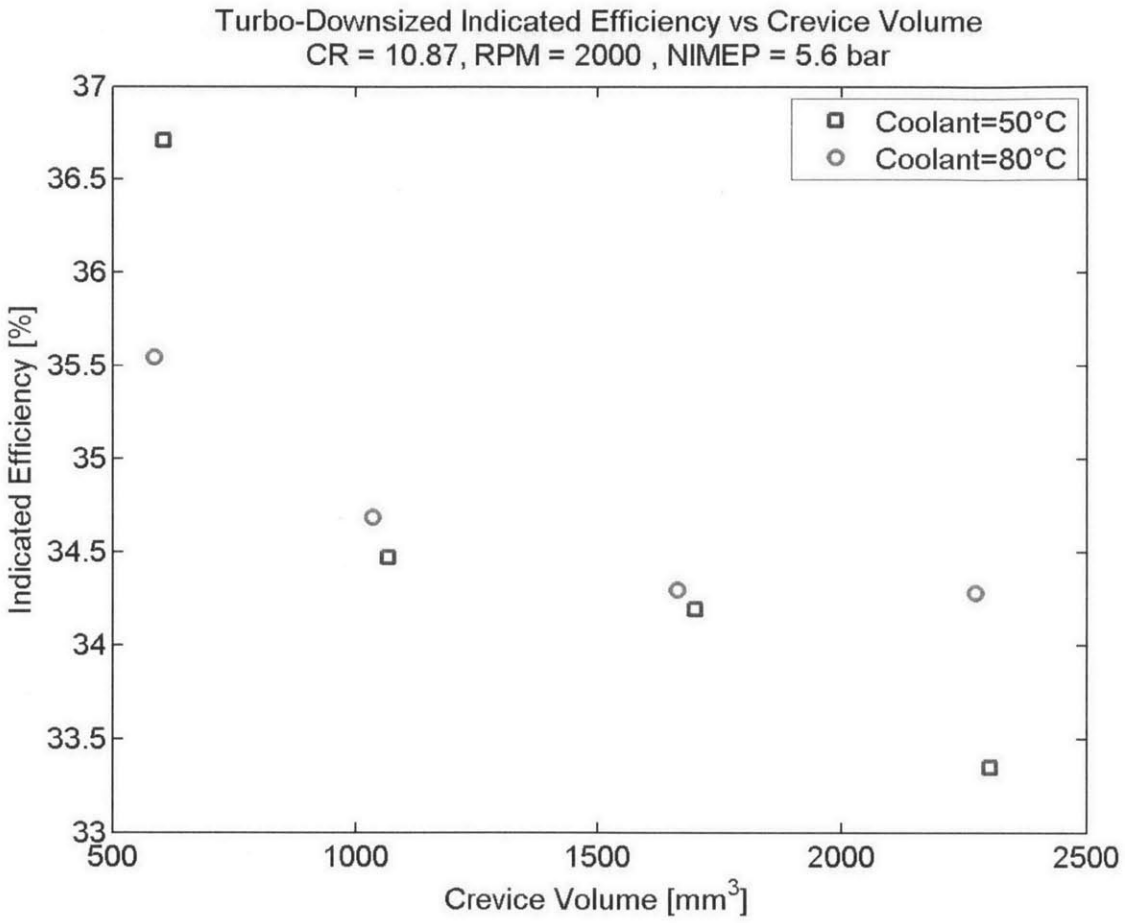

Figure D-3 Indicated efficiency versus crevice volume for a compression ratio of 10.87, speed of 2000 rpm, and an NIMEP value of 5.6 bar at two coolant temperatures.

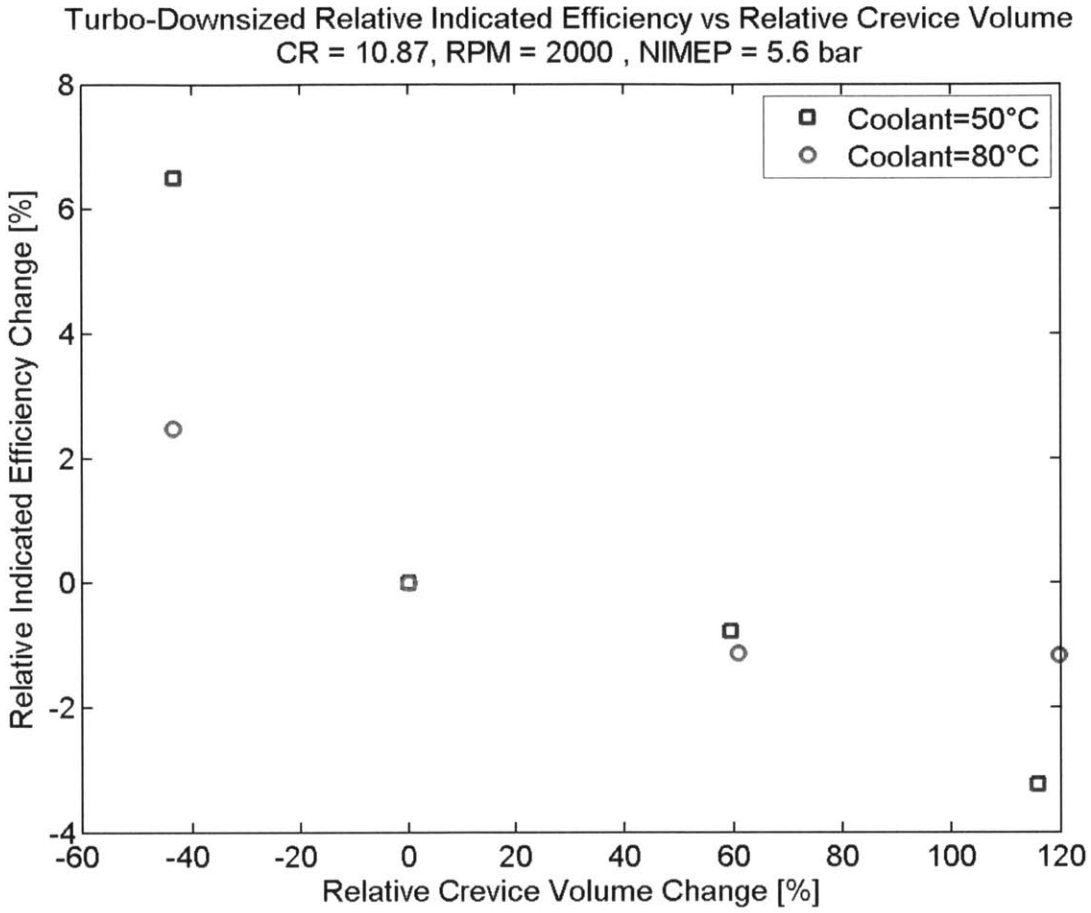

Figure D-4 Relative indicated efficiency change versus relative crevice volume change for a compression ratio of 10.87, speed of 2000 rpm, and an NIMEP value of 5.6 bar at two coolant temperatures.

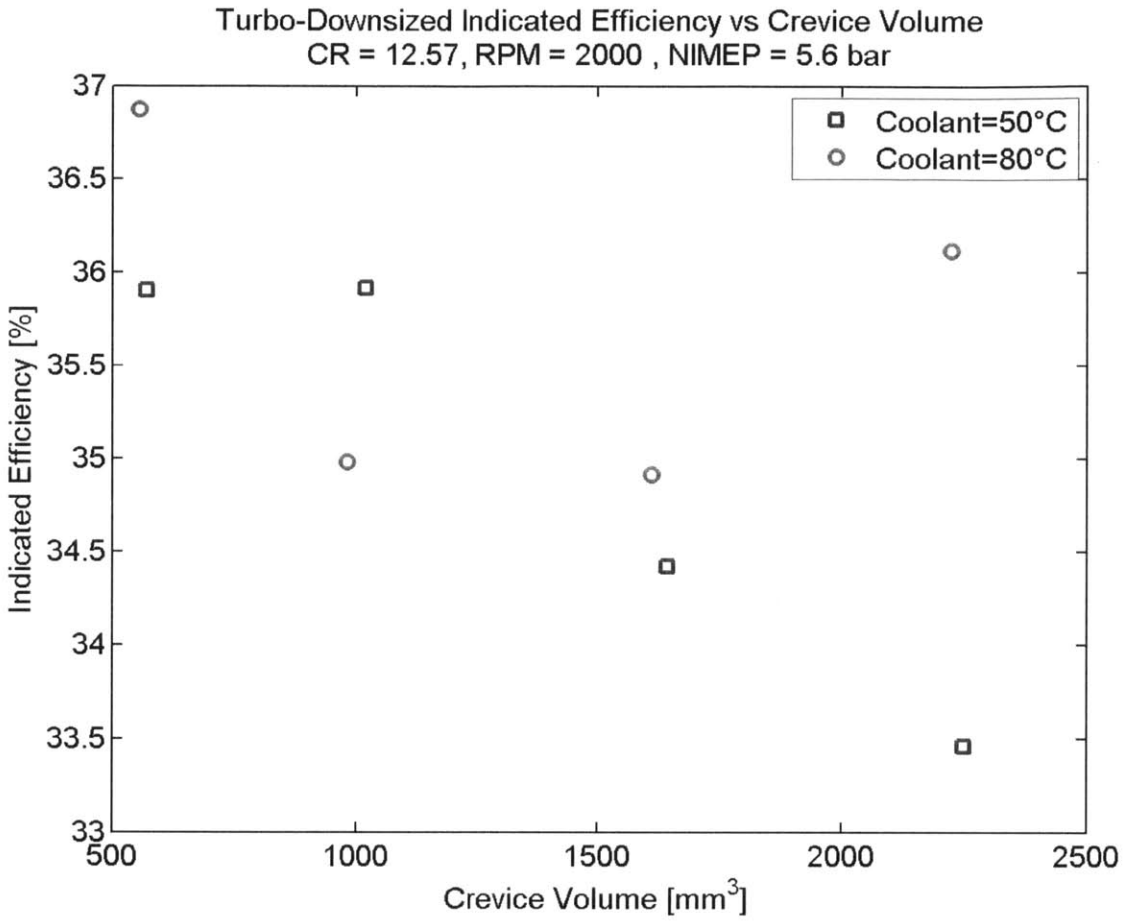

Figure D-5 Indicated efficiency versus crevice volume for a compression ratio of 12.57, speed of 2000 rpm, and an NIMEP value of 5.6 bar at two coolant temperatures.

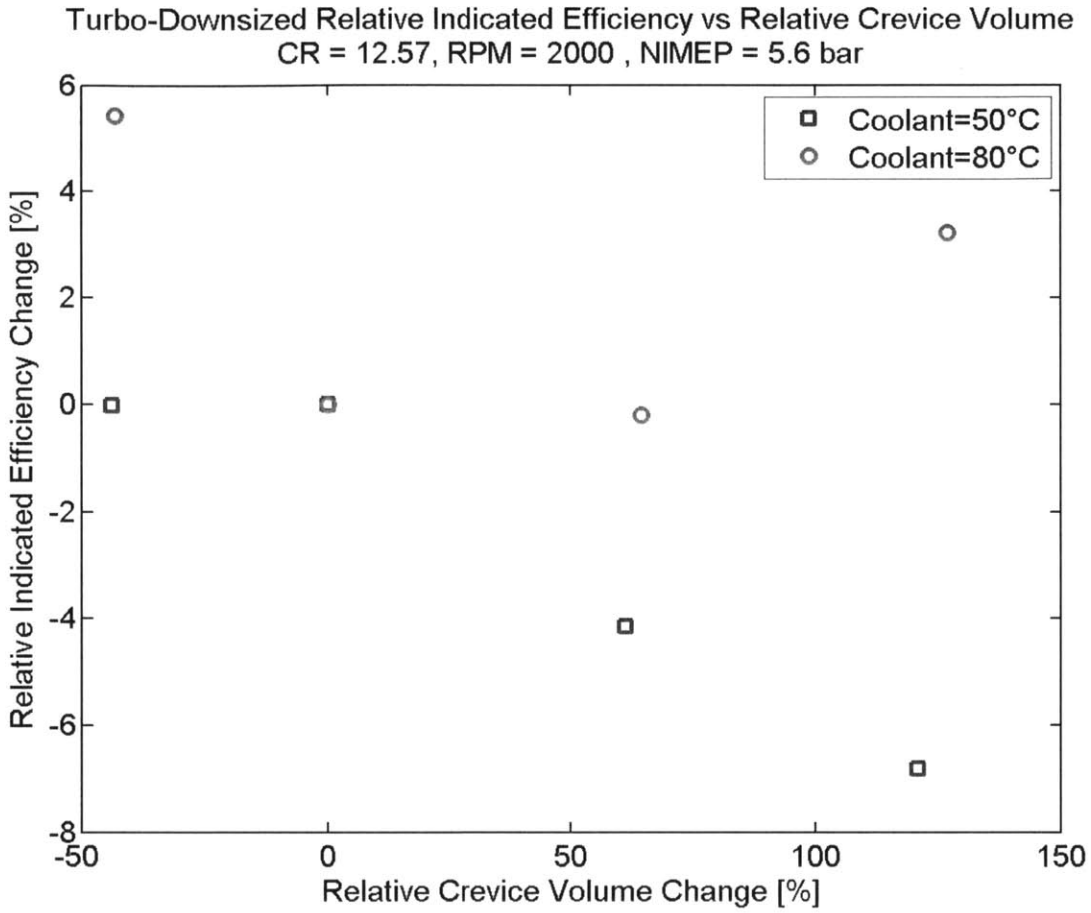

Figure D-6 Relative indicated efficiency change versus relative crevice volume change for a compression ratio of 12.57, speed of 2000 rpm, and an NIMEP value of 5.6 bar at two coolant temperatures.

Works Cited

[1] Department of Transportation, Environmental Protection Agency, and National Highway Traffic Safety Administration, 2012, "2017 and Later Model Year Light-Duty Vehicle Greenhouse Gas Emissions and Corporate Average Fuel Economy Standards," **77**(199), pp. 62623–63200.

[2] Atkins M. J., and Koch C. R., 2003, "A Well-to-Wheel Comparison of Several Powertrain Technologies," SAE Technical Paper 2003-01-0081.

[3] Arnold S., Balis C., Jeckel D., Larcher S., Uhl P., and Shahed S. M., 2005, "Advances in Turbocharging Technology and its Impact on Meeting Proposed California GHG Emission Regulations," SAE Technical Paper 2005-01-185.

[4] Bisordi A., Oudenijeweme D., Bassett M., Stansfield P., Williams J., and Ali R., 2012, "Evaluating Synergies between Fuels and Near Term Powertrain Technologies through Vehicle Drive Cycle and Performance Simulation," SAE Technical Paper 2012-01-0357.

[5] Leduc P., Dubar B., Ranini A., and Monnier G., 2003, "Downsizing of Gasoline Engine : an Efficient Way to Reduce CO2 Emissions," Oil & Gas Science and Technology, **58**(1), pp. 115–127.

[6] Lecointe B., and Monnier G., 2003, "Downsizing a Gasoline Engine Using Turbocharging with Direct Injection," SAE Technical Paper 2003-01-0542.

[7] Lake T., Stokes J., Murphy R., Osborne R., and Schamel A., 2004, "Turbocharging Concepts for Downsized DI Gasoline Engines," SAE Technical Paper 2004-01-0036.

[8] Bandel W., Fraidl G. K., Kapus P. E., and Sikinger H., 2006, "The Turbocharged GDI Engine: Boosted Synergies for High Fuel Economy Plus Ultra-Low Emissions," SAE Technical Paper 2006-01-1266.

[9] Han D., Han S., Han B., and Kim W., 2007, "Development of 2.0L Turbocharged DISI Engine for Downsizing Application," SAE Technical Paper 2007-01-0259.

[10] Shahed S. M., and Bauer K., 2009, "Parametric Studies of the Impact of Turbocharging on Gasoline Engine Downsizing," SAE Technical Paper 2009-01-1472.

[11] Lumsden G., Oudenijeweme D., Fraser N., and Blaxill H., 2009, "Development of a Turbocharged Direct Injection Downsizing Demonstrator Engine," SAE Technical Paper 2009-01-15.

[12] Adamczyk A. A., Kaiser E. W., and Lavoie G. A., 1983, "A Combustion Bomb Study of the Hydrocarbon Emissions from Engine Crevices," Combustion Science and Technology, pp. 261–277.

[13] Goolsby A. D., and Haskell W. W., 1976, "Flame-Quench Distance Measurements in a CFR Engine," Combustion and Flame, **26**, pp. 105–114.

[14] Saika T., and Korematsu K., 1986, "Flame Propagation into the Ring Crevice of a Spark Ignition Engine," SAE Technical Paper 861528.

[15] Sterlepper J., Neuber H. J., and Ruhland H., 1994, "HC-Emissions of SI Engines-Optical Investigation of Flame Propagations in Piston Top Land Crevice," SAE Technical Paper 941994.

[16] Alkidas A. C., Drews R. J., and Miller W. F., 1995, "Effects of Piston Crevice Geometry of the Steady-State Engine- Out Hydrocarbons Emissions of a SI Engine," SAE Technical Paper 952537.

[17] Daniel W. A., 1970, "Why Engine Variables Affect Exhaust Hydrocarbon Emission," SAE Technical Paper 700108.

[18] Williams F. A., 1985, Combustion Theory, The Benjamin/Cummings Publishing Company Inc.

[19] Lavoie G. A., 1978, "Correlations of Combustion Data for SI Engine Calculations-Laminar Flame Speed, Quench Distance and Global Reaction Rates," SAE Technical Paper 780229.

[20] Rhodes D. B., and Keck J. C., 1985, "Laminar Burning Speed Measurements of Indolene-Air-Diluent Mixtures at High Pressures and Temperatures," SAE Technical Paper 850047.

[21] Metghalchi M., and Keck J. C., 1982, "Burning Velocities ofMmixtures of Air with Methanol, Isooctane, and Indolene at High Pressure and Temperature," Combustion and Flame, **48**, pp. 191–210.

[22] Gordon S., and McBride B. J., 1994, "Computer Program for Calculation of Complex Chemical Equilibrium Compositions and Applications," NASA Reference Publication 1311.

[23] Heywood J., 1988, Internal combustion engine fundamentals.

[24] Kaplan J. A., and Heywood J. B., 1991, "Modeling the Spark Ignition Engine Warm-Up Process to Predict Component Temperatures and Hydrocarbon Emissions," SAE Technical Paper 910302.

[25] Esfahanian V., Javaheri A., and Ghaffarpour M., 2006, "Thermal analysis of an SI engine piston using different combustion boundary condition treatments," Applied Thermal Engineering, **26**(2-3), pp. 277–287.

[26] Gatowski J. A., Balles E. N., Chun K. M., Nelson F. E., Ekchian J. A., and Heywood J. B., 1984, "Heat Release Analysis of engine Pressure Data," SAE Technical Paper 841359.

[27] Namazian M., and Heywood J. B., 1982, "Flow in the Piston-Cylinder-Ring Crevices of a Spark-Ignition Engine: Effect on Hydrocarbon Emissions, Efficiency and Power," SAE Technical Paper 820088.

[28] Min K., Cheng W. K., and Heywood J. B., 1994, "The Effects of Crevices on the Engine-Out Hydrocarbon Emissions in SI Engines," SAE Technical Paper 940306.

[29] Min K., and Cheng W. K., 1995, "Oxidation of the Piston Crevice Hydrocarbon During the Expansion Process in a Spark Ignition Engine," Combustion Science and Technology, **106**(4-6), pp. 307–326.

[30] Wu K. C., and Hochgreb S., 1997, "Numerical Simulation of Post-Flame Oxidation of Hydrocarbons in Spark Ignition Engines," SAE Technical Paper 970886.

[31] Tamura M., Sakurai T., and Tai H., 2001, "A Study of Crevice Flow in a Gas Engine Using Laser-Induced Fluorescence," SAE Technical Paper 2001-01-0913.

[32] Cheng W. K., Hamrin D., Heywood J. B., Hochgreb S., Min K., and Norris M., 1993, "An Overview of Hydrocarbon Emissions Mechanisms in Spark Ignition Engines," SAE Technical Paper 932708.

[33] Wentworth J. T., 1971, "The Piston Crevice Volume Effect on Exhaust Hydrocarbon Emission," Combustion Science and Technology.

[34] Thompson N. D., and Wallace J. S., 1994, "Effect of Engine Operating Variables and Piston and Ring Parameters on Crevice Hydrocarbon Emissions," SAE Technical Paper 940480.

[35] Boam D. J., Finlay I. C., Biddulph T. W., Ma T. A., Lee R., Richardson S. H., Bloomfield J., Green J. A., Wallace S., and Woods W. A., 1994, "The sources of unburnt hydrocarbon emissions from spark ignition engines during cold starts and warm-up," Proceedings of the Institution of Mechanical Engineers, Part D: Journal of Automobile Engineering.

[36] Ayala F. A., Gerty M. D., and Heywood J. B., 2006, "Effects of combustion phasing, relative air-fuel ratio, compression ratio, and load on SI engine efficiency," SAE Technical Paper 2006-01-0229, (724).

[37] Smith P., and Cheng W. K., 2013, "Assessing the Loss Mechanisms Associated with Engine Downsizing , Boosting and Compression Ratio Change," SAE Technical Paper 2013-01-0929.

[38] Bromberg L., Cohn D., and Heywood J., 2007, "Optimized Fuel Management System for Direct Injection Ethanol Enhancement of Gasoline Engines," US Patent 7,225,787.

[39] Patton K. J., Nitschke R. G., and Heywood J. B., 1989, "Development and Evaluation of a Friction Model for Spark-Ignition Engines," SAE Technical Paper 890836.

[40] Sandoval D., and Heywood J. B., 2003, "An ImprovedFfriction Model for Spark-Ignition Engines," SAE Technical Paper 2003-01-0725.

[41] Goldwitz J. A., 2004, "Combustion Optimization in a Hydrogen-Enhanced Lean Burn SI Engine," S.M.M.E. Thesis.

[42] Davis R. S., and Patterson G. J., 2006, "Cylinder Pressure Data Quality Checks and Procedures to Maximize Data Accuracy," SAE Technical Paper 2006-01-1346.

[43] Cambustion, 2006, HFR400 Fast Response Hydrocarbon Measurement System User Manual.

[44] Cheung H., 1993, "A Practical Burn RateAanalysis for Use in Engine Development and Design," S.M.M.E. Thesis.

[45] Cho H., Lee K., Lee J., Yoo J., and Min K., 2001, "Measurements and Modeling of Residual Gas Fraction in SI Engines," SAE Technical Paper 2001-01-1910.

[46] Tian T., 1997, "Modeling the Performance of the Piston Ring-Pack in Internal Combustion Engines," PhD Thesis.

[47] Tian T., Noordzij L. B., Wong V. W., and Heywood J. B., 1998, "Modeling Piston-Ring Dynamics, Blowby, and Ring-Twist Effects."

[48] Tian T., 2002, "Dynamic behaviours of piston rings and their practical impact. Part 1: ring flutter and ring collapse and their effects on gas flow and oil transport," Institution of Mechanical Engineers, Part J: Journal of Engineering Tribology, **216**, pp. 209–227.

[49] Tian T., 2004, "Input and Output of the 2D Ring Dynamics Model," Conortium on Lubrication in I.C. Engines.